

DISSERTATION

IMPROVED RESOLUTION AND SPEED IN NONLINEAR MICROSCOPY

Submitted by

Omid Masihzadeh

Department of Electrical and Computer Engineering

In partial fulfillment of the requirements

For the Degree of Doctor of Philosophy

Colorado State University

Fort Collins, Colorado

Spring 2010

COLORADO STATE UNIVERSITY

March 26, 2010

WE HEREBY RECOMMEND THAT THE DISSERTATION PREPARED UNDER OUR SUPERVISION BY OMID MASIHZADEH ENTITLED IMPROVED RESOLUTION AND SPEED IN NONLINEAR MICROSCOPY BE ACCEPTED AS FULFILLING IN PART REQUIREMENTS FOR THE DEGREE OF DOCTOR OF PHILOSOPHY.

Committee on Graduate Work

M. Marconi

C. S. Menoni

J. Roberts

Advisor: R. A. Bartels

Department Head: A. A. Maciejewski

ABSTRACT OF DISSERTATION

IMPROVED RESOLUTION AND SPEED IN NONLINEAR MICROSCOPY

Optical microscopy is an important tool for biomedical research. New techniques for microscopy enable new capabilities for studying biological systems. Moreover, in optical microscopy, the polarization state of the focal field strongly influences the images formed due to the impact of focal spot size, adjusting the relative strength and phase of both transverse and longitudinal field components, and manipulating interaction with the sample under study. In particular, coherent nonlinear microscopies, such as third harmonic generation (THG), and second harmonic generation (SHG), offer rich possibilities for new control over the imaging process.

In the first part of this dissertation, I demonstrate that control over the spatial polarization state of the focal field can be used to improve the spatial resolution in a laser-scanning THG microscopy. First, we show a detailed design of our nonlinear scanning microscope, then we introduce a non-iterative algorithm for measurement of spatially inhomogeneous polarization distributions in third-harmonic generation microscopy. We also, show control of spatial polarization state of the focal field through imaging of a spatial light modulator to the focus of a microscope objective. Then, we introduced a novel technique for enhancing resolution in THG microscopy, through spatial polarization shaping at the focal field.

In the second part of this dissertation, we show an alternative method to laser-scanning nonlinear microscopy in biological tissue, namely, nonlinear holographic microscopy. First, we introduce the foundation of nonlinear holographic microscopy by reviewing linear off-axis holography. We start by introducing digital recording in off-axis holography, its limitations, and show how through holography we can obtain

3-D images from 2-D data. We then explore numerical reconstruction of the object field from the recorded holograms. Finally, we expand this technique to SHG nonlinear holographic microscopy to construct 3-dimensional images of biological tissues.

Omid Masihzadeh
Electrical and Computer Engineering
Colorado State University
Fort Collins, CO 80523
Spring 2010

Acknowledgments

The work presented here would have not been possible without support of many people I had the pleasure to work with. I would like to express my appreciation to my advisor, Professor R. A. Bartels, for his guidance and support during my time here in Colorado State University. He has been a great mentor, on and off the work place. I would like to thank him for believing in me and take me in as his graduate student, despite my background in the field of optics. His knowledge and dedication to pursue science and teaching has been a great model to follow. Also, many thanks goes to his wife Malini Ramakumar Bartels for making sure we don't go hungry in the lab. She makes the best cookies I have ever had.

Special thanks goes to all the people I worked with everyday for the past five years. I would like to thank our Post-Doc and a good friend of mine, Dr. Philip Schlup which has helped me throughout many hard, long, frustrating days in the lab. He is one of the most talented person I have ever had the pleasure to work with. I had the pleasure to work with many people in the lab who's input and comments on my work has been priceless. I would like to thank Klaus Hartinger, Jesse W. Wilson, Srinivasan Nirmalghandi, David G. Winters, David Kupka, Greg Futia, Brad Granger, and Jessica Gleason for all their support.

Finally, many thanks goes to all friends and family who have helped me through one of the most exciting and challenging time of my life. I like to thank my mom, whom I love the most, my dad for being understanding, and my brother whom I miss a lot.

Omid Masihzadeh, March. 26, 2010

Contents

1	Introduction	1
2	Nonlinear Optics	9
2.1	Introduction	9
2.2	Polarization Response of Material	11
2.2.1	Second Harmonic Generation	14
2.2.2	Third Harmonic Generation	16
2.3	The Propagation Equation	19
2.3.1	Monochromatic Light	22
2.3.2	Second Harmonic and Third Harmonic Generation under Focusing Conditions	24
2.4	Green's Function Formulation for Far-Field Nonlinear Signal	29
3	Nonlinear Microscopy	32
3.1	Nonlinear Laser Scanning Microscopy	33
3.1.1	Resolution	35
3.1.2	Scattering in Living Tissues	39
3.1.3	Signal detection	41
3.2	Second Harmonic Microscopy	43
3.3	Third Harmonic Generation Microscopy	46

4	Resolution Enhancement in Third Harmonic Microscopy through Polarization Switching	49
4.1	Introduction	49
4.1.1	Setup	50
4.1.2	Laser-scanning microscope design	52
4.2	Proposed Method for Resolution Enhancement	56
4.2.1	Spatial Polarization Shaping	57
4.3	THG Polarization Tomography of the Fundamental Field	61
4.3.1	Spatial Polarization Phase Retrieval	63
4.3.2	Theory	67
4.3.3	Analysis of experimental results	71
4.4	Summary	75
5	Holography	77
5.1	Introduction	77
5.2	Digital Recording in Off-Axis Holography	80
5.2.1	Obtaining 3-D Images from 2-D Data	82
5.2.2	Numerical Reconstruction of the Object Field	83
5.2.3	Resolution in Digital Holographic Microscopy	85
5.3	Summary	86
6	Label-Free Second Harmonic Generation Holographic Microscopy of Biological Specimens	87
6.1	Introduction	87
6.2	Theory	90
6.3	Experimental Setup	93
6.4	Results	96
6.5	Summary	99

7	Conclusion	102
A	Derivation of q^{th} Harmonics Generation under Focusing Conditions	104
A.1	The setup	104
A.1.1	The homogenous solution to Eq. (A.6)	106
A.1.2	The driving term in the spatial frequency space.	108
A.1.3	Inhomogeneous spatial frequency domain equation	109
A.2	Solutions in the spatial frequency domain	109
A.2.1	Limiting case of infinite uniform nonlinear media	111
A.2.2	Limiting case of non-uniform nonlinear media	113

List of Figures

2.1	Schematic and Jablonski diagrams of SHG (a) Physical diagram. (b) Jablonski diagram show two incident photons of frequency ν_1 simultaneously generate a photon with frequency twice the incident frequency. (c) Jablonski diagram show three incident photons of frequency ν_1 simultaneously generate a photon with frequency three times the incident frequency.	16
2.2	Geometry of a Gaussian beam focused (a) inside a bulk material and (b) on an interface of two material with different third order susceptibilities.	26
2.3	Interaction length for second and third harmonic versus phase matching.	28
2.4	Illustration of nonlinear object field generation, and its far-field detection, with definitions of the parameters of the excitation and detection coordinate systems.	31
3.1	(a) Radial resolution, is the ability of resolving two points sources separated by a distance Δr , located on the axis perpendicular to the optical axis, and (b) axial resolution, is the ability of resolving two points sources separated by a distance Δz located on the optical axis	36

3.2	Interaction volume: (a) Single-photon excitation, where the emission probability depends on excitation intensity $I(r)$. (b) Two-photon excitation, where the emission probability depends on the square of the excitation intensity $I^2(r)$	38
3.3	Contrast mechanism: imaging of human cardiac muscle using (a) White light microscopy. (b) SHG microscopy	41
3.4	Typical microscope setup: The laser beam is scanned radially across the sample (x, y) with a galvanometric scanner and axially using translation stage. A microscope objective focuses the beam on the sample and the emitted light is recorded by a detector.	42
3.5	SHG scanning microscopy of starch. (a) 2-D images of a single starch granule (b) 3-D.	44
3.6	Experiment (Blue) and theoretical (Red) data of SHG of a human cardiac muscle versus polarization angle. The discrepancy is believed to be due to the age of the sample.	45
3.7	THG from Biological samples: (a) Cell culture. (b) Zoomed in. (c) Onion. (d) Cornea.	47
3.8	Multi-modal imaging (White light, SHG, and THG): (a) Cornea. (b) Cell culture	48
4.1	FROG traces of pulse a) before the compressor (BK7), b) before the microscope objective, c) after the microscope objective.	51
4.2	THG images of a mesh grid ($12 \mu\text{m}$ pitch), before and after objective alignment procedure mentioned in the text.	54
4.3	Beam profile of the beam on the SLM (Blue), Gaussian fit (Red). The green step corresponds to the $\pi/2$ phase jump written on the SLM for enhanced resolution experiment (see text).	55

4.4	SLM characteristics: a) Calibration through spectral interferometry (see text).b) To ensure the bead under study does not affect the polarization at the focus, we apply a constant voltage across the SLM, while monitoring the THG signal. We repeat this procedure on a cover slip. Both nano-bead and the cover glass behave the same and have the same response to the polarization at the focus.	55
4.5	Demagnification. a) Beam displacement on the SLM, and b) beam movement at the focus of the objective.	56
4.6	Principle of spatial resolution enhancement. The superposition of a spatially-uniform phase in the s polarization and a $\pi/2$ -rad phase jump on the p polarization switches the polarization state from linear in the center to circular at some radius r_s . This suppresses the THG signal at the edges, giving rise to enhanced resolution.	57
4.7	Simulation of spatial filtering caused by low numerical aperture of the collecting lens. a) Beam profile and the applied $\pi/2$ phase jump on the SLM. b) Spatial filtering of the spatial frequency. The numerical aperture of the collecting lens, filters high spatial frequency content due to the abrupt phase jump and c) smoothes the abrupt phase discontinuity.	58
4.8	The SLM shapes an spatially uniform linear polarized beam so that the edges of the beam are circularly polarized while the center of the beam is kept linear. The THG signal from the medium is suppressed at regions of the beam that is circularly polarized, while significant THG signal is observed at the center of the beam where the polarization is kept linear.	59

4.9	Experimental setup: The laser beam driven from the 1550 nm fiber oscillator is collimated and expanded, and compressed by double passing two blocks of BK7 material. The elliptical polarized beam is then polarized (<i>P1</i>) and its polarization is rotated by its a half waveplate (<i>L2</i>). The beam is focused on the SLM and re-collimated with <i>f1</i> and <i>f2</i> resp. A scanning galvanometer is imaged on the back aperture of the objective by a 1 : 1 imaging telescope. Polarizer <i>P2</i> is used for the polarization tomography experiment, and a window plate <i>SW</i> scans the beam across the SLM for demagnification characterization. . . .	60
4.10	Isotropic response: The THG signal from an isotropic bead with linearly polarized focal field: THG signal is a) suppressed with a circularly polarized field. c) independent of the direction of the linearly polarized field.	61
4.11	Spatial electric field retrieval. a) An electric field can be decomposed in terms of its <i>x</i> and <i>y</i> -polarization, while the phase difference between the two are needed to completely characterized the field. b) There intensity measurement with a polarizer at angles $\eta = 0^\circ$ and $\eta = 90^\circ$ and $\eta \neq 0^\circ, 90^\circ$, say $\eta = 45^\circ$ are needed to fully recover the spatial features of an electric field.	64
4.12	Third order power dependence of the signal. the slope is measured to be 2.8	65
4.13	Maximum values of three components of the field going in the vicinity of the focus, for a) low and b) high numerical apertures.	67
4.14	Ratio of the maximum values of the focal field amplitudes a) $\frac{ Ez_{max} }{ Ex_{max} }$, and b) $\frac{ Ey_{max} }{ Ex_{max} }$ for a low, moderate, and high numerical aperture. . . .	67

4.15	(a) Spatially uniform phase across the p-polarized field component of the laser beam. Dashed black lines correspond to the phase written on the SLM while the red lines are the retrieved phase. The green line represent the measured line-out of the third harmonic image of the bead and the black dotted line represents the line-out of the beam on the SLM, demagnified by the demagnification factor. (b) Retrieved vs. applied phase and corresponding signal to noise ratio (S/N), *.	71
4.16	(a) Ramp and quadratic phase: Applied (dashed) and retrieved (thick) phase, along with a line-out of the third harmonic image of the bead (thin). The line-outs are taken parallel to the imaged SLM axis.	72
4.17	Scanning THG microscopy images of 100 nm diameter polystyrene beads, with (a) a uniform linear polarization state and (b) a $\pi/2$ phase jump on the p polarization component.	73
4.18	(a) Phase applied to the SLM p polarization, relative to the beam intensity distribution. (b) Retrieved phase using tomographic phase retrieval. (c) Reconstructed THG image distribution (see text).	74
4.19	Enhanced resolution is shown as a function of polarization switched radius r_s/w . Also, corresponding decrease in the collected THG energy signal is shown.	75

5.1	Gabor's in-line configuration for holographic recording a) The interference pattern between the incident reference plane wave is recorded by a recording medium. Image reconstruction b), is accomplished by illuminating the hologram by the reconstruction beam, identical to the incident reference beam used for creating the hologram. The image of the object will appear where the object was located during the recording process. A conjugate image (twin-image) will also appear on the other side (the conjugate plane) of the recorded hologram, in line with the real image object.	78
5.2	In off-axis nonlinear holography the sample is illuminated by a fundamental short pulse. The residual fundamental beam will be filtered by a bandpass chromatic filter, while the second harmonic emerging from the sample will interfere with a second harmonic reference beam. The interference pattern will be recorded by a EMCCD camera.	79
5.3	Off-axis holography setup: recording a) the interference patter of the object beam and a reference beam incident on the photographic plate with a an angle θ with respect to the object beam. In reconstruction b) of the object beam, the hologram is illuminated with the same reference beam. In off-axis holography, however, the phase conjugated object image is separated from the real image with an angle θ	80
5.4	In frequency domain, the real and virtual images will be separated from the DC term (intensity of the reference and the object waves in the frequency domain), provided that the spatial carrier frequency of the interference pattern (which depends on the angle between the incident reference beam with respect to the object wave) is sufficiently high with respect to the bandwidth (B) of the object wave	81

5.5	Off-axis hologram a) of two point sources separated in the direction of the optical axis and laterally. The hologram of the two point sources are the superposition of two Fresnel zones with focal lengths f_1 and f_2 . In the reconstruction, b) the two points sources will appear at an average distance $z_1 = f_1$ and $z_2 = f_2$	83
5.6	By inserting an objective microscope between the object and the hologram one achieves a reduction of the spatial frequency component k_x, k_y by the magnification factor. (Only k_x is shown here)	86
6.1	(a) Experimental arrangement; see text for details. (b) Second-harmonic spectra measured for the reference beam (blue line) and samples human muscle (green), starch granules (red), and corn seed (cyan). (c) Interference Fresnel rings observed without a sample at the image plane, at time overlap between reference and independently frequency-doubled object pulses.	90
6.2	A cluster of starch granules (scale is the same for all figures): (a) White light; (b) second-harmonic from the sample; (c) measured hologram; (d) reconstruction at image plane.	93
6.3	Peak intensities, in local regions around starch grains marked A , B and C in Fig. 6.2, with varying reconstruction distance d_H . The peaks correspond to the axial plane where each grain is focused. Comparison between two object planes d_S allows us to estimate the microscope axial magnification.	95
6.4	Image and reconstruction of corn seed at two different image and reconstruction planes.	96
6.5	Reconstruction of hologram showing several separate human muscle fibrils. The animation shows the assembly of reconstruction planes into the three-dimensional depiction of the sample.	98

6.6	Polarization dependence of the muscle tissue.	99
6.7	Dog stomach: Holographic a) reconstruction at the image plane, and b) around the focus. Also, the c) SHG image taken at focus is show. Rabbit tendon (c,d,e)	100
6.8	Corn seed: Holographic a) reconstruction at the image plane, and b) around the focus. Also, the c) SHG image taken at focus is show. Rabbit lymph (c,d,e).	101
A.1	Geometry of a Gaussian beam focused (a) inside a bulk material and (b) on an interface of two material with different third order suscepti- bilities.	110

Chapter 1

Introduction

Imaging is a powerful tool in many contemporary scientific research, including biomedical sciences. There have been three major stages of evolution of the imaging devices:

(1) Direct image plane image formation as a 2-D function by directly mapping each point of an object to a point in the image plane. It started by the invention of magnifying glass at the end of the 13th century by Salvino Degli Armati. The credit for the first microscope is usually given to Dutch spectacle maker Joannes and his son Zacharios Jansen, where through experimenting with several lenses they discovered that objects appeared greatly enlarged. The father of microscopy, Anthony Leeuwenhoek of Holland, was the first to describe bacteria, yeast plants, and the circulation of blood corpuscles in capillaries.

(2) Holographic imaging, which constitute of recording of amplitude and phase of the wave field radiated by the object in form of a hologram, and reproduction of the wave field by reconstruction of holograms. Invention of holography by D. Gabor [1] was motivated by the desire to improve resolution power of electron microscope that was limited by the fundamental limitations of the electron optics. The very first implementation of holography were not demonstrated until 1961 by radio-engineers E. Leith and J. Upatnieks [2, 3].

(3) Computational imaging, where images are obtained, stored, and manipulated digitally. For instance, recording the holographic interferograms with a CCD camera has led to significant improvements in speed of hologram processing. Using digital holograms, 3D microscopy images can be computed numerically from a single image capture [4, 5, 6, 7]

The conventional wide field optical microscopy, provides sub-micron spatial resolution and has had a tremendous impact in biology and medicine. The contrast mechanism in linear wide field optical microscopy is the transmission or reflectivity of the sample, or through changes in polarization. Since many cellular structures are transparent, the variation of the reflectivity and transmission is very small. Phase contrast and differential interference contrast (DIC) microscopes have been developed to convert the optical phase and polarization differences into intensity differences and greatly enhance the image contrast.

Although tremendous progress has been made in conventional optical microscopy, including confocal [8, 9], it has suffered from a low physical and chemical specificity [10]. The contemporary research of microelectronics, disease detection, material analysis, and biochemistry demand the ability to visualize the molecular identity and dynamics in real time. Many advanced imaging techniques have been invented to answer these challenges. With the development of fluorescence labels, fluorescence imaging has gained popularity among cell biologists and biochemists because the signal is specific to the label and its sensitivity reaches the single molecule level [11]. Despite its success, fluorescence imaging has several limitations [12, 8].

Current research in nonlinear microscopy is aiming to develop alternative methods that provide endogenous contrast. Various nonlinear signals, such as second harmonic generation (SHG) [13, 14], third harmonic generation (THG) [15, 16], and coherent anti-Stokes spectroscopy CARS [17, 18] have been used for imaging. SHG arises from the second order nonlinearity of materials with a noncentrosymmetric molecular or-

ganization. Certain biological materials such as collagen can assemble into large noncentrosymmetric structures, making them a good target for SHG microscopy [19, 20, 21, 22, 23, 24, 25, 26, 27, 28]. THG has no restriction on the symmetry property of the material. THG signals are strong at interfaces and small inhomogeneities of the size smaller than the focus. This has enabled the application of THG in imaging micrometer-sized lipid bodies in hepatocytes [15, 16, 20, 29, 30, 31, 32, 33].

The formation of images of biological specimens with coherent nonlinear scattering, through nonlinear scanning microscopy, opens unique image formation contrast due to the nature of nonlinear interactions. The strength of the nonlinear interaction in the medium, moreover, depends on the strength and polarization of the incident field. For instance, the polarization state of the focal field strongly influences the focal spot size [34], and by adjusting the relative strength and phase field components, one can manipulate the interaction between the field with the sample under study impacting the resolution [35]. In anisotropic samples, for example, manipulation of the focal field polarization state distribution can be used to probe the anisotropy of sub-wavelength particles interacting with the focal field [36].

While nonlinear scanning microscopy is a valuable and powerful tool, it is limited by low image acquisition rates. For acquiring 3-D images, the implementation of this technique requires a tightly focused fundamental pulse to be mechanically scanned across (x, y) and through the sample (z) , where images are assembled by serially collecting a nonlinear signal from each point. This time consuming process, often fails to capture dynamics of a process under study and presents a significant barrier for application of nonlinear microscopy to many areas [37, 38, 39, 40, 41, 42, 43]. By contrast, a hologram is capable of storing 3-D optical field information in a 2-D image, considerably improve image acquisition time.

In this dissertation, we explore nonlinear imaging through both nonlinear scanning

microscopy and nonlinear holographic microscopy. In nonlinear scanning microscopy we show an enhanced resolution in THG microscopy through shaping of spatial polarization of the fundamental field and manipulation of nonlinear interaction between the fundamental field and the medium. The lateral spatial resolutions achievable with nonlinear microscopies and ultra-high 1.2 NA water-immersion objectives are usually in the 300-500 μm range [44, 45, 46, 47]. In our work, under-filling the back aperture of our 0.65 NA objective yielded a resolution of 2 μm . Through polarization control, we were able to enhance this resolution by a factor of 2. A significant advantage of our technique is that it is generally applicable under any conditions used for THG microscopy.

Moreover, through nonlinear holographic microscopy, we illustrate fast 3-D imaging of biological tissues, with use of an home-built oscillator. We demonstrate image acquisition rates as low as 10 ms, currently limited by the opening time of our mechanical shutter. Although the shutter is not capable of continuous rapid switching, this would allow for video-rate microscopy imaging. Faster switching times are possible through the use of liquid crystal shutters [48] that have speeds of around 50-100 μs (e.g Swift Optical Shutters, Meadowlark Optics, Frederick, Colorado), or using the electro-optics effect with switching speeds of a few μs [49].

In the first part of this dissertation, I demonstrate that control over the spatial polarization state of the focal field can be used to improve the spatial resolution in a laser-scanning THG microscopy. First, we show a detailed design of our nonlinear scanning microscope, then we introduce a non-iterative algorithm for measurement of spatially inhomogeneous polarization distributions in third-harmonic generation microscopy. We also, show control of spatial polarization state of the focal field through imaging of a spatial light modulator to the focus of a microscope objective. Then, we introduced a novel technique for enhancing resolution in THG microscopy, through spatial polarization shaping at the focal field.

In the second part of this dissertation, we show an alternative method to laser-scanning nonlinear microscopy in biological tissue, namely, nonlinear holographic microscopy. First, we introduce the foundation of nonlinear holographic microscopy by reviewing linear off-axis holography. We start by introducing digital recording in off-axis holography, its limitations, and show how through holography we can obtain 3-D images from 2-D data. We then explore numerical reconstruction of the object field from the recorded holograms. Finally, we expand this technique to SHG nonlinear holographic microscopy to construct 3-dimensional images of biological tissues.

This work is organized as follows. In the first chapter, the fundamentals and mathematical tools for nonlinear optics is introduced. In this chapter, we first introduce the polarization response of material to an intense fundamental laser field. We explore the propagation of the laser field inside the medium, and generation of new field (SHG and THG) through the interaction of the fundamental field with the material. Then we present a two-dimensional model of SHG and THG, and a more general q^{th} harmonic generation under focusing conditions, and expand that to a three-dimensional calculation of nonlinear optical signal generation.

Chapter two will introduce the concept of nonlinear scanning microscopy. We show how through nonlinear scanning microscopy we achieve a new contrast modality, its impact on resolution and three-dimensional sectioning capability through scattering media like biological tissues. In particular we will explore nonlinear microscopy techniques like SHG and THG microscopy, and show some of the results we obtained experimentally.

In chapter three, we introduced a novel technique for enhancing resolution in THG microscopy, through spatial polarization shaping at the focal field. The nonlinear nature of third harmonic light results in emission of signal in a close vicinity of the focal volume, resulting in high lateral resolution [16, 15]. In optical microscopy, the lateral resolution is determined by the wavelength of light and the numerical aperture. In

transmission mode, the lateral resolution is determined by both the excitation and collection objectives. In direct imaging method [16], a slight advantage compared to laser scanning method [54] in resolution has been reported, since the lateral resolution is determined by the third-harmonic signal, where in laser scanning, the resolution is determined by both the fundamental and the third harmonic signal. In both cases, high numerical aperture objective ($NA > 1$) are required to achieve high resolution. These objectives, however, suffer from a very short working distance which is not desired for imaging of most thick biological sample. Even for thin biological sample (cell cultures grown in chamber slides), high working distance objectives are sometimes necessary. For example, a $NA = 1.4$ plan apochromat objective has a working distance of $d_w = 0.13$ mm where as a $NA = 0.75$ plan apochromat objective has a working distance of $d_w = 1$ mm, ideal for imaging of thick specimen. However, the resolution of the $NA = 1.4$ objective is about twice as much as the $NA = 0.75$ objective.

Over the past decay, a variety of techniques has been developed in fluorescent microscopy to enhance the resolution better than the diffraction limit [55, 56, 57, 58]. Yet, no technique has been developed for coherent nonlinear microscopy techniques. Here, we illustrate an enhanced resolution by a factor of 2 through quenching of THG signal by a circularly polarized light. This technique can be used in conjunction with any numerical aperture objective. For instance, the author in reference [16] uses a $NA = 1.25$ collection objective to image rhizoids of Chara plant, by collecting the 400 nm third harmonic signal. Under optimal conditions, this would result in a lateral resolution of $\Delta r = 0.61 \frac{400}{1.25} \sim 200nm$. Under the same conditions, through our novel THG quenching technique, we would have achieved a resolution of $\Delta r = 100nm$. This corresponds to an effective numerical aperture of $NA = 2.5$. Of course, such numerical aperture objective is not available and in order to reach such resolution, a shorter wavelength light has to be used.

In this chapter, we first show a detailed design of our nonlinear scanning microscope, then we introduce a non-iterative algorithm for measurement of spatially inhomogeneous polarization distributions in third-harmonic generation microscopy. We also, show control of spatial polarization state of the focal field through imaging of a spatial light modulator to the focus of a microscope objective.

Imaging in nonlinear microscopy, like SHG and THG microscopy, has largely been restricted to time consuming laser-scanning microscopy. The implementation of this technique requires the focused fundamental beam to be scanned through each volume element, where images are assembled by serially collecting the excited nonlinear signal. The refresh rate of image acquisition for nonlinear microscopy, however, fails to capture dynamics of a process under study and presents a significant barrier for application of nonlinear microscopy to many areas [42, 43, 37, 41, 40, 38]. The scanning of the fundamental beam is predominantly done with nonresonant galvonometric scanners, which can provide a frame rate of about 10 Hz. For instance, images of 300×300 pixels has been shown to take about 30 second to acquire [15]. For a $50 \mu\text{m}$ thick sample then (average thickness of histological samples), an average time of 25 min would be required to construct a 3-D image. Faster resonant galvonometers have been show to achieve video rate scanning speed with the expense of much more expensive and complicated electronics [59, 60]. In holography, however, 3-D optical field information can be retrieved by a single 2-D image.

The concept of holography is introduced in chapter four. In this chapter we lay the foundation of nonlinear holographic microscopy by first introducing linear off-axis holography. We start by introducing digital recording in off-axis holography, its limitations, and show how through holography we can obtaining 3-D images from 2-D data. We then explore numerical reconstruction of the object field from the recorded holograms. Finally, in chapter five we show nonlinear holographic microscopy using a low average power oscillator. Through this technique, we record and reconstruct

a 3-D image of a $100\ \mu\text{m}$ thick fixed cardiac muscle, in less than 10 ms. Here, the hologram was captured by an effective 400×400 pixel EMCCD camera. A 3-D image of the same sample using laser-scanning microscopy would take about 50 minutes.

Chapter 2

Nonlinear Optics

2.1 Introduction

Nonlinear optics is the study of the interaction of light with matter, where the response of the material depends in a nonlinear fashion on the input field strength. It wasn't until the invention of laser [61] when experimental observations of coherent nonlinear optics were realized [62]. Nonlinear optical processes have become an important subject in many field of research, including laser design, biomedical sciences, quantum computing. Our main focus in this thesis is nonlinear optical microscopy.

Although accurate descriptions of nonlinear optics requires a quantum mechanical treatment, the classical model of driven anharmonic oscillator provides a very good description of nonlinear optics phenomena, due to nonlinear electronic dipole response. In this picture, the electromagnetic wave induces an oscillating dipole moment in the media, where dipole displacement is not strictly proportional to the applied field, which may include frequencies different from those incident. The time dependent induced dipole moment per unit volume is, usually denoted by $\mathbf{P}(t)$ and called polarization, depends on the strength of the driving field $\mathbf{E}(t)$. For a lossless, dispersion-free medium, the polarization can often be expanded by power series in

terms of the driving field as [31],

$$\mathbf{P}(t) = \epsilon_0[\chi^{(1)}\mathbf{E}(t) + \chi^{(2)}\mathbf{E}^2(t) + \chi^{(3)}\mathbf{E}^3(t) + \dots] \quad (2.1)$$

$$= \mathbf{P}^{(1)}(t) + \mathbf{P}^{(2)}(t) + \mathbf{P}^{(3)}(t) + \dots \quad (2.2)$$

The first term in Eq. (2.2) represents the linear response of the material to the field. The constant in front of each field expansion order is called the susceptibility of the material. For linear response $\chi^{(1)}$ (second-rank tensor) is called the linear susceptibility. The quantities $\chi^{(2)}$ (third-rank tensor) and $\chi^{(3)}$ (forth-rank tensor) are called the second- and third order nonlinear susceptibilities. The second term in Eq. (2.2), $\mathbf{P}^{(2)}(t)$ and third term $\mathbf{P}^{(3)}(t)$, are called second-order nonlinear polarization and third-order nonlinear polarization, respectively.

Due to small value of nonlinear susceptibilities ($\chi^{(2)} \sim 10^{-12} \text{ m/V}$ and $\chi^{(3)} \sim 10^{-24} \text{ m}^2/\text{V}^2$) [31], the nonlinear polarizations are insignificant unless the applied field intensities $I = \frac{1}{2}\epsilon_0 c |\mathbf{E}(\mathbf{t})|^2$ are very large (but still small compared to atomic field intensity). Depending on the field strength, focusing conditions, and the symmetry of the material, some of the nonlinear polarizations might be absent. For example, as we will see later on, second order nonlinearity (and any even order nonlinearity) is only present in non-centrosymmetric material. Third order nonlinearity is present in all material, although under tight focusing conditions, or when the incident field is circularly polarized no far field signal will be observed. In this dissertation, we will only be concerned with linear, second- and third-order nonlinearity, and higher order nonlinearities will be neglected.

The aim of this chapter is to introduce the formalism of nonlinear optics that will apply to nonlinear microscopy. The discussion is limited to so-called parametric processes, which are processes for which the initial and final quantum- mechanical

states of the system are equal. These processes include phenomena like second harmonic generation (SHG) and third harmonic generation (THG). First, we introduce the main mathematical tools and the general form and properties of linear and nonlinear polarizations and susceptibilities are given. Then, we derive the nonlinear wave equation and apply that to fields under focusing conditions.

2.2 Polarization Response of Material

As we saw in section 2.1, strong fields inside a medium drive a nonlinear electronic response inside the medium. The strength of the nonlinearity in the medium depends on the strength of the field and the optical susceptibility tensor. The susceptibility tensors can be expressed in terms of its Fourier transform of the time domain response, by means of the Fourier integral identity. Transformation between time to frequency domain, and vice versa is done by Fourier transform. The Fourier transform and its inverse are defined as following,

$$f(t) = \frac{1}{2\pi} \int_{-\infty}^{\infty} d\omega F(\omega) e^{-i\omega t} \quad (2.3)$$

$$F(\omega) = \int_{-\infty}^{\infty} dt f(t) e^{i\omega t} \quad (2.4)$$

Using the above, we can describe the electric field and polarizability as,

$$\begin{cases} \mathbf{E}(\omega) = \frac{1}{2\pi} \int_{-\infty}^{\infty} dt \mathbf{E}(t) e^{-i\omega t} \\ \mathbf{E}(t) = \int_{-\infty}^{\infty} d\omega \mathbf{E}(\omega) e^{i\omega t} \end{cases} \quad (2.5)$$

and

$$\begin{cases} \mathbf{P}(\omega) = \frac{1}{2\pi} \int_{-\infty}^{\infty} dt \mathbf{P}(t) e^{-i\omega t} \\ \mathbf{P}(t) = \int_{-\infty}^{\infty} d\omega \mathbf{P}(\omega) e^{i\omega t} \end{cases} \quad (2.6)$$

Let us apply these formalism to linear response of the material. The response of such media to an electric field, in time domain can be written as [31],

$$\mathbf{P}_i^{(1)}(t) = \epsilon_0 \int_0^t d\tau R_{ij}^{(1)}(t - \tau) \mathbf{E}_j(\tau) = \epsilon_0 R_{ij}^{(1)}(t) \otimes \mathbf{E}(t_1) \quad (2.7)$$

where $R_{ij}^{(1)}(\tau)$ is linear response function, producing a linear polarization at time t , invoked by a field at time τ . In frequency domain, we can re-write the convolution as a product,

$$\mathbf{P}_i^{(1)}(\omega) = \epsilon_0 \chi_{ij}^{(1)}(\omega; \omega) \mathbf{E}_j(\omega) \quad (2.8)$$

where $\chi_{ij}^{(1)}(\omega; \omega) = \int_{-\infty}^{\infty} dt R_{ij}^{(1)}(t) e^{i\omega t}$. In writing the above equations, we have assumed time invariance, locality and causality.

Making the same assumptions, we can write the first two nonlinear polarizations as,

$$\mathbf{P}_i^{(2)}(t) = \epsilon_0 \int_0^\infty \int_0^\infty d\tau_1 d\tau_2 R_{ijk}^{(2)}(t - \tau_1, t - \tau_2) \mathbf{E}_j(\tau_1) \mathbf{E}_k(\tau_2) \quad (2.9)$$

and

$$\mathbf{P}_i^{(3)}(t) = \epsilon_0 \int_0^\infty \int_0^\infty \int_0^\infty d\tau_1 d\tau_2 d\tau_3 R_{ijkl}^{(3)}(t - \tau_1, t - \tau_2, t - \tau_3) \mathbf{E}_j(\tau_1) \mathbf{E}_k(\tau_2) \mathbf{E}_l(\tau_3) \quad (2.10)$$

where $R_{ijk}^{(2)}$ is the second order and $R_{ijkl}^{(3)}$ is the third order response function. Rewriting the nonlinear polarizabilities in terms of Fourier transform of the fields and the response function we get,

$$\mathbf{P}_i^{(2)}(t) = \frac{\epsilon_0}{(2\pi)^2} \int_0^\infty \int_0^\infty d\omega_1 d\omega_2 \chi_{ijk}^{(2)}(\omega; \omega_1, \omega_2) \mathbf{E}_j(\omega_1) \mathbf{E}_k(\omega_2) e^{-i(\omega_1 + \omega_2)t} \quad (2.11)$$

and

$$\mathbf{P}_i^{(3)}(t) = \frac{\epsilon_0}{(2\pi)^3} \int_0^\infty \int_0^\infty \int_0^\infty d\omega_1 d\omega_2 d\omega_3 \chi_{ijkl}^{(3)}(\omega; \omega_1, \omega_2, \omega_3) \mathbf{E}_j(\omega_1) \mathbf{E}_k(\omega_2) \mathbf{E}_l(\omega_3) e^{-i(\omega_1 + \omega_2 + \omega_3)t} \quad (2.12)$$

with

$$\chi_{ijk}^{(2)}(\omega; \omega_1, \omega_2) = \int_{-\infty}^\infty \int_{-\infty}^\infty dt_1 dt_2 R_{ijk}^{(2)}(t_1, t_2) e^{i(\omega_1 t_1 + \omega_2 t_2)} \quad (2.13)$$

$$\chi_{ijkl}^{(3)}(\omega; \omega_1, \omega_2, \omega_3) = \int_{-\infty}^\infty \int_{-\infty}^\infty \int_{-\infty}^\infty dt_1 dt_2 dt_3 R_{ijkl}^{(3)}(t_1, t_2, t_3) e^{i(\omega_1 t_1 + \omega_2 t_2 + \omega_3 t_3)} \quad (2.14)$$

Equations (2.11) and (2.12) can be transferred to the frequency domain by using Eq. (2.6). For example for a second-order polarization, we find

$$\begin{aligned} \mathbf{P}_i^{(2)}(\omega) &= \frac{\epsilon_0}{2\pi} \int_0^\infty \int_0^\infty d\omega_1 d\omega_2 \chi_{ijk}^{(2)}(\omega; \omega_1, \omega_2) \mathbf{E}_j(\omega_1) \mathbf{E}_k(\omega_2) \delta(\omega - \omega_1 - \omega_2) \\ &= \frac{\epsilon_0}{2\pi} \int_0^\infty d\omega_1 d\chi_{ijk}^{(2)}(\omega; \omega_1, \omega - \omega_1) \mathbf{E}_j(\omega_1) \mathbf{E}_k(\omega - \omega_1) \end{aligned} \quad (2.15)$$

and for the third-order polarization we get,

$$\mathbf{P}_i^{(3)}(\omega) = \frac{\epsilon_0}{(2\pi)^2} \int_0^\infty \int_0^\infty \int_0^\infty d\omega_1 d\omega_2 d\omega_3 \chi_{ijkl}^{(3)}(\omega; \omega_1, \omega_2, \omega_3) \mathbf{E}_j(\omega_1) \mathbf{E}_k(\omega_2) \mathbf{E}_l(\omega_3) \delta(\omega - \omega_1 - \omega_2 - \omega_3) \quad (2.16)$$

2.2.1 Second Harmonic Generation

Shortly after the invention of the Laser, the second harmonic generation was observed by Franken and co-workers [62]. In this process, two photons of frequency ν_1 are annihilated to create a new photon at twice the frequency $2\nu_1 = \nu_{SHG}$. The schematic and Jablonski diagram of SHG is shown in Fig. 2.1 [31, 63].

The strength of field radiated at second harmonic depends on the second order nonlinear optical susceptibility $\chi^{(2)}$ described by Eq. (2.13), and the induced polarization due to the interaction of the field with the material is described by Eq. (2.15). By substituting a cw electric field $\mathbf{E}(t) = \mathbf{A}_1 \cos(k_\omega z - \omega t)$ into Eq. (2.15), and setting $\omega_1 = \omega_2 = \omega$ we get,

$$\mathbf{P}_{2\omega}^{(2)} = \frac{1}{4}\epsilon_0\chi^{(2)}\mathbf{A}_1\mathbf{A}_1 \exp[i(2k_\omega z - 2\omega t)] \quad (2.17)$$

$$+ \frac{1}{4}\epsilon_0\chi^{(2)}\mathbf{A}_1\mathbf{A}_1 \exp[-i(2k_\omega z - 2\omega t)] \quad (2.18)$$

$$= \frac{1}{2}\epsilon_0\chi^{(2)}\mathbf{A}_1\mathbf{A}_1 \cos(2k_\omega z - 2\omega t) \quad (2.19)$$

Equation (2.19) is a manifestation of how the fundamental field induces the second order polarizability which in turn gives rise to a new field with the twice of the fundamental frequency.

One fundamental aspect of SHG, and any even order nonlinear phenomena, is that the polarization in centrosymmetric materials, that is material that possess a point which the medium remains unchanged under the operation $x \rightarrow -x$, is exactly zero. Basically, the inversion operation leaves the inversion-symmetric media unaffected, but does add minus signs to both polarizability, $\mathbf{P}_{2\omega}^{(2)} \rightarrow -\mathbf{P}_{2\omega}^{(2)}$ and the field $\mathbf{E}_\omega \rightarrow -\mathbf{E}_\omega$. This is only possible when $\chi^{(even)} = 0$. Mathematically, consider an electric field $E(t) = E_\omega \cos(\omega t)$ inside a centrosymmetric medium then,

$$-P(t) = \chi^{(2)}(-E(t))^2 \quad (2.20)$$

$$-P(t) = \chi^{(2)}(E(t))^2 \quad (2.21)$$

which will only hold if $\chi^{(2)}$ is zero. Therefore, only a non-centrosymmetric medium can exhibit nonzero polarization field, for $\chi^{(even)}$ material.

Many materials, such as Potassium dihydrogen phosphate (KDP) and β -barium borate (BBO) exhibit such symmetry and are widely used in nonlinear research. Materials with inversion symmetry generate no second harmonic in dipole approximation, a property which turns out to be key idea in SH microscopy of biological specimen, which contain highly structured tissues. Therefore SHG microscopy probes the organization of material structure through morphological analyses. We will talk about SHG microscopy in more detail in later chapter.

It is worth mentioning that SHG can be generated in centro-symmetric material using low frequency electric field. This process is usually described as a third-order nonlinear process with the nonlinear polarization described by [31]

$$\mathbf{P}^{(3)} = \frac{3}{4}\epsilon_o\chi^{(3)}\mathbf{E}(\omega)\mathbf{E}(\omega)\mathbf{E}(0) \quad (2.22)$$

where $\mathbf{E}(0)$ is the low frequency electric field. This process is usually referred as Electric-Field-Induced-Second-Harmonic-Generation. Even if the inversion symmetry is broken, the second harmonic signal, under most conditions, is very weak, and depends on the strength of the incident field.

In the past few decades, SHG has been widely used to the study of interfacial regions without a center of symmetry, and was later combined with a microscope for SHG scanning microscopy [64, 65]. Today, SHG scanning microscopes have been

widely used in material studies for surface monolayer detection [66], and electric field distribution imaging [67, 68]. Moreover, the explosion of research in nonlinear microscopy has shown the promise of SHG in tissue imaging. For instance, second harmonic is an ideal method for probing membranes of living cells [69]. The majority of the second harmonic microscopy reports have been focused on imaging collagen fibers in a variety of connective tissues including skin, bone, tendon, blood vessels, and cornea [70, 26, 71, 72] (and references within).

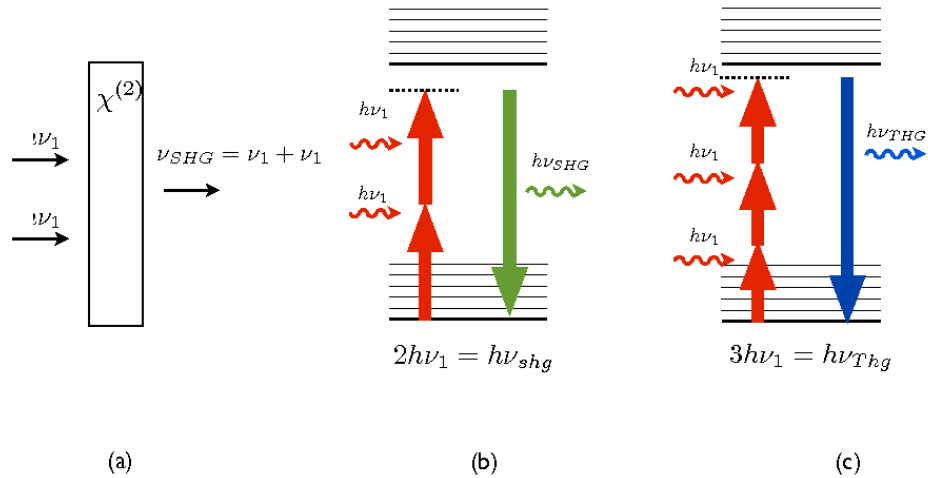


Figure 2.1: Schematic and Jablonski diagrams of SHG (a) Physical diagram. (b) Jablonski diagram show two incident photons of frequency ν_1 simultaneously generate a photon with frequency twice the incident frequency. (c) Jablonski diagram show three incident photons of frequency ν_1 simultaneously generate a photon with frequency three times the incident frequency.

2.2.2 Third Harmonic Generation

When the electric field in the medium is strong enough, the third order nonlinearity is not negligible anymore and gives rise to third harmonic generation (THG). THG is a third order nonlinear process due to the third order susceptibility $\chi^{(3)}$, that mixes three photons at the optical frequency ω to generate a photon at three times the

angular frequency of the incident photon. Figure 2.1 (c) show the Jablonski diagram for THG.

The induced third order polarization in the material is governed by Eq. (2.14). For a monochromatic wave we get,

$$\mathbf{P}_i^{(3)} = \frac{D\epsilon_0}{4}\chi_{ijkl}^{(3)}\mathbf{E}_j(\omega)\mathbf{E}_k(\omega)\mathbf{E}_l(\omega) \quad (2.23)$$

where the degeneracy factor $D = 1$ to 1 if all three frequencies are the same (THG), $D = 3$ if two frequencies are the same and $D = 6$ if all three frequencies are different.

In this dissertation, we will exclusively deal with isotropic medium, which makes the form of $\chi_{ijkl}^{(3)}$ isotropic. In general, for a given frequency combinations $\chi_{ijkl}^{(3)}$ has $3^4 = 81$ elements. But in isotropic media, there are only 21 nonzero elements, out of which only 3 of them are independent. That is due to the fact that for isotropic material, $\chi_{ijkl}^{(3)}$ is invariant to all transformations; rotation, reflection, and inversions. For example, consider reflection in $y - z$ plane, such that $x \rightarrow -x, y \rightarrow y, z \rightarrow z$. Then we have $\chi_{xyyz}^{(3)} = \chi_{xyzz}^{(3)} = 0$. Here, the first equality is by definition of invariant reflection, and the second equality is necessarily true, since $\mathbf{E} \neq -\mathbf{E}$. Applying this reasoning to other elements and planes, shows us that elements with odd number of indices are zero, hence 60 out of 81 elements are zero, which leaves only 21 elements having the form $\chi_{aaaa}^{(3)}, \chi_{aabb}^{(3)}, \chi_{baab}^{(3)}, \chi_{abab}^{(3)}$. Now considering a 90° rotation about the z -axis, $x \rightarrow y, y \rightarrow -x, z \rightarrow z$, and realizing invariant under rotation we get, for example, $\chi_{xxxx}^{(3)} \rightarrow \chi_{yyyy}^{(3)} = \chi_{xxxx}^{(3)}; \chi_{xxyy}^{(3)} \rightarrow \chi_{yyxx}^{(3)} = \chi_{xxyy}^{(3)}$, and so on. Rotation around other axis and repeating this procedure leaves only 4 independent elements. Next, performing an arbitrary rotation by an angle Φ about an arbitrary axis will leave you with 3 independent elements $\chi_{xxxx}^{(3)} = \chi_{xxyy}^{(3)} + \chi_{xyxy}^{(3)} + \chi_{xyyx}^{(3)}$. Hence, $\chi_{ijkl}^{(3)}$ for an isotropic medium can be written as,

$$\chi_{ijkl}^{(3)} = a\delta_{ij}\delta_{ij} + b\delta_{ij}\delta_{ij} + c\delta_{ij}\delta_{ij} \quad (2.24)$$

where $a = \chi_{xxyy}^{(3)}$, $b = \chi_{xyxy}^{(3)}$, $c = \chi_{yyxx}^{(3)}$. Therefore, for isotropic media we have,

$$\mathbf{P}_i^{(3)} = \frac{\epsilon_o}{4} [a\mathbf{E}_i(\omega)\mathbf{E}_k(\omega)\mathbf{E}_k(\omega) + b\mathbf{E}_i(\omega)\mathbf{E}_j(\omega)\mathbf{E}_j(\omega) + c\mathbf{E}_i(\omega)\mathbf{E}_l(\omega)\mathbf{E}_l(\omega)] \quad (2.25)$$

utilizing the definition of the dot product, we find a simple expression for third order polarization,

$$\begin{aligned} \mathbf{P}_i^{(3)}(3\omega) &= \frac{\epsilon_o}{4}\chi_{xxxx}^{(3)}[\mathbf{E}(\omega) \cdot \mathbf{E}(\omega)]\mathbf{E}_i(\omega) \\ &= \frac{\epsilon_o}{4}\chi_{xxxx}^{(3)}E^2(\omega)\mathbf{E}_i(\omega) \end{aligned} \quad (2.26)$$

One of the interesting properties of THG is that $\mathbf{P}_i^{(3)}(3\omega)$ is identically to zero for circular polarized light. Consider an input fundamental field in a linearly-polarized basis given by

$$\mathbf{E} = \{ \hat{\mathbf{x}}A(\rho, z) + \hat{\mathbf{y}}B(\rho, z)e^{i\delta_0} \} \quad (2.27)$$

where $A(\rho, z)$ and $B(\rho, z)$ describe the spatial evolution of the x and y -polarized components, respectively. An initial phase offset is described by δ_0 . Note also, that k_1 is the wavenumber of the fundamental field. Inserting this into Eq. (2.26), through the dot product one easily shows that the THG polarization density is non-existent for a circularly-polarized light field [73]. Evaluating the dot product in Eq. (2.26), we find

$$\mathbf{E}(\omega) \cdot \mathbf{E}(\omega) = A^2 + B^2e^{i2\delta_0} \quad (2.28)$$

For circular polarization, where $A = B$, $\delta_0 = \pi/2, 3\pi/2$, the phase factor $e^{i2\delta_0} = -1$, which makes the dot product to be identically zero. Plugging this result into

Eq. (2.26) results in $\mathbf{P}_i^{(3)}(3\omega) = 0$.

Generally, due to the small magnitude of the third harmonic nonlinear susceptibility, THG signal from bulk of sample tend to be very small. For example, $\chi^{(3)} \sim 10^{-14} m^2/V^2$ for majority of solutions and $\chi^{(3)} \sim 10^{-17} m^2/V^2$ for gases has been reported [74]. Also, another interesting property for THG is that under focusing conditions, due to the Gouy phase shift, in the homogenous material there will be no third harmonic signal [66, 30], as destructive interference causes signal created before and after the focus cancel out. However, as Barad and Tsang has shown, if we break the symmetry, e.g in the case of interfaces, significant amount of THG will be observed[15, 75]. SHG and THG under focusing conditions will be described in next section.

2.3 The Propagation Equation

In this section we derive the non-linear propagation equation for the slowly varying envelope of an electric field. There will be three major assumptions made in the derivation: The first assumption is propagation inside a homogenous medium of non-interacting particles. The second assumption will be on the focussing condition of the the beam. We will assume propagation under moderate focusing conditions, i.e the spot size of the beam is always much larger than the wavelength of the field. Finally, we will assume that the contribution of the backward propagation field is negligible, i.e., slow varying approximation will be made [76].

Starting with the Maxwell's Equations [77]:

$$\nabla \cdot \mathbf{D}(\mathbf{r}, t) = \rho \quad (2.29)$$

$$\nabla \cdot \mathbf{B}(\mathbf{r}, t) = 0 \quad (2.30)$$

$$\nabla \times \mathbf{E}(\mathbf{r}, t) = -\frac{\partial \mathbf{B}(\mathbf{r}, t)}{\partial t} \quad (2.31)$$

$$\nabla \times \mathbf{H}(\mathbf{r}, t) = \mathbf{J}(\mathbf{r}, t) + \frac{\partial \mathbf{D}(\mathbf{r}, t)}{\partial t} \quad (2.32)$$

$$(2.33)$$

where $\mathbf{D}(\mathbf{r}, t)$ is the displacement field, ρ is the charge density, $\mathbf{B}(\mathbf{r}, t)$ is the magnetic induction, $\mathbf{E}(\mathbf{r}, t)$ is the electric field, $\mathbf{H}(\mathbf{r}, t)$ is the magnetic field, and $\mathbf{J}(\mathbf{r}, t)$ is the induced current density. By taking the curl of the Faraday's law, Eq. (2.31),

$$\nabla \times \nabla \times \mathbf{E}(\mathbf{r}, t) = -\nabla \times \frac{\partial \mathbf{B}(\mathbf{r}, t)}{\partial t} \quad (2.34)$$

and assuming a nonmagnetic medium, and using Ampere's Law (Eq. 2.32), the wave equation becomes,

$$\nabla \times \nabla \times \mathbf{E}(\mathbf{r}, t) = -\mu_0 \left[\frac{\partial \mathbf{J}(\mathbf{r}, t)}{\partial t} + \frac{\partial^2 \mathbf{D}(\mathbf{r}, t)}{\partial t^2} \right] \quad (2.35)$$

Where μ_0 is the permeability. Next, by substituting for $\mathbf{D}(\mathbf{r}, t) = \epsilon \mathbf{E}(\mathbf{r}, t) + \mathbf{P}(\mathbf{r}, t)$, with $\epsilon_0 \equiv 1/c^2 \mu_0$ the permittivity of free space and $\mathbf{P}(\mathbf{r}, t)$ the induced polarization,

$$\nabla \times \nabla \times \mathbf{E}(\mathbf{r}, t) + \frac{1}{c^2} \frac{\partial^2 \mathbf{E}(\mathbf{r}, t)}{\partial t^2} = -\mu_0 \left[\frac{\partial \mathbf{J}(\mathbf{r}, t)}{\partial t} + \frac{\partial^2 \mathbf{P}(\mathbf{r}, t)}{\partial t^2} \right] \quad (2.36)$$

This is the most general form of the wave equation in nonlinear optics. Usually, we are interested in regions of space that contains no free charges ($\rho = 0$) and no free current ($\mathbf{J} = 0$). Then,

$$\nabla \times \nabla \times \mathbf{E}(\mathbf{r}, t) + \frac{1}{c^2} \frac{\partial^2 \mathbf{E}(\mathbf{r}, t)}{\partial t^2} = -\mu_0 \frac{\partial^2 \mathbf{P}(\mathbf{r}, t)}{\partial t^2}. \quad (2.37)$$

Moreover, under certain conditions, we can make further simplifications. For example, by using the identity from vector calculus, we can write the first term on the left-hand side of Eq.(2.36) as $\nabla \times \nabla \times \mathbf{E}(\mathbf{r}, t) = \nabla [\nabla \cdot \mathbf{E}(\mathbf{r}, t)] - \nabla^2 \mathbf{E}(\mathbf{r}, t)$. For homogeneous, isotropic material $\nabla \cdot \mathbf{E}(\mathbf{r}, t)$ vanishes identically. So,

$$\nabla^2 \mathbf{E}(\mathbf{r}, t) - \frac{1}{c^2} \frac{\partial^2 \mathbf{E}(\mathbf{r}, t)}{\partial t^2} = \frac{1}{\epsilon_0 c^2} \frac{\partial^2 \mathbf{P}(\mathbf{r}, t)}{\partial t^2} \quad (2.38)$$

It is often convenient to split \mathbf{P} into its linear and nonlinear parts, as $\mathbf{P} = \mathbf{P}^{(1)} + \mathbf{P}^{(NL)}$. Here $\mathbf{P}^{(1)}$ is the part of the polarization that depends linearly on the electric field. Then, Eq. (2.38) becomes,

$$\nabla^2 \mathbf{E}(\mathbf{r}, t) - \frac{1}{\epsilon_0 c^2} \frac{\partial^2 \mathbf{D}^{(1)}(\mathbf{r}, t)}{\partial t^2} = \frac{1}{\epsilon_0 c^2} \frac{\partial^2 \mathbf{P}^{(NL)}(\mathbf{r}, t)}{\partial t^2} \quad (2.39)$$

where we have used $\mathbf{D}^{(1)} = \epsilon_0 \mathbf{E} + \mathbf{P}^{(1)}$. In case of lossless and dispersionless medium, we can express the relationship between $\mathbf{D}^{(1)}$ and \mathbf{E} in terms of real and frequency independent dielectric tensor $\epsilon^{(1)}$. Moreover, assuming an isotropic medium we can write ,

$$\mathbf{D}^{(1)}(t) = \epsilon_0 \epsilon^{(1)} \mathbf{E}(t) \quad (2.40)$$

where $\epsilon^{(1)} = n^2$ is scalar quantity, which is dimensionless and has a different value for each material. Hence, for an isotropic, dispersionless material, our wave equation becomes,

$$-\nabla^2 \mathbf{E}(\mathbf{r}, t) + \frac{\epsilon^{(1)}}{c} \frac{\partial^2 \mathbf{E}(\mathbf{r}, t)}{\partial t^2} = -\frac{1}{\epsilon_0 c^2} \frac{\partial^2 \mathbf{P}^{(NL)}(\mathbf{r}, t)}{\partial t^2} \quad (2.41)$$

2.3.1 Monochromatic Light

Although in nonlinear optics we are often concerned with interaction of short pulses with the medium, it is a common practice to consider the bandwidth of a the pulse to be small (with respect to the carrier frequency). Hence, we can assume our field to be approximated with superposition of time harmonic plane waves oscillating at a set of discrete frequencies ω_n .

$$\mathbf{E}(\mathbf{r}, t) = \sum_n \mathbf{E}_n(\mathbf{r}, t) \quad (2.42)$$

$$\mathbf{P}(\mathbf{r}, t) = \sum_m \mathbf{P}_m(\mathbf{r}, t) \quad (2.43)$$

where the summation is performed over positive frequencies only. If we represent each frequency component in terms of its complex amplitude as,

$$\mathbf{E}_n(\mathbf{r}, t) = \mathbf{E}_n(\mathbf{r})e^{-i\omega_n t} + c.c., \quad (2.44)$$

$$\mathbf{P}_m(\mathbf{r}, t) = \mathbf{P}_m(\mathbf{r})e^{-i\omega_m t} + c.c., \quad (2.45)$$

By inserting Eq. (2.43) into (2.41), we find,

$$-\sum_n \nabla^2 \mathbf{E}_n(\mathbf{r})e^{-i\omega_n t} + \frac{\omega_n^2 \epsilon_n^{(1)}}{c} \sum_n \mathbf{E}_n(\mathbf{r})e^{-i\omega_n t} = -\frac{1}{\epsilon_0 c^2} \sum_m \mathbf{P}_m^{(NL)}(\mathbf{r})e^{-i\omega_m t}. \quad (2.46)$$

Evaluating the above, term by term, we find

$$\nabla^2 \mathbf{E}_n(\mathbf{r}) - \frac{\omega_n^2 \epsilon_n^{(1)}}{c} \mathbf{E}_n(\mathbf{r}) = \frac{\omega_m^2}{\epsilon_0 c^2} \mathbf{P}_m^{(NL)}(\mathbf{r})e^{-i(\omega_m - \omega_n)t}. \quad (2.47)$$

For stationary, time-independent solutions, only $\omega_m = \omega_n$ survive. Moreover, for

$\omega_m \neq \omega_n$ there will be no time-averaged power transfer from the incident field to the induced polarization, and we have,

$$\nabla^2 \mathbf{E}_n(\mathbf{r}) - \frac{\omega_n^2 \epsilon_n^{(1)}}{c} \mathbf{E}_n(\mathbf{r}) = \frac{\omega_m^2}{\epsilon_0 c^2} \mathbf{P}_n^{(NL)}(\mathbf{r}) \quad (2.48)$$

Next, we represent the electric field and the polarization in terms of their slowly varying amplitudes, as

$$\mathbf{E}_n(\mathbf{r}) = \frac{1}{2} \{ \mathbf{A}_n(\mathbf{r}) e^{ik_n z} + c.c. \}, \quad (2.49)$$

$$\mathbf{P}_n(\mathbf{r}) = \frac{1}{2} \{ \mathbf{p}_n(\mathbf{r}) e^{ik'_n z} + c.c. \}. \quad (2.50)$$

where, \mathbf{A}_n and \mathbf{p}_n are spatially varying complex quantities. Here the prime on the polarization wave-vector emphasizes on possible wavevector mismatch between the field and the induced polarization. Next, we substitute Eq. (2.49,2.50) into Eq. (2.48),

$$\nabla^2 \mathbf{A}_n(\mathbf{r}) e^{ik_n z} - \frac{\omega_n^2 \epsilon_n^{(1)}}{c} \mathbf{A}_n(\mathbf{r}) e^{ik_n z} = \frac{\omega_m^2}{\epsilon_0 c^2} \mathbf{p}_n^{(NL)}(\mathbf{r}) e^{ik'_n z} \quad (2.51)$$

Separating the laplacian in terms of the transverse and longitudinal part, $\nabla^2 = \nabla_T^2 + \frac{\partial^2}{\partial z^2}$, where $\nabla_T^2 = \frac{\partial^2}{\partial x^2} + \frac{\partial^2}{\partial y^2}$, we can rewrite Eq. (2.51) as,

$$\nabla_T^2 \mathbf{A}_n(\mathbf{r}) e^{ik_n z} + \frac{\partial^2}{\partial z^2} \mathbf{A}_n(z) e^{ik_n z} - \frac{\omega_n^2 \epsilon_n^{(1)}}{c} \mathbf{A}_n(\mathbf{r}) e^{ik_n z} = \frac{\omega_m^2}{\epsilon_0 c^2} \mathbf{p}_n^{(NL)}(\mathbf{r}) e^{ik'_n z} \quad (2.52)$$

After evaluating $\frac{\partial^2}{\partial z^2} \mathbf{A}_n(z) e^{ik_n z} = \frac{\partial^2 \mathbf{A}_n}{\partial z^2} + 2ik_n \frac{\partial \mathbf{A}_n}{\partial z} - k_n^2 \mathbf{A}_n$, and using the slow varying amplitude approximation, stating $\mathbf{A}_n(z)$ varies slow with respect to z ,

$$\left| \frac{\partial^2}{\partial z^2} \mathbf{A}_n(z) \right|^2 \ll \left| k_n \frac{\partial \mathbf{A}_n(z)}{\partial z} \right|^2 \quad (2.53)$$

,

and using the relationship $k_n = \frac{n\omega_n}{c}$ with $n^2 = \epsilon_n^{(1)}$, and transforming back to temporal domain we find

$$2ik_n \frac{\partial \mathbf{A}_n}{\partial z} + \nabla_T^2 \mathbf{A}_n = -\frac{\omega_n^2}{\epsilon_0 c^2} \mathbf{P}_n e^{i\Delta k z} \quad (2.54)$$

where $\Delta k = k'_n - k_n$. Equation (2.54) describes propagation of each frequency component of electromagnetic, under slow varying envelope approximation.

2.3.2 Second Harmonic and Third Harmonic Generation under Focusing Conditions

Now, we will consider the generation of SHG and THG under focusing conditions of Gaussian beams. Let us consider an intense monochromatic electric field incident on a material inducing polarization inside the medium described by Eq. (2.2). The induced polarization, in turn, will create a new field according to Eq. (2.54). For instance, let us assume that an time-harmonic plane wave incident field,

$$\mathbf{E}_\omega(\mathbf{r}, t) = \frac{1}{2} \{ \mathbf{A}_1(\mathbf{r}) e^{i(k_\omega z - \omega t)} + c.c \} \quad (2.55)$$

induces a third harmonic polarization,

$$\mathbf{P}^{(3)}(\mathbf{r}, t) = \frac{1}{2} \{ \mathbf{p}_3(\mathbf{r}) e^{i(3k_\omega z - 3\omega t)} + c.c \} \quad (2.56)$$

where, $\mathbf{p}_3(\mathbf{r})$ is given by Eq. (2.26). Then, Eq. (2.54) describes the propagation of the third harmonic envelope of the field as,

$$\begin{aligned}
2ik_3 \frac{\partial \mathbf{A}_3}{\partial z} + \nabla_T^2 \mathbf{A}_3 &= -\frac{\omega_3^2}{\epsilon_0 c^2} \mathbf{P}_3 e^{i\Delta k z} \\
&= -\frac{\omega_3^2}{4\epsilon_0^2 c^2} \chi^{(3)} \mathbf{A}_1^3 e^{i\Delta k z}
\end{aligned} \tag{2.57}$$

where in Eq. (2.58) the dependence on spatial coordinate is still implied. Here $\Delta k = 3k_\omega - k_{3\omega}$ is the phase mismatch between the third harmonic and the fundamental field. The subscripts 1 and 3 in Eq. (2.58) signifies the fundamental and third harmonic frequency. Also, note that in writing \mathbf{A}_1^3 we have assumed a linear polarized incident field.

In most practical cases, the incident field is a focused laser beam, with a Gaussian spatial profile given by [31],

$$\mathbf{A}_1(r; z) = \frac{A_{10}}{B_1} \exp \left\{ -\frac{r^2}{w_{10}^2 B_1} \right\} \tag{2.58}$$

with

$$B_1 = 1 + \frac{2iz}{w_{10}^2 k_1} \tag{2.59}$$

Here, A_{10} represent the amplitude of the Gaussian beam at the waist $z = 0$, with a waist radius of w_{10} . In the same way, the spatial profile of the THG beam can be written as,

$$\mathbf{A}_3(r; z) = \frac{A_{30}}{B_3} \exp \left\{ -\frac{r^2}{w_{30}^2 B_3} \right\} \tag{2.60}$$

with

$$B_3 = 1 + \frac{2iz}{w_{30}^2 k_3} \tag{2.61}$$

In general, for any q^{th} harmonic, if present, we can express the spatial variation of the amplitude of the induced field by a Gaussian beam as,

$$\begin{aligned} \mathbf{A}_q(r; z) &= \frac{A_{q0}}{\left[1 + \frac{i2z}{w_{q0}^2 k_q}\right]} \exp\left\{-\frac{(r^2)}{w_{q0}^2 \left[1 + \frac{i2z}{w_{q0}^2 k_q}\right]}\right\} \\ &= \frac{A_{q0}}{(1 + i\zeta)} \exp\left\{-\frac{(r^2)}{w_{q0}^2 (1 + i\zeta)}\right\} \end{aligned} \quad (2.62)$$

Here, $\zeta = 2z/b$ is a dimensionless longitudinal coordinate defined in terms of the confocal parameter, $b = 2\pi w_{q0}^2/\lambda_q = k_q w_{q0}^2$, which is the measure of the longitudinal extent of the focal region of the gaussian beam. Figure. A.1, illustrate this quantity. The subscript q illustrate the order of harmonic of the initial gaussian beam.

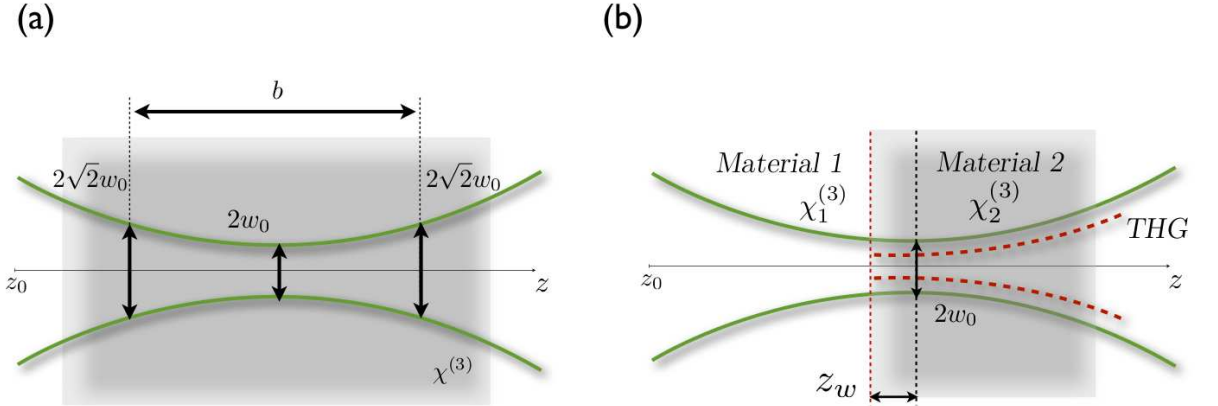


Figure 2.2: Geometry of a Gaussian beam focused (a) inside a bulk material and (b) on an interface of two material with different third order susceptibilities.

A description of the evolution of $\mathbf{A}_q(r; z)$ in the medium can be found by substitution of Eq. (A.14) in Eq. (2.2) [31]. The details and the solution to Eq. (2.2) are presented in Appendix A and will be summarized here.

As described in Appendix A, the solution to Eq. (2.2) for a focused Gaussian beam inside medium with $\chi^{(q)}$, is given by,

$$A_{q0}(z) = iq \frac{\omega_1 \chi^{(q)} A_{10}^q}{2n_q c} \int_{z_0}^z \frac{e^{i\Delta k z'}}{\left[1 + \frac{i2z}{w_{10}^2 k_1}\right]^{q-1}} dz' \quad (2.63)$$

or equivalently,

$$A_{q0}(z) = iq \frac{\omega_1 \chi^{(q)} A_{10}^q}{2n_q c} J_q(\Delta k; z_0; z) \quad (2.64)$$

where,

$$J_q(\Delta k; z_0; z) = b \int_{z_0/b}^{z/b} \frac{e^{i\Delta k b z'}}{(1 + i2z')^{q-1}} dz' \quad (2.65)$$

is the q^{th} harmonic interaction length and z_0 is the position of the entrance of the medium and $\Delta k = qk_\omega - k_\omega$. Also, $z = 0$ is the location of the waist of the beam, c is the speed of light. The solution to Eq. (2.65), in the case of infinite, uniform nonlinear medium can be calculated analytically through contour integration (See Appendix A) and is given by,

$$J_q(\Delta k; z_0; z) = \begin{cases} 0 & \text{for } \Delta k < 0 \\ \frac{\pi b}{(q-2)!} \left(\frac{\Delta k b}{2}\right)^{q-2} e^{-\Delta k b/2} & \text{for } \Delta k > 0 \end{cases} \quad (2.66)$$

Equation (2.66) tells us that the interaction length of the q^{th} harmonic field, depends on the focusing conditions (through b) and phase matching condition (through Δk). Moreover, for any q^{th} harmonic, the interaction length, and therefore far field intensity, is null when $\Delta k \leq 0$, which is true for all material that possess normal dispersion $n_{q\omega} > n_\omega$ (Note that Eq. (2.66) does not hold for $q = 2$ (SHG), where through phase matching will result in a nonzero interaction length).

Figure 2.3 illustrates the Interaction length for SHG and THG for a specific focusing condition ($NA = 1; \lambda = 1\mu m$). As expected, for the SHG, maximum interaction length value is achieved for perfect phase matching $\Delta k = 0$. A more surprising result

is that the interaction length for THG is only non-zero when $\Delta k > 0$. This phenomena has been explained to be a result of Gouy phase shift that the phase of the fundamental field experiences under focusing conditions.

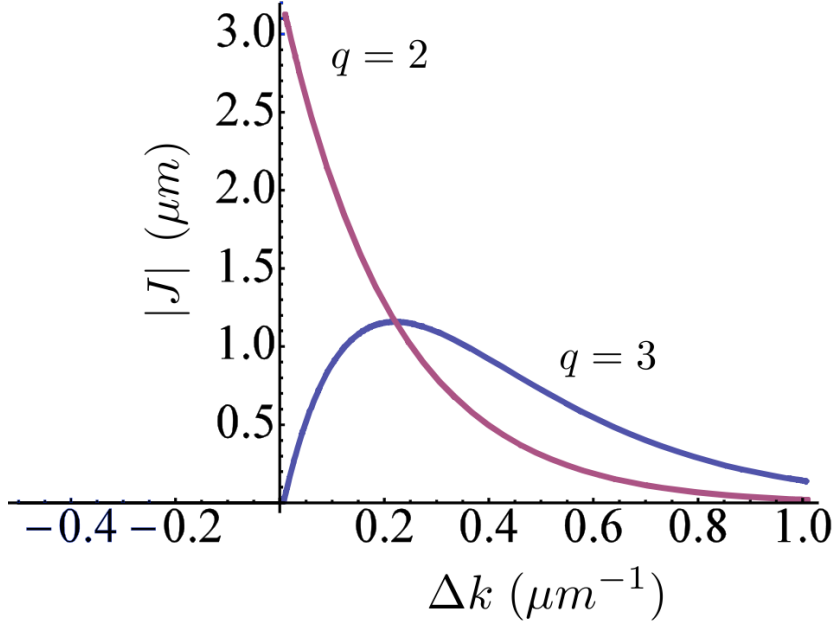


Figure 2.3: Interaction length for second and third harmonic versus phase matching.

However, as Barad and Tsang has shown, if we break the symmetry, e.g in the case of interfaces, significant amount of THG will be observed [15, 75]. Under this condition shown in Fig. A.1(b), a significant amount of third harmonic field will be detected at the far field no matter what kind of phase matching conditions we might have at hand.

Barad *et.al* took this idea and applied it to microscopy, and showed that THG of interfaces can be used as a contrast mechanism in nonlinear microscopy [15]. They also showed that the radiated third harmonic power at an interface is proportional to the square of the difference between the between the third order susceptibilities, or

$$\begin{aligned}
P_3 &= \frac{n_3 c \epsilon_0}{2} \int_0^\infty \int_0^{2\pi} |\mathbf{A}_3(r; z)|^2 d\theta dr \\
&\propto \frac{\delta\chi^2}{\left(1 + \frac{4z_w^2}{b^2}\right)}
\end{aligned} \tag{2.67}$$

where $\delta\chi = \left| \chi_2^{(3)} - \chi_1^{(3)} \right|$ is the difference between susceptibilities of the two medium, and z_w is the distance between the interface and the beam waist.

2.4 Green's Function Formulation for Far-Field Non-linear Signal

In section 2.3.2 we presented a two-dimensional model of q^{th} harmonic generation under focusing conditions of Gaussian beam onto a sample. In this section we will introduce a three-dimensional calculation of nonlinear optical signal generation. In particular, we will investigate the far-field calculation of SHG and THG in an isotropic sample [78, 79, 80, 81].

Figure (2.4), illustrates a 3-D geometry for focusing and nonlinear radiation [80, 81]. It is assumed that the incident beam $\mathbf{E}_0^{\text{inc}}(\mathbf{r}_0, t) = \mathbf{A}_0^{\text{inc}}(\mathbf{r}_0) e^{i(\omega_0 t - k_0 z)}$ illuminating the sample is linearly polarized along the x -axis, oscillating at frequency ω_0 , has a Gaussian spatial profile $\mathbf{A}_0^{\text{inc}}(\mathbf{r}_0)$, and propagating along the z -axis. Inside the medium, the fundamental field drives a polarization density oscillating at second and/or third-harmonic of the incident field given by

$$\mathbf{P}^{(2)}(\mathbf{r}_0) = \frac{1}{2} \epsilon_0 \chi^{(2)}(\mathbf{r}_0) \mathbf{A}_0^{\text{inc}}(\mathbf{r}_0) \mathbf{A}_0^{\text{inc}}(\mathbf{r}_0) \tag{2.68}$$

for generation of second harmonic signal, and

$$\mathbf{P}^{(3)}(\mathbf{r}_0) = \frac{1}{4}\epsilon_0\chi_{1111}^{(3)}(\mathbf{r}_0) [\mathbf{A}_0^{\text{inc}}(\mathbf{r}_0) \cdot \mathbf{A}_0^{\text{inc}}(\mathbf{r}_0)] \mathbf{A}_0^{\text{inc}}(\mathbf{r}_0) \quad (2.69)$$

for third harmonic generation. The nonlinear optical susceptibilities $\chi^{(2)}(\mathbf{r}_0)$ and $\chi^{(3)}(\mathbf{r}_0)$ are tensors, whose elements are dictated by the material of the object. Here $\mathbf{r}_0 = x_0\hat{\mathbf{i}} + y_0\hat{\mathbf{j}} + z_0\hat{\mathbf{k}}$ is the spatial coordinate in the object space. If we assume that the nonlinear signal emerging from an object, at some distance \mathbf{r} , is a coherent superposition of nonlinear radiation of induced dipoles inside the sample, we can calculate the nonlinear radiation $\mathbf{E}^{\text{obj}}(\mathbf{r})$ which contains encoded information on 3-D spatial structure of the object, by using Green's function formalism [78],

$$\mathbf{E}^{\text{obj}}(x, y, z) = -\mu_0\omega_q^2 \int \int \int_V \mathbf{G}_0(\mathbf{r}, \mathbf{r}_0) \cdot \mathbf{P}^{(q)}(\mathbf{r}_0) dx_0 dy_0 dz_0 \quad (2.70)$$

where we assume $z \gg z_0$, $\omega_q = q\omega_0$, $k_q = \omega_q n/c$. The dyadic Green's function is given by

$$\mathbf{G}_0(\mathbf{r}, \mathbf{r}_0) = \frac{e^{ik_q r}}{4\pi r} e^{-ik_q(x x_0/r + y y_0/r + z z_0/r)} \begin{bmatrix} (1 - x^2/r^2) & -xy/r^2 & -xz/r^2 \\ -xy/r^2 & (1 - y^2/r^2) & -yz/r^2 \\ -xz/r^2 & -xy/r^2 & (1 - z^2/r^2) \end{bmatrix}, \quad (2.71)$$

where $r = \sqrt{x^2 + y^2 + z^2}$.

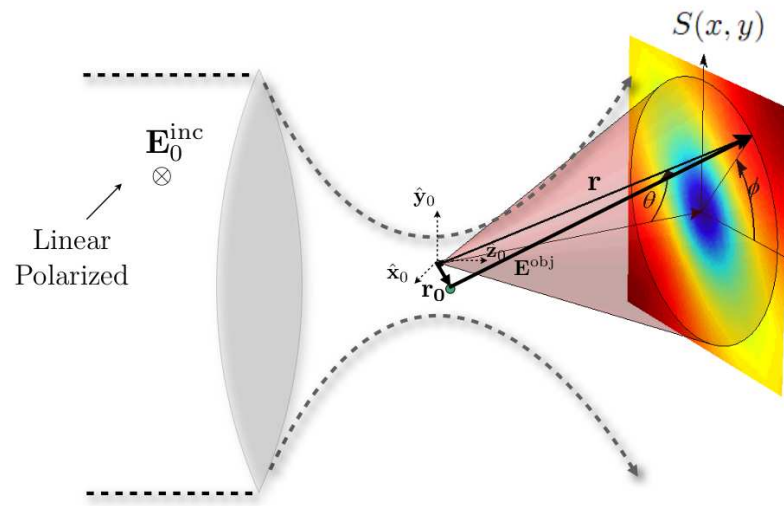


Figure 2.4: Illustration of nonlinear object field generation, and its far-field detection, with definitions of the parameters of the excitation and detection coordinate systems.

Chapter 3

Nonlinear Microscopy

The evolution of optical microscopy has always been driven by the desire to improve the resolution and search for new imaging contrast mechanisms to reveal previously unobservable features. Although tremendous progress has been made in conventional optical microscopy, notably confocal [8, 9], it has suffered from a low physical and chemical specificity [10]. This motivated the development of techniques like two-photon fluorescence, second harmonic generation (SHG), and third harmonic generation (THG) microscopy, and coherent anti-Stokes Ramon spectroscopy (CARS) [11, 22, 82, 16, 15, 83, 84].

The evolution of contemporary nonlinear microscopy started by the pioneering work of Denk and Webb [11], with their demonstration of two-photon excitation fluorescent microscopy, a subset of multi-photon excitation microscopy. Through focusing of subpicosecond lasers, they showed that by concentrating the laser field into a small spot, using a microscope objective, the emitted fluorescent light would originate from localized focal volume or voxel. The implication of this technique was tremendous, including deeper tissue penetration and less photodamage [11, 22, 82]. Moreover, they showed that by scanning the laser across the sample in (x, y, z) dimensions, 3-dimensional images could be constructed.

3.1 Nonlinear Laser Scanning Microscopy

The contrast in nonlinear optical microscopy arises from multiphoton interaction of a laser with a sample. To understand how this is advantageous, consider the difference between single photon and two-photon excitation (TPE) microscopes. In single photon fluorescence microscopy, the excitation field promotes an electron to an excited state by absorbing a photon with a certain probability which depends on the intensity of the excitation focused beam. After the electron goes through some vibrational/rotational relaxation, it returns to the ground state some time later and releases its energy by emitting a fluorescence photon. Usually, the excitation process requires photons in the ultraviolet or blue/green spectral region. In TPE, the incident field requires two photons with less photon energy, typically in the infrared spectral range, to promote to the same electronic state. Therefore the probability of two photon absorption is proportional to square of the excitation intensity. This process, however, requires intense laser illumination which is achieved by focusing the beam into a small spot, which limits the induced signal to a small volume. Hence the name nonlinear laser scanning microscopy. The success of laser scanning two-photon microscopy has become a laboratory standard and opened doors to many other nonlinear modality like SHG [13, 14], THG [15, 16], CARS [17, 18].

Due to several intrinsic advantages which arise as a result of having nonlinear intensity dependence, nonlinear microscopy has become an important tool for the imaging of biological tissues. Most biological tissues strongly scatter light, making deep optical imaging impossible [85]. In contrast to single photon microscopy, nonlinear techniques enables the use of longer wavelengths, reducing the scattering in the samples and extends the imaging depth from tens of microns to several hundred of

microns [86].

The strong dependence of the excitation probability on the excitation intensity causes signal in nonlinear imaging restricted to the focal volume. For instance, for focused excitation field, the excitation probability outside the focal volume falls off with z^{-2q} , where z is the distance from the focal plane and q is the number of photons absorbed [87], as a consequence provides excellent depth discrimination.

Moreover, this intensity dependence improves the spatial resolution, since the effective point-spread function is smaller. In conventional linear microscopic techniques the signal response depends linearly on the input intensity, hence the illuminated sample volume contributes equally to the incident field, whether it is in or out-of-focus. The use of a confocal pinhole suppresses the contributions from out-of-focus planes permitting optical sectioning of the sample and improves the axial resolution [8]. Nonlinear optical microscopy applications, on the other hand, have inherent optical sectioning capability. Even without the use of a confocal pinhole, these microscopic techniques provide three-dimensional imaging capability [11].

The efficiency of nonlinear microscopy depends on physical and molecular properties explained in chapter 2, and on the spatial and temporal distribution of the excitation light. Most nonlinear processes have a very low transition probabilities, and strong intensities are needed. To generate sufficient signal, excitation light has to be concentrated in both space and time, by utilizing high numerical aperture objective and use of ultra-short pulses receptively. For a given average power, laser pulses of width τ_p at repetition rates f_R can enhanced the signal by a factor of $(\frac{1}{\tau_p f_R})^{(N-1)}$ compared to cw illumination, where N is the number of photons involved in the nonlinear process [10].

In this chapter, we will mostly concentrate on the class of, coherent, parametric nonlinear optical processes. Parametric processes can always be described by a real susceptibility [31]. This results in the absence of a net energy transfer to the specimen,

hence lowering the probability of destroying the sample. In a coherent process, phase and polarization during the nonlinear conversion are conserved. Harmonic generation and stimulated Raman scattering are examples of parametric, coherent processes.

3.1.1 Resolution

The optical resolution is usually defined through the Rayleigh criterion, which states that two point sources with equal intensity can be just resolved when the principle intensity maximum of one coincides with the first minimum of the other [88]. This is depicted in Fig 3.2. In signal processing, the response of the system to an input is characterized by its impulse response. In a similar way, image formation in any optical system is described by a point spread function (*PSF*), that is the image of a point [89]. Using *PSF*, the image of any object can be characterized by convolving the object distribution with the *PSF*. The *PSF* of an imaging system depends on whether the imaging is done with coherent or incoherent light. In a coherent imaging, the relative phase between the signal from the entire sample vary in time in a correlated way [89]. In scanning laser microscopy however, this does not hold, since there is no phase relation between each imaged point—even with coherent nonlinear treatments such as SHG or THG. Therefore the imaging is considered as incoherent.

The *PSF* depends on the wavelength and the numerical aperture *NA*. Assuming an aberration-free system (most theoretical models in optical microscopy assume aberration free systems) with a circular aperture (microscope objective have exclusively circular apertures) and under paraxial approximations, the 3-D complex amplitude *PSF* of a lens is given by the Hankel transform, [88, 89],

$$h(u, v) = 2 \int_0^1 P(\rho) J_0(v\rho) \exp(iu\rho^2/2) \rho d\rho \quad (3.1)$$

Here, J_0 is the zeroth-order Bessel function of the first kind, ρ is the radial coor-

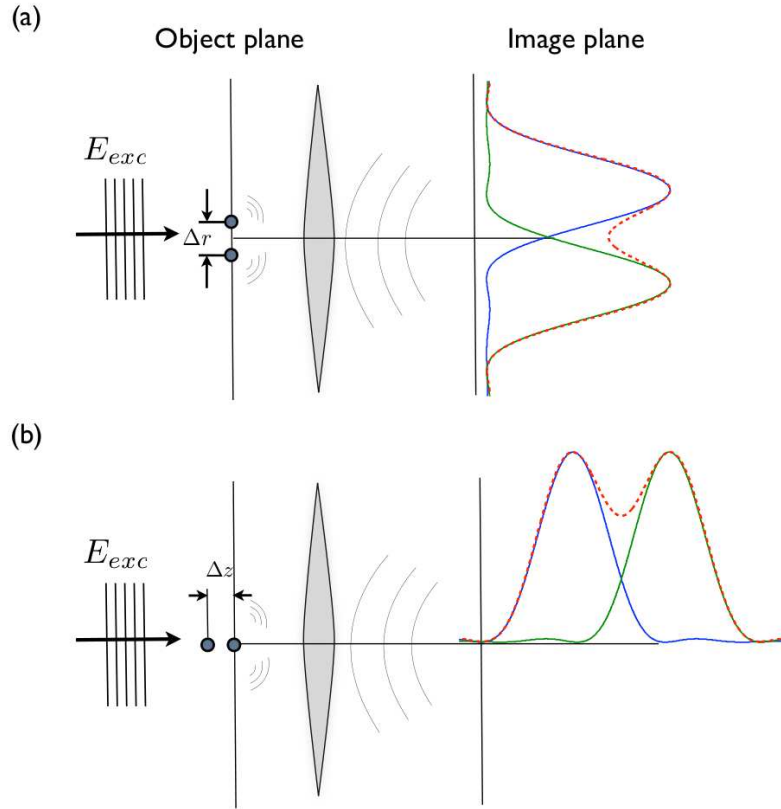


Figure 3.1: (a) Radial resolution, is the ability of resolving two points sources separated by a distance Δr , located on the axis perpendicular to the optical axis, and (b) axial resolution, is the ability of resolving two points sources separated by a distance Δz located on the optical axis

ordinate at the pupil P , normalized to the pupil radius a , and u, v are normalized, dimensionless optical coordinates,

$$v = r \frac{2\pi}{\lambda} \sin(\theta) \quad (3.2)$$

$$u = z \frac{8\pi}{\lambda} \sin(\theta/2)^2 \quad (3.3)$$

with $r = \sqrt{x^2 + y^2}$ and z are the radial (in the x, y focal plane) and axial (the distance between the focal point along the optical axis) coordinate, respectively, and θ denoted the acceptance cone of light (angle that defines the numerical aperture

$NA = n \sin(\theta)$). Here λ denoted the optical wavelength in the objective.

The *IPSF* of a scanning microscope is given by intensity point spread function or intensity impulse function, $|h(u, v)|^2$, and the image intensity of an incoherent object I_i is,

$$I_i = |h(u, v)|^2 \otimes I_o \quad (3.4)$$

where $I_o(u, v)$ is the intensity transmittance of an object (i.e the intensity of the fluorescence signal emitted in fluorescence imaging).

Axial *IPSF* can be calculated by setting $r = 0$ corresponding to $v = 0$,

$$IPSF_z(u, 0) = |2 \int_0^1 \exp(iu\rho^2/2) \rho d\rho|^2 = \text{sinc}^2\left(\frac{u}{4\pi}\right) \quad (3.5)$$

and the lateral *IPSF* is given by setting $z = 0$,

$$IPSF_r(0, v) = |2 \int_0^1 J_0(\rho v) \rho d\rho|^2 = \left|\frac{2J_1(v)}{v}\right|^2 \quad (3.6)$$

In the normalized optical coordinate (v, u) the first node in these lateral and axial distributions is at $v_0 = 1.22\pi$ and $u_0 = 4\pi$ respectively. In the real units the first nodes are found to be,

$$r_0 = \frac{0.61\lambda}{NA} \quad (3.7)$$

$$z_0 = \frac{2n\lambda}{NA^2} \quad (3.8)$$

Equation (3.8) describes the optical resolution of a moderate numerical aperture microscope objective, where paraxial approximation has been assumed.

The enhanced resolution has been shown [86] by considering a general spatial gaussian distribution on the input beam with a waist size w_0 ,

$$I(r) = I_0 \exp \left[- \left(\frac{x}{w_0} \right)^2 \right]. \quad (3.9)$$

Then it follows that for a N^{th} order process we have,

$$I^N(r) = I_0^N \exp \left[- \left(N \frac{x}{w_0} \right)^2 \right] \quad (3.10)$$

$$I^N(r) = I_0^N \exp \left[- \left(\frac{x}{w_N} \right)^2 \right]$$

where $w_N = w_0/\sqrt{N}$ is the waist for the N^{th} order process, which has reduced with a factor of \sqrt{N} . Therefore, the effective point spread function is $IPSF(r)^{(N)} = [IPSF(r)^{(1)}]^N$, and we have an enhanced resolution by a factor of \sqrt{N} . For example, for a second order process (SHG), the interaction area will decrease with a factor of 2 and for a third order process (THG), the interaction area decreases by a factor of 3.

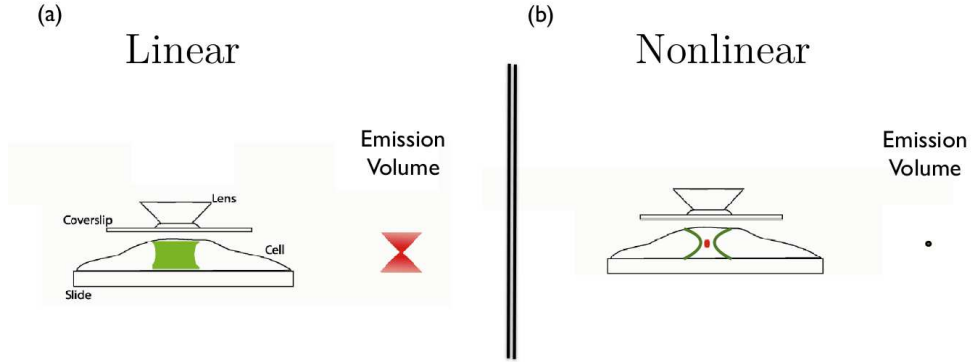


Figure 3.2: Interaction volume: (a) Single-photon excitation, where the emission probability depends on excitation intensity $I(r)$. (b) Two-photon excitation, where the emission probability depends on the square of the excitation intensity $I^2(r)$

For completeness, we should also mention that the resolution of the system also depends on the intensity distribution in the back aperture of the objective $P(\rho)$, the pupil function. For uniform distribution illumination $P(r) = 1$. For gaussian distri-

bution, the pupil function is given by $\exp(-(r/F)^2)$, where $F = D_{beam}/D_{BA}$ is the fill factor, indicating how much of the input beam area fills the back aperture. Here D_{beam} is the $1/e^2$ intensity width and D_{BA} the back-aperture diameter. Since the radial intensity profile of a laser beam is Gaussian, an exact match to an aperture is impossible. Therefore, certain compromise between resolution, which increases as the back aperture of the objective is increasingly filled, and throughput, which is maximal when the back aperture is under-filled [90]. For instance, when the back aperture of the objective is completely filled, power transmission is 86%. A further reduction of the beam size, increases the transmitted power while it broadens the focal volume.

3.1.2 Scattering in Living Tissues

In biological tissues, scattering and absorption (mostly due to water) of the fundamental light inside the tissue, can limit the deep tissue microscopy [85]. In most biological samples, in the visible to near infrared regime, the probability of scattering inside of a tissue is much higher than absorption. The mean free path between photon scattering events is on the order of 0.1 mm, whereas the mean absorption length can extend to 10 – 100 mm [12]. The likelihood of scattering depends on refractive index variation Δn , object size a , and wavelength λ . Scattering of light by a spherical particle of any size can be modeled by the Mie theory, which reduces to the simpler Rayleigh theory if the spherical particle is much smaller than the wavelength [12, 85, 10].

For isolated atoms and molecules, scattering is nearly isotropic and strongly wavelength dependent and is $\propto \lambda^{-4}$. In nonlinear optical microscopy only non-scattering photons that reach the focal volume (ballistic photon), contribute to signal. The ballistic power follows a Lambert-Beer-like exponential decline, which limits optical imaging depth z ,

$$P_{ball} = P_0 e^{-\mu_s z} \quad (3.11)$$

where μ_s is the scattering coefficient, defined as the probability of photon scattering in a medium per unit path length which has a representative value of 100cm^{-1} for biological tissue [85], and P_0 is the incident power. A table of scattering and absorption coefficient for different biological tissue can be found in [85].

Because of the quadratic or cubic dependence of SHG and THG respectively, the collected signal declines as $S_{SHG} \propto e^{-2\mu_s z}$ and $S_{THG} \propto e^{-3\mu_s z}$ [12, 85, 10]. Therefore, we need to exponentially increase laser power entering the surface ($P_0 \propto e^{\mu_s z}$) to maintain the same ballistic intensity at the focus to increase the penetration depth for imaging.

In many nonlinear microscopy experiments, the excitation occur in the near-infrared wavelength range (700 – 1500 nm), whereas emission occurs in the visible spectral range where most detection tools like CCD and photodiodes have been developed. It follows from the discussion above (scattering $\propto \lambda^{-4}$) one will see that at near-infrared, light penetrates deeper into scattering tissue. For instance, for THG microscopy using a laser with $\lambda_{ex} = 1500$ nm, we get an emission at $\lambda_{em} = 500$ nm. The calculation above shows that the scattering probability decreases by almost two orders of magnitude by using the longer excitation wavelength. Moreover, optical absorption in biological tissue is weak in the near-infrared spectral region.

With ultrashort lasers, it is very easy to create intensities required to induce nonlinearities like SHG and THG inside the tissues. Even with a modest focusing conditions, intensities up to $100\text{GW}/\text{cm}^2$ are achievable. Moreover, due to the short interaction lengths J inside of the cells ($J \approx 1 - 6$ um, depending on the focusing conditions), no phase matching is required [91], as J is less than the coherence length. For instance, we have observed significant amount of SHG in human cardiac muscle

tissue (The Microscope Store, LLC) using a home-built Yb:KGW laser oscillator operating around the wavelength 1026 nm, obtaining a 70 MHz train of pulses capable of delivering 14 nJ of pulse energy. We use only 4 nJ of this energy to focus into $35 \mu\text{m}$ $1/e^2$ radius, corresponding to $300 \text{ MW}/\text{cm}^2$ into the sample, which is well below a typical damage threshold of biological samples which, varies between tissue types, but has a typical value of $\sim 200 \text{ GW}/\text{cm}^2$ [92, 93, 94, 95]. Under this focusing condition we were able to take continuous SHG images for hours without observing any visual damage on the sample. Figure 3.3 shows the white light (a) and SHG (b) signal from these tissues. One can easily see how the nonlinearity in the sample generate a new contrast.

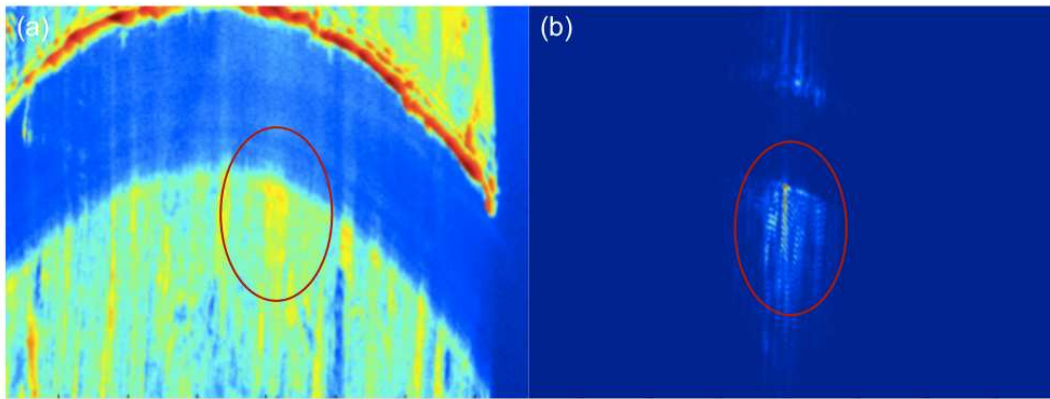


Figure 3.3: Contrast mechanism: imaging of human cardiac muscle using (a) White light microscopy. (b) SHG microscopy

3.1.3 Signal detection

The detection of the signal in nonlinear microscopy can be done with either a CCD camera, photomultiplier tube (PMT), or a photodiode, depending on the wavelength and the signal energy. Imaging detectors, like CCD cameras, are the easiest and most common detection tool to use when no scanning on the sample is done (wide field illumination). In scanning nonlinear microscopy though, imaging detectors are not

necessary.

Large area PMT's are the most common detectors in nonlinear microscopy. They enable efficient detection of single photons. Another alternative to PMT's are avalanche photodiodes, which possess higher quantum efficiencies than PMT's. They possess, however, very small active area [96].

Figure. 3.4 shows a typical nonlinear microscope setup. A laser beam from a mode-locked laser gets scanned by a galvonometric scanner and focused by a high numerical objective onto a sample which can be moved in x, y, z directions with a translational stage. The nonlinear signal from the sample then gets filtered by a combination of dichroic optics and/or bandpass filtering centered around the emission wavelength. The signal then gets collected by a detector.

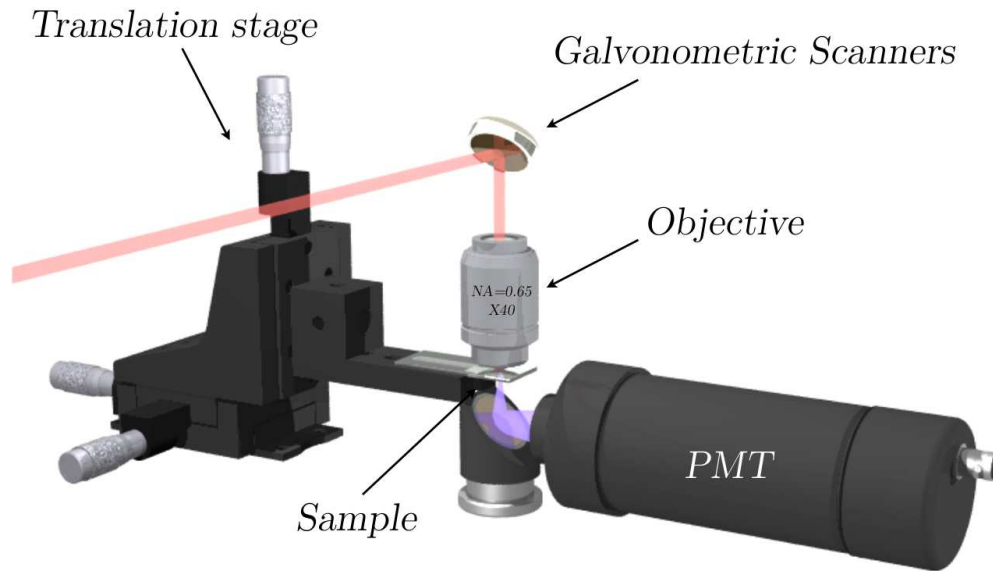


Figure 3.4: Typical microscope setup: The laser beam is scanned radially across the sample (x, y) with a galvonometric scanner and axially using translation stage. A microscope objective focuses the beam on the sample and the emitted light is recorded by a detector.

3.2 Second Harmonic Microscopy

Second harmonic generation as a contrast mechanism in microscopy was first proposed around 30 years ago [97, 98], and applied to biological samples in the 1980s [13, 14]. As explained in chapter 2, SHG describes the upconversion of an incident electromagnetic wave, with a frequency ν , into a frequency 2ν , and is originated through the second order susceptibility of the material. In biological samples, SHG requires specimen with noncentrosymmetric structure. Just like with TPE, the second harmonic signal produced in the sample depends on the square of the incident field [22, 23], which gives rise to its inherent optical sectioning. Since SHG is a coherent process, the phase of the emitted signal with respect to the excited field is conserved. Hence, it is predominantly radiated in the forward or backward direction, depending on the size and shape of the specimen [99, 100, 101, 102], rather than isotropically.

Although TPE and SHG are both two photon processes, there are some dissimilarities between the two. For instance, the contrast in SHG microscopy from tissues is produced purely from endogenous species, and no labeling is required. Moreover, the SHG signal arises from induced polarizability rather than absorption which can lead to photobleaching and phototoxicity.

The main advantage with SHG is, due to its contrast mechanism which is physical structure of the tissues. Biological materials that assemble into ordered noncentrosymmetric structures [13, 25] are known to allow SHG. Currently, SHG microscopy has been applied to biological tissues like collagen, mitotic spindles, actomyosin complexes, and microtubules (see the review by Campagnola and Loew [24]). For example, information about the molecular structure of proteins can be easily extracted from SHG imaging. SHG signals have well-defined polarizations, and thus SHG polarization anisotropy can be used to determine the absolute orientation and degree of organization of proteins in tissues [24, 25, 26, 27, 28].

The polarization dependence of SHG for collagen and myosin has been studied

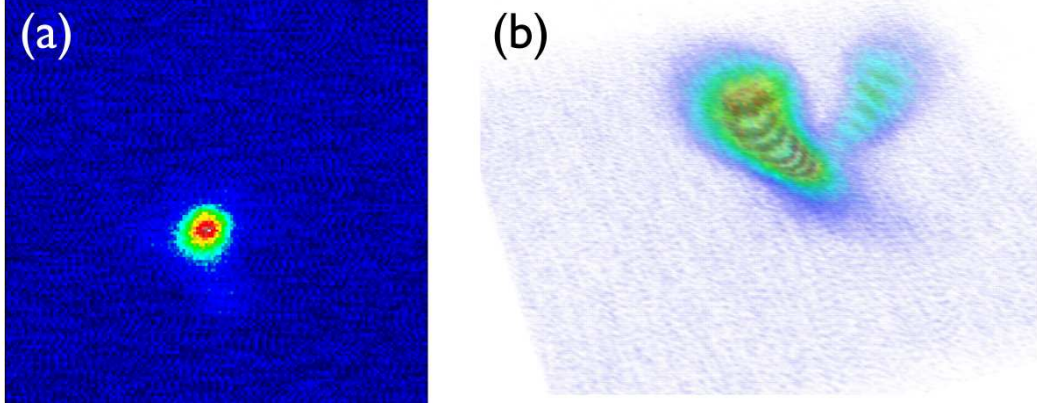


Figure 3.5: SHG scanning microscopy of starch. (a) 2-D images of a single starch granule (b) 3-D.

extensively [19, 20, 21]. Briefly, for a well aligned molecules such as fibril collagen and muscle myosin, one can approximate the susceptibility tensor to be cylindrically and C_∞ symmetric [20]. This reduces the number of independent susceptibilities elements of $\chi^{(2)}$ tensor to four elements [31, 13, 71, 20, 14]. The induced second order polarization by a focused linearly polarized laser with frequency ω in the i^{th} direction, can be written as,

$$P_i^{(2)}(2\omega)_i = \frac{1}{2}\epsilon_0 \sum_{j,k} \chi_{ijk}^{(2)} \mathbf{E}_j(\omega) \mathbf{E}_k(\omega) \quad (3.12)$$

For a z propagating y -polarized field, and assuming the filament is y -aligned, this polarization can be decomposed into two components, $P_y^{(2)}(2\omega) = \frac{1}{2}\epsilon_0 \chi_{yyy} E_y^2(\omega) + \chi_{yxx} E_x^2(\omega)$ and $P_x^{(2)}(2\omega) = \chi_{yxx} E_y(\omega) E_x(\omega)$, where $E_x(\omega)$ and $E_y(\omega)$ are the field projections in the x and y directions. This induced polarization produces SHG which can be written as,

$$I_y(\phi) = \frac{1}{2}\epsilon_0 I_{SHG} \left[\frac{\chi_{yyy}}{\chi_{yxx}} \cos(\phi)^2 + \sin^2 \phi \right]^2 \quad (3.13)$$

$$I_x(\phi) = \frac{1}{2}\epsilon_0 I_{SHG} [\sin(2\phi)]^2 \quad (3.14)$$

where ϕ is the angle of polarization with respect to the tendon, I_{SHG} is the total intensity measured with a polarizer in the y -direction. Equation (3.14) shows the polarization dependence of SHG signal in biological tissues like collagen and muscles. For instance, experimentally, the orientation of the muscle fibrils and molecular symmetries can be determined by a polarizer/halfwaveplate combination [28, 20]. Figure 3.6 show the second harmonic signal collected of human cardiac muscle measured in our lab, using a low NA condenser. The theoretical data, Eq. (3.14), has also been included for comparison purposes. As it has been reported [103], some characteristics of the curve (e.g the absolute minimum) are affected by the age of the sample and the origin of the sample. Our data here is taken from a fixed tissue purchased from Microscope Store, LLC. The discrepancies between the theoretical data and experimental data, possibly is due to the age of the sample.

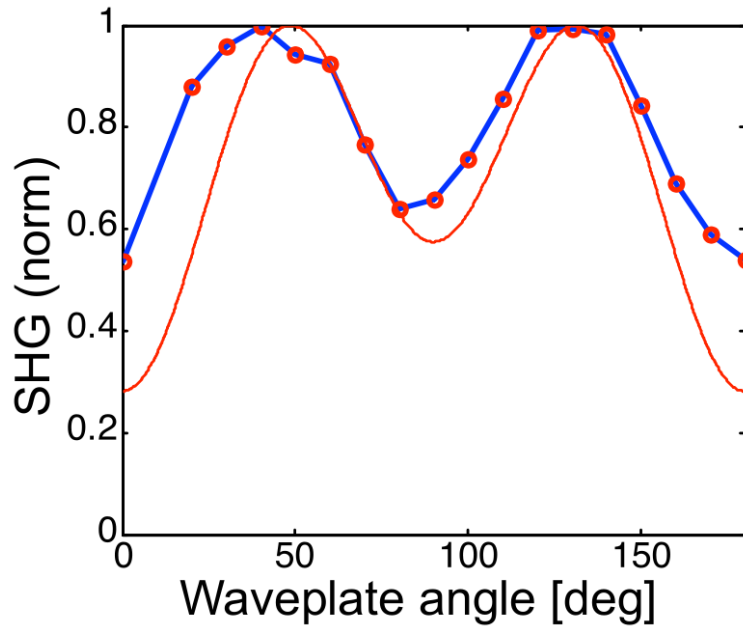


Figure 3.6: Experiment (Blue) and theoretical (Red) data of SHG of a human cardiac muscle versus polarization angle. The discrepancy is believed to be due to the age of the sample.

3.3 Third Harmonic Generation Microscopy

Third harmonic generation as a nonlinear optical microscopic contrast was introduced by Barad *et.al* [15]. Soon after that, the first THG microscopy in living biological specimens was demonstrated [16]. It was shown that THG imaging is especially suited for 3-dimensional imaging of transparent specimens. During the past decade, THG has been used to study variety of biological specimens, ranging from muscle fibers [20] to live Zebrafish embryos [29].

Contrast mechanism in THG microscopy is different than SHG microscopy. Unlike SHG, THG is present in all material no matter what symmetry it might possess. Moreover, as explained in chapter 2, under focusing conditions, e.g in microscopy, there is no or little THG generated in a homogenous material. Significant THG is only generated when the symmetry along the optical axis is broken which occurs when the incident beam is focused on an inhomogeneity or a material interface. This is the fundamental contrast mechanism in THG microscopy. The generation of TH under focusing conditions has been described in [30, 31, 15, 32, 33].

There are, however, some similarities between SHG and THG. As a nonlinear coherent process, depending on the shape of the material, the THG is forward and backward directed. Like SHG, the third harmonic is generated in the focal region giving rise to excellent sectioning capability.

Figure 3.7 show THG images of different biological sample taken using a 37 MHz train of 80 fs pulses with a center wavelength of 1550 nm Er: fiber oscillator.

As in nonlinear scanning microscopy one can construct 3-D images using SHG or THG, a fourth dimension can be added by combining the two modalities (or more) to look at structural aspect. Figure. 3.8 show multimodal (SHG, THG, white light) images of a human cornea and cell culture .

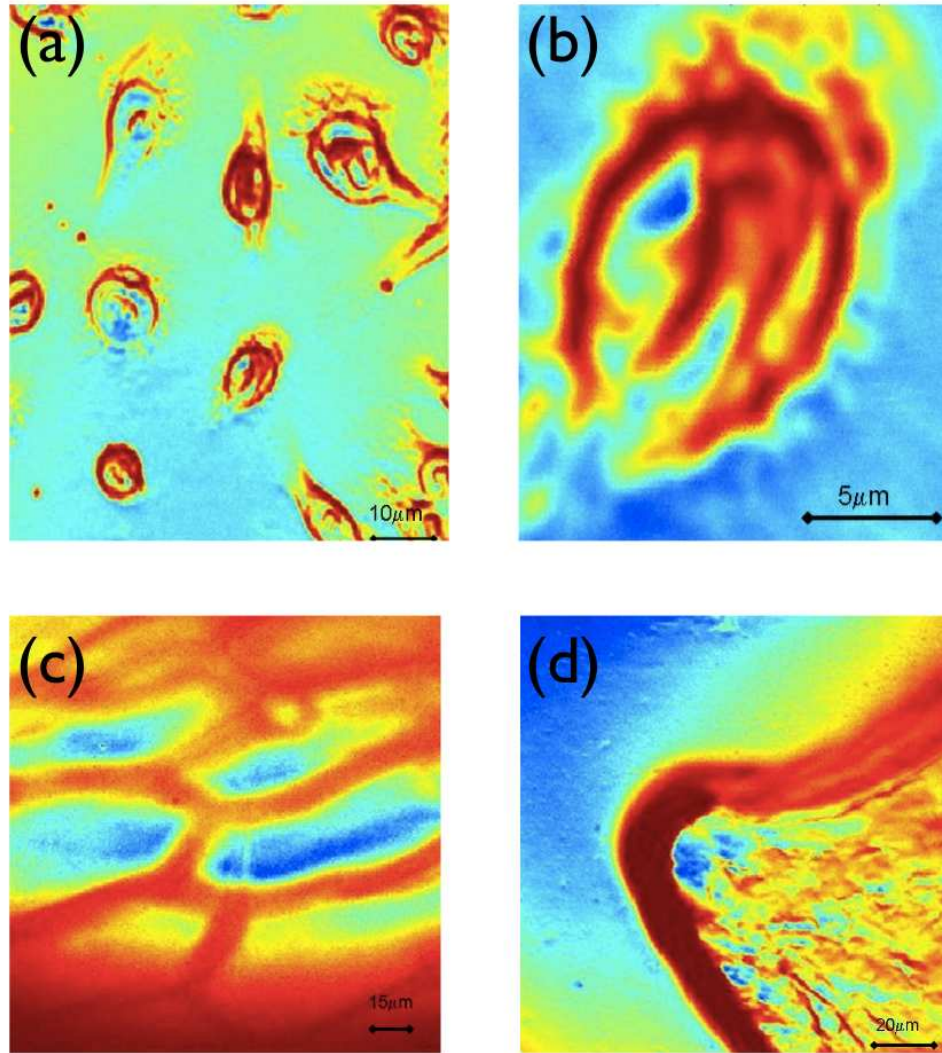


Figure 3.7: THG from Biological samples: (a) Cell culture. (b) Zoomed in. (c) Onion. (d) Cornea.

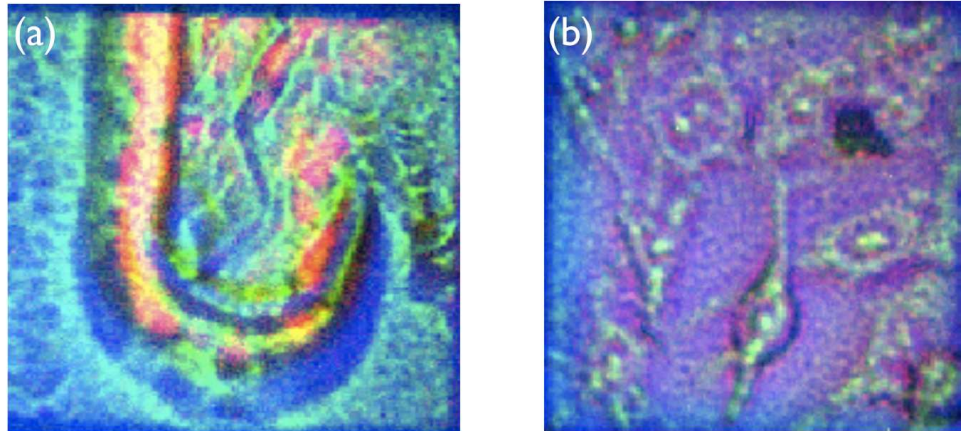


Figure 3.8: Multi-modal imaging (White light, SHG, and THG): (a) Cornea. (b) Cell culture

Chapter 4

Resolution Enhancement in Third Harmonic Microscopy through Polarization Switching

4.1 Introduction

In optical microscopy, the polarization state of the focal field strongly influences the images formed due to the impact of focal spot size [34], adjusting the relative strength and phase of both transverse and longitudinal field components, and manipulation of the interaction with the sample under study [35]. For instance, compared to spatially-uniform polarization states, more compact focal spots are possible with radially-polarized fields [34].

Full three-dimensional control over the polarization state of focal fields has been demonstrated through mode-conversion and phase control with spatial light modulators [104, 105, 106, 107, 108]. In anisotropic samples, precise manipulation of the focal field polarization state distribution can be used to probe the anisotropy of sub-wavelength particles interacting with the focal field [36].

Due to the complexity of nonlinear optical tensors, coherent nonlinear microscopies (CNM), including third harmonic generation (THG) [15, 16, 32], second harmonic generation (SHG) [64], and coherent anti-Stokes Raman scattering (CARS) [18] offer rich possibilities for new control over the imaging process. Recent numerical investigations on the implications of the focal field polarization THG microscopy have been undertaken [109, 110], while other work has explored the selectivity of specific focal field polarization components to elements of the SHG tensor in SHG microscopy [79, 111, 99, 112], and high resolution sensitivity to chemical interfaces has been demonstrated by focal field control in CARS microscopy [113].

In chapter 2 we explored some of the properties of SHG and THG. We saw that, while SHG radiation is only emitted for media lacking inversion symmetry, THG is a more universal process that occurs in all media regardless of symmetry. Furthermore, we saw that THG scattering is suppressed for a circularly-polarized field in an isotropic medium [30]. In this chapter, we exploit the sensitivity of THG scattering to the field polarization to enhance the spatial resolution in a THG nonlinear microscope.

4.1.1 Setup

We demonstrate enhanced THG microscopy resolution by imaging a controlled, spatially-inhomogeneous polarization state distribution, created with a spatial light modulator (SLM), to the focal plane of a microscope objective. The SLM (Boulder Nonlinear Systems, Lafayette, CO) has 1×12288 pixels with a $1.6 \mu\text{m}$ pixel pitch. The SLM only perturbs p -polarized light so that we can create arbitrary elliptical polarizations by mixing with an s polarization component whose phase is not perturbed by application of voltage to the SLM pixels. The linear arrangement of pixels allows us to control the spatial polarization in one dimension, leading to an intrinsic comparison between standard and enhanced resolutions in a single image by comparing the orthogonal

direction exhibiting a spatially uniform polarization state.

Our experimental setup is shown in Fig. 4.9. A 37-MHz train of ultrashort pulses with a center wavelength of 1550 nm is obtained from an Er: fiber laser system (Precision Photonics; Boulder, CO). The pulses with an average power of 120 mW, pass through 480 mm of BK7 to temporally compress the pulses at the focus of the microscope. We characterized our pulses with SHG frequency resolved optical gating (FROG) measurement, which measured a 84 fs pulses at the focus of the microscope (see Fig. 4.1).

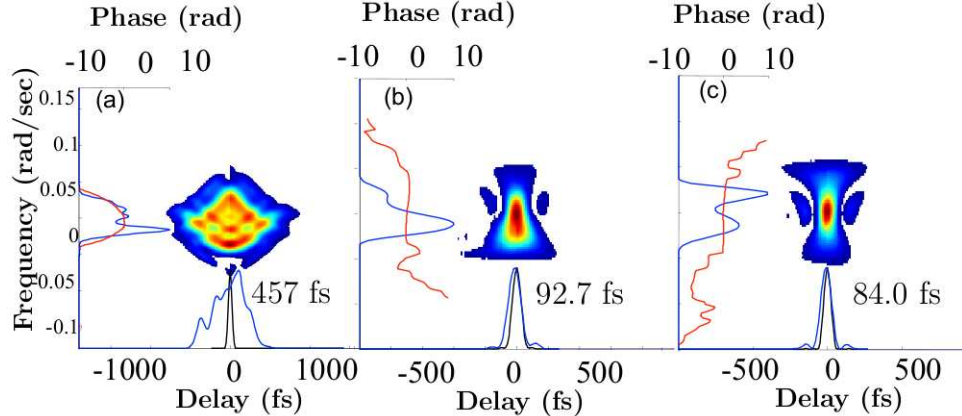


Figure 4.1: FROG traces of pulse a) before the compressor (BK7), b) before the microscope objective, c) after the microscope objective.

The pre-chirped pulses are loosely focused on the reflective SLM with a $f1 = 1000$ mm lens. The beam is recollimated after reflection from the SLM with a second lens $f2 = 500$ mm, placed one focal length before an xy -scanning galvanometer (Nutfield Technology QS-10) that is imaged to the pupil plane of a Zeiss A-Plan 40×0.65 -NA objective with a 1 : 1 telescope. The scanning galvanometers were driven by $x - y$ servo drivers, which were controlled by the analog-to-digital converter (National Instruments Corporation USB-6251). The focusing lens $f1$ was chosen to use a maximum amount of SLM pixel for shaping the beam, while the collimating lens,

f_2 was chosen to achieve a desired beam radius at the back aperture of the focusing objective.

The forward-directed THG signal is collected with a photo-multiplier tube (PMT) after passing through a 10 nm wide optical bandpass filter centered at 520 nm (Thorlabs FB520 – 10). The signal is boosted with a low-noise current pre-amplifier (SRS SR570) and recorded with the same analog-to-digital converter that controls the galvos.

A THG image of a 100 nm diameter polystyrene bead (Microspheres-Nanospheres), with a spatially-uniformly (linearly) polarized beam, is shown in Fig. 4.17(a). The image shows a FWHM microscope resolution of $2 \mu\text{m}$. The limited resolution of the microscope system is due to the under-filled back aperture of the objective.

4.1.2 Laser-scanning microscope design

There are three main parts to the design and characterization of our laser-scanning microscope, which will be outlined below: alignment of the microscope, SLM calibration and magnification characterization.

The most critical part of the design of laser-scanning microscope is the alignment of the focusing objective. In our laser scanning microscope setup, the microscope objective is tilted with use of a mirror holder and translated with a $x - y$ translation stage. The alignment steps of the objective is listed below:

- Align the beam using an alignment card. One should use the same alignment card throughout the whole alignment procedure.
- Make sure that the beam is centered at back aperture of the objective. Using the translation stage and mirror holder's knob maximize the throughput of the

beam power.

- Take the objective off and align the beam to a set target (alignment card), then screw the objective in place and using the translation stage ONLY, translate the objective until your beam hits the target.
- Place a pinhole in front of the objective (before the pupil plane), and maximize the amount of light going through the pin hole. Then using the mirror knobs ONLY make sure the back-reflected beam off the objective lens goes through the pin hole.
- Repeat this procedure until satisfied.
- Be very patient, as the alignment of the objective is the most important, while most tedious part of the scanning microscope alignment. You might need to repeat this procedure everyday as the temperature fluctuation in the lab will steer the mirrors and misalign your system.

Figure 4.2 show a THG image of a $12\ \mu\text{m}$ pitch TEM gold mesh grid before and after a good alignment procedure.

The manipulation of the spatial polarization of the beam requires locating the exact position of the beam on the SLM, finding the polarization axis of the SLM, and mapping of the applied voltage to phase.

The location of the beam on the SLM was found by writing and sweeping a sinusoidal phase grating on the SLM, while collecting the zeroth order diffraction with a photo-diode. As the phase grating is being swept across the SLM, depending on the diffracted energy, we can extract the pixels occupied by the beam. Figure 4.3 shows the beam ($1/e^2$) occupies about 550 pixels, corresponding to $340\ \mu\text{m}$.

The polarization axis of the SLM was found by writing a sinusoidal phase grating across the shaper and collecting the zeroth order diffraction, while changing half wave-plate angle L_1 before the SLM. Since, the SLM only shapes the p -polarized light, no

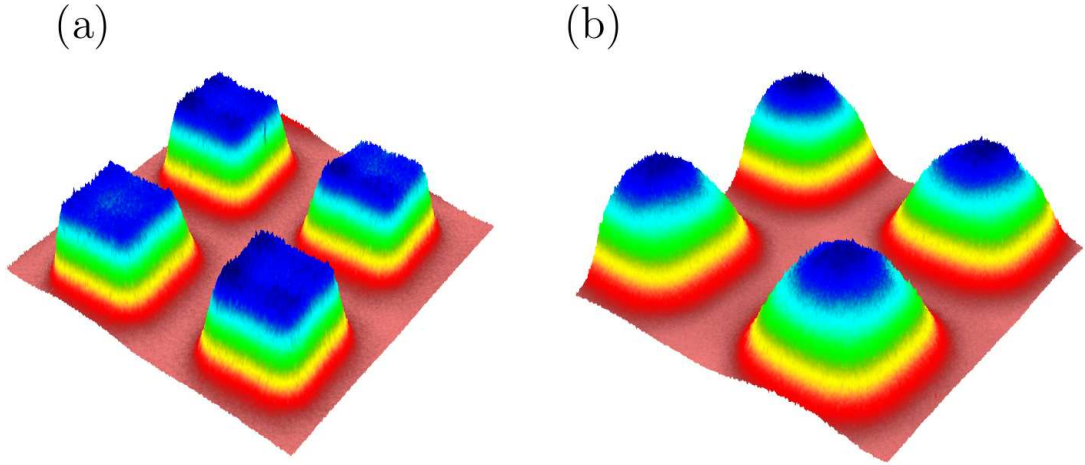


Figure 4.2: THG images of a mesh grid ($12 \mu\text{m}$ pitch), before and after objective alignment procedure mentioned in the text.

change in the diffraction pattern would be noticed when the wave-plate angle correspond to a s -polarized axis of the SLM, and maximum attenuation would be recorded by the photo-diode, when the half wave plate angle corresponds to the p -polarized axis of the SLM. Maximum and minimum half wave plate angles of 198° and 152° were recorded. Moreover, the corresponding SLM polarization axis at the pupil plane of the objective was found by maximizing the signal throughput of a polarizer $P2$ before the objective microscope. Maximum and minimum polarizer angles of 24° and 112° were recorded.

The mapping between the applied voltage on the SLM and corresponding phase shift induced by the SLM was calibrated using spectral interferometry [114, 115]. In this method, the beam goes through a calcite crystal which separates and introduces a time delay between the two polarizations. As the beam is incident on the SLM, we apply uniform voltages across the SLM which adds a constant phase to the p -polarized component of the beam. Using spectral interferometry [115] the spectral phase, corresponding to the applied phase to the SLM is, retrieved. Figure 4.4 (b)

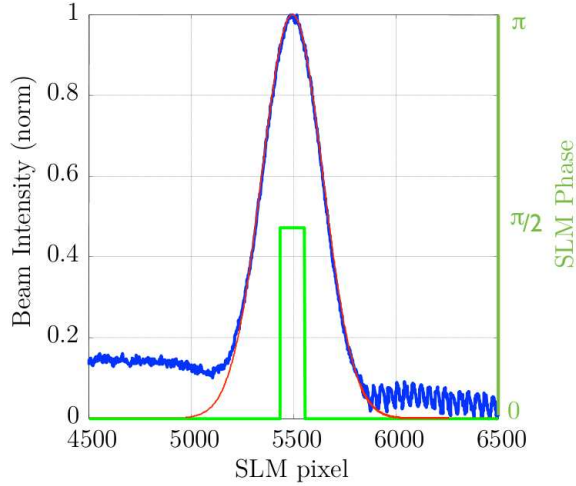


Figure 4.3: Beam profile of the beam on the SLM (Blue), Gaussian fit (Red). The green step corresponds to the $\pi/2$ phase jump written on the SLM for enhanced resolution experiment (see text).

illustrates the mapping between the applied voltage and its corresponding voltage.

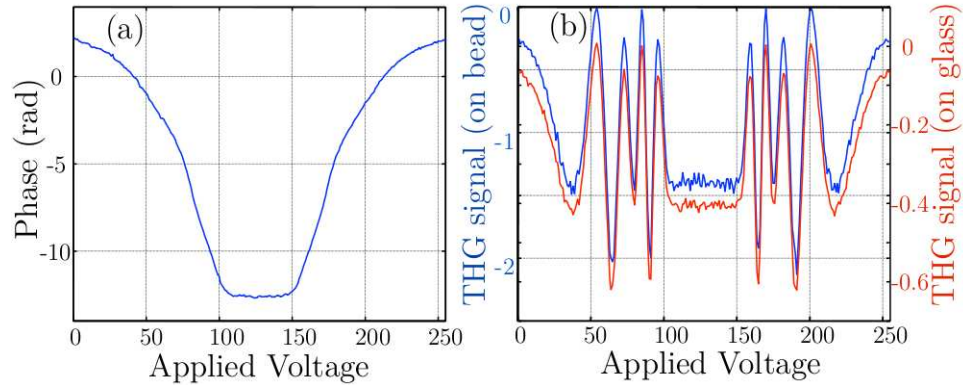


Figure 4.4: SLM characteristics: a) Calibration through spectral interferometry (see text). b) To ensure the bead under study does not affect the polarization at the focus, we apply a constant voltage across the SLM, while monitoring the THG signal. We repeat this procedure on a cover slip. Both nano-bead and the cover glass behave the same and have the same response to the polarization at the focus.

The total demagnification at the focus was measured by displacing the beam on the SLM by rotating a 6.35-mm thick window SW placed in the beam incident on the SLM. For each window rotation, a beam profile similar to Fig. 4.3, and a THG image of a bead, similar to Fig. 4.17(a) was acquired. Figure 4.5(a) show the translation of

the beam profile on the SLM, and 4.5(b) shows the bead centroids (marked with *) of the THG signal resulting from the translation. The transformation of the beam from the SLM to the focus includes both a demagnification M and a rotation ρ , since the \hat{x} axis in a scanned image does not align with the pixel axis of the SLM, which was due to the translation axis of the galvanometer. The demagnification, defined as the ratio between the net beam displacement on the image plane and the SLM, is measured to be $|M| = 130$, in good agreement with a theoretical estimate of $|M| = f_2/f_{\text{obj}} = 500/4$. The focal length of the objective is calculated by L_t/M_o , where $L_t = 160$ is the tube length of a specific objective (Zeiss in our case) and $M_o = 40X$ is the indicated microscope objective magnification. From the direction of motion in Fig. 4.5(b), the rotation angle is measured to be $\rho = -16^\circ$.

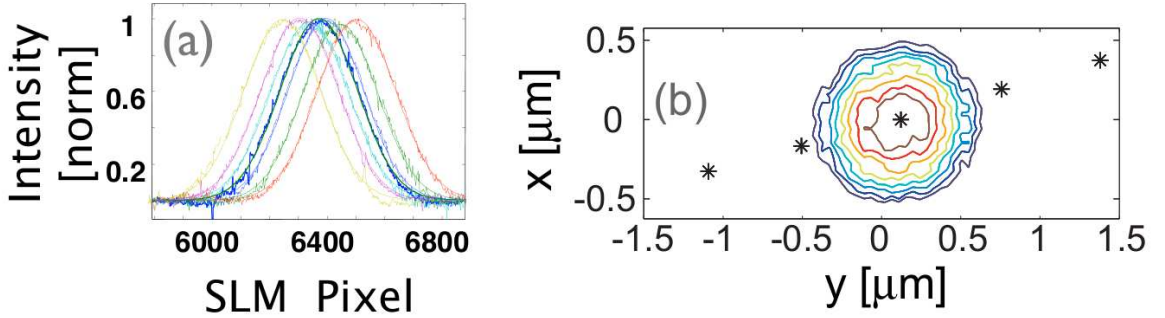


Figure 4.5: Demagnification. a) Beam displacement on the SLM, and b) beam movement at the focus of the objective.

4.2 Proposed Method for Resolution Enhancement

The process of enhanced spatial resolution is pictured schematically in Fig. 4.6. In this approach, the polarization state of the focal field is linearly-polarized at the beam center and is switched to circularly-polarized at some radius r_s . As described in more detail below, we create the desired focal field spatial distribution of the polarization by imaging an abrupt $\pi/2$ phase jump at the two edges of the focal field, created by

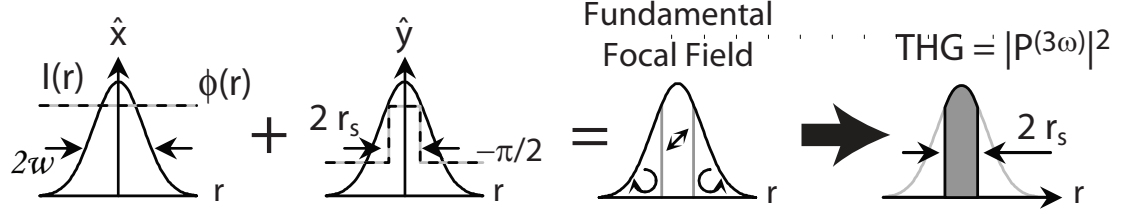


Figure 4.6: Principle of spatial resolution enhancement. The superposition of a spatially-uniform phase in the s polarization and a $\pi/2$ -rad phase jump on the p polarization switches the polarization state from linear in the center to circular at some radius r_s . This suppresses the THG signal at the edges, giving rise to enhanced resolution.

a spatial light modulator, switching the spatial polarization at some radius r_s from circular to linear and back to circular again. The limited back aperture of the microscope objective filters out high spatial frequencies of the incident field and thus smoothes the abrupt phase discontinuity. The actual spatial distribution of the polarization state is probed through a THG polarization tomography [116].

4.2.1 Spatial Polarization Shaping

We denote the spatial distribution of the field at the focus as,

$$\mathbf{E}(x_f, y_f) = E_{x0}(x_f, y_f) \{ \hat{\mathbf{x}} + R(x_f, y_f) \exp[i\delta(x_f, y_f)] \hat{\mathbf{y}} \} \quad (4.1)$$

where (x_f, y_f) are the spatial coordinates of the focal field, and $R(x_f, y_f) = \frac{E_{y0}(x_f, y_f)}{E_{x0}(x_f, y_f)}$ and $\delta(x_f, y_f) = \delta_x(x_f, y_f) - \delta_y(x_f, y_f)$ are the relative amplitude and phase, respectively, between the polarization components. A half wave plate inserted into the beam incident on the SLM is rotated to provide equal amplitude between s and p polarized light at the SLM. Application of a spatially varying phase along the y direction at the SLM images to a one-dimensional spatially-varying phase $\delta(x, y) \rightarrow \delta(y)$ at the microscope focus. Together, $R(x, y)$ and $\delta(x, y)$ dictate the spatial variation of the polarization state of the focal field spatial distribution.

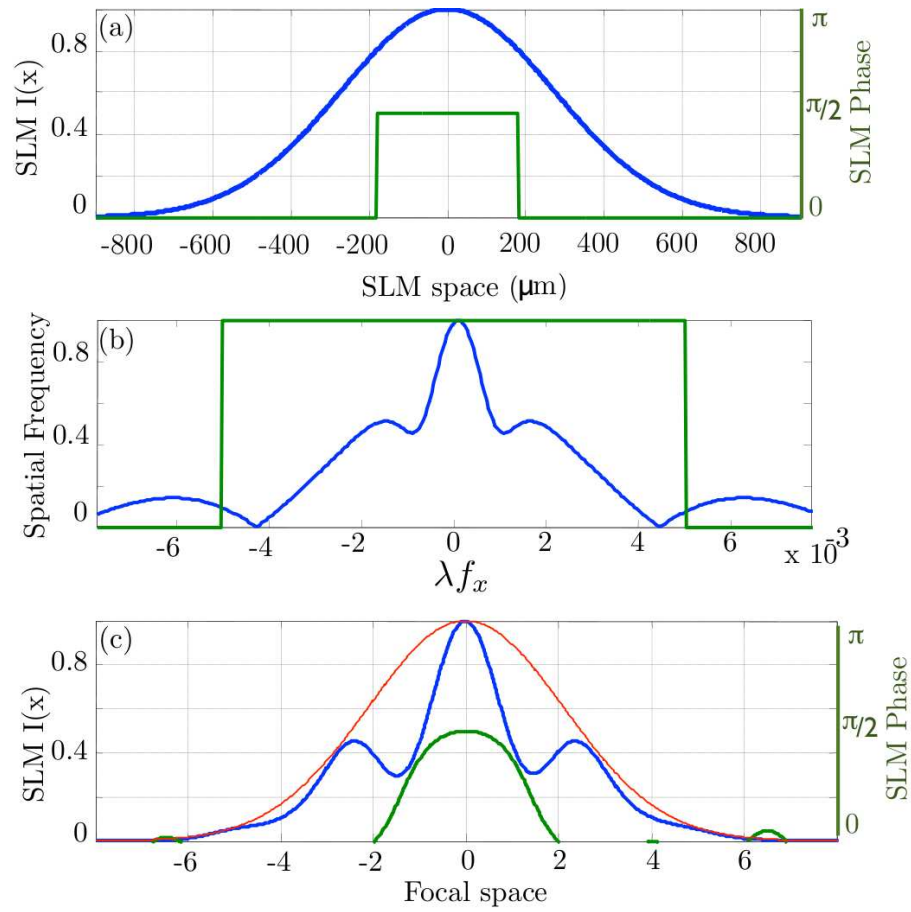


Figure 4.7: Simulation of spatial filtering caused by low numerical aperture of the collecting lens. a) Beam profile and the applied $\pi/2$ phase jump on the SLM. b) Spatial filtering of the spatial frequency. The numerical aperture of the collecting lens, filters high spatial frequency content due to the abrupt phase jump and c) smooths the abrupt phase discontinuity.

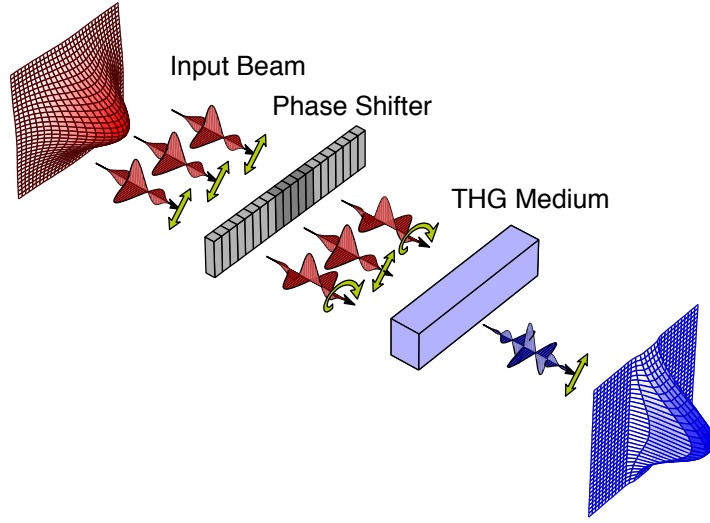


Figure 4.8: The SLM shapes an spatially uniform linear polarized beam so that the edges of the beam are circularly polarized while the center of the beam is kept linear. The THG signal from the medium is suppressed at regions of the beam that is circularly polarized, while significant THG signal is observed at the center of the beam where the polarization is kept linear.

The THG polarization density for an isotropic medium is given by $\mathbf{P}^{(3)} = \frac{1}{4}\epsilon_0\chi_{1111}^{(3)}(\mathbf{E}\cdot\mathbf{E})\mathbf{E}$. The polarization density is thus zero for a circularly-polarized field and reduces the spatial region of THG scattering as sketched in Fig. 4.8. To enhance resolution, a top-hat $\pi/2$ rad phase jump profile was applied to the p polarization at the SLM, switching the spatial polarization at some radius r_s as shown in Fig. 4.6. The corresponding applied voltage that would give a linear polarized light (maximum THG signal), versus circular polarized light (minimum THG signal) was extracted from data shown in Fig. 4.4. Furthermore, by adjusting the ration between the p and s -polarized light, using half wave plate $L2$, fully quenched THG signal was obtained. Also, the value of r_s was extracted from the beam profile shown in Fig. 4.3.

The resulting nano-bead image is shown in Fig. 4.17(b). The image shows a resolution of $1\mu\text{m}$ corresponding an enhancement of $\sim 2\times$ in the SLM axis direction (vertical) as compared to the unshaped image.

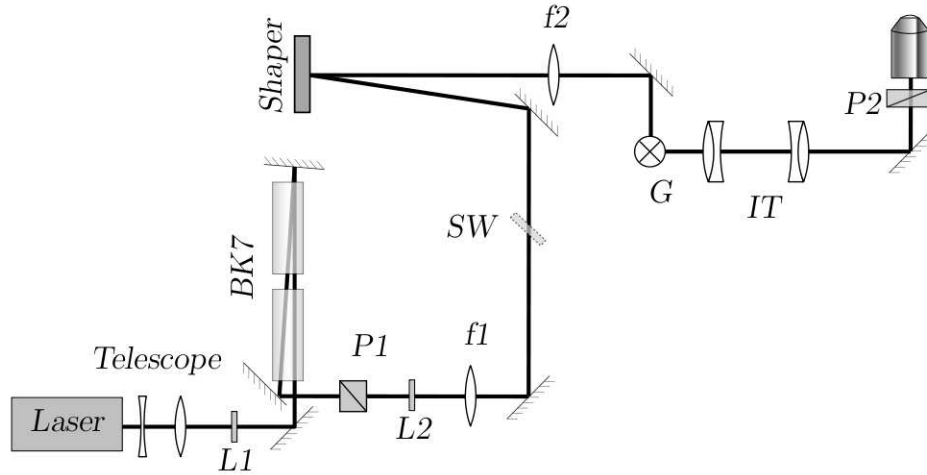


Figure 4.9: Experimental setup: The laser beam driven from the 1550 nm fiber oscillator is collimated and expanded, and compressed by double passing two blocks of BK7 material. The elliptical polarized beam is then polarized ($P1$) and its polarization is rotated by its a half waveplate ($L2$). The beam is focused on the SLM and re-collimated with $f1$ and $f2$ resp. A scanning galvanometer is imaged on the back aperture of the objective by a 1 : 1 imaging telescope. Polarizer $P2$ is used for the polarization tomography experiment, and a window plate SW scans the beam across the SLM for demagnification characterization.

An essential test of the nanobead probe is that it exhibits an isotropic response so that the polarization state can be unambiguously probed. Even with multiple ultrasonicated dilution steps, many regions of microsphere sample deposition do not exhibit isotropic optical properties. We found that a mixture of 0.1 mg of polystyrene bead mixture (a single droplet) to 1 cup of water gives a good probability of finding an isolated nanobead. It is a good practice to make a few samples at a time, since the preparation of the sample requires the dilution dry out. To prepare our samples, we made a dilution according to above. The dilution then was put on a ultrasonic device. A droplet of the dilution was laid on a glass slide and was immediately covered by a cover slip. The glass slide was put on a hot plate for fast evaporation of the water. The faster the water evaporate, the less chance of cluster build up. Too much heat, however, will deform the sample.

To verify that the response is isotropic, the direction of a spatially homogeneous, linearly polarized focal field is scanned through a full 2π angle with rotation of a half wave plate inserted at the back aperture of the objective. An isotropic response requires the THG scattering strength to be independent of the direction of the linearly polarized field. Further validation of the isotropic response is obtained by testing THG scattering suppression with a circularly polarized field. In tests with a circularly polarized field, THG scattering collected from the nanobeads are reduced by a factor of 100-to-500. These results are presented in Fig.4.10.

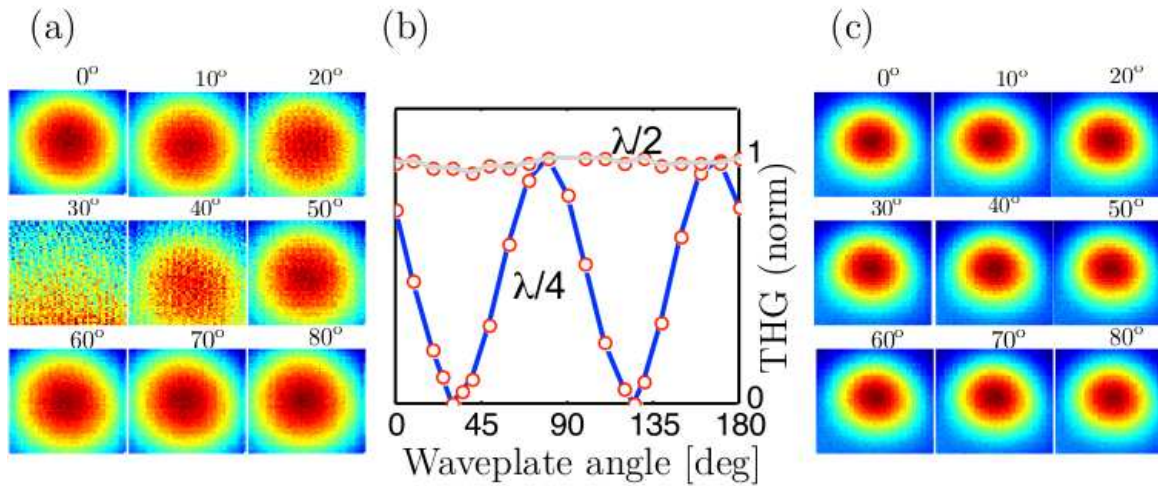


Figure 4.10: Isotropic response: The THG signal from an isotropic bead with linearly polarized focal field: THG signal is a) suppressed with a circularly polarized field. c) independent of the direction of the linearly polarized field.

4.3 THG Polarization Tomography of the Fundamental Field

In section 4.2 we exploited the polarization dependence of THG to enhance the spatial resolution in scanning THG microscopy, by applying a circular polarized light at the edges of the laser beam while having linear polarization in the middle of the beam

[35]. In this section, we demonstrate spatial control and measurement of spatially inhomogeneous polarization state focal fields for THG microscopy at the focus of an objective. By locally probing the polarization state of the focal field through THG emission in a laser-scanning THG microscope, we map out the polarization state that generates THG radiation at the focal field. We demonstrate spatial modulation of the polarization state in the focal plane.

To characterize the spatial polarization distribution of the focal field, we probed the local polarization state in the focal field by profiling the THG scattering from the focal field with the polystyrene nanobead (Corpuscular, Plain C-PS-0.10), with a diameter $d = 100 \text{ nm}$ much less than the wavelength, $d \ll \lambda$. The small diameter of the nanobead samples only a small spatially localized region of the focused fundamental beam. A polarizer in the pupil plane, which can be set to an angle of η with respect to a reference direction $\hat{\mathbf{x}}$, permits selection of a specific polarization projection component direction in the focal plane provided that the microscope objective $\text{NA} < 0.7$. Recording THG images under various linear polarization projections of the incident field, the inhomogeneous focal polarization state distribution can be determined noniteratively through THG microscopy polarization tomography [116].

Before we develop the phase retrieval algorithm using THG signal, it would be instructive to illustrate the method of phase retrieval using intensity measurement of the fundamental electric field. This is shown in Fig. 4.11. Figure 4.11(a) illustrates how the spatial features of an arbitrary polarized electrical field can be represented as a vectorial sum of its x -polarized component and y -polarized component, along with the phase difference between the two fields. Bearing this in mind, we ask ourself, how can we retrieve the full spatial features of an electrical field, provided information about its intensity is know. In another words, provided we can record the intensity profile of an electric field, for example using an square law detector, how can we re-

construct the electric field (since the phase information will be lost upon recording of the intensity). Figure 4.11(b) illustrates a possible solution. In order to reconstruct the field three pieces of information is needed, namely $\mathbf{E}_x(x, y)$, $\mathbf{E}_y(x, y)$, and the phase difference $\delta(x, y)$ between the two. The first two quantities, \mathbf{E}_x and \mathbf{E}_y can be retrieved by recording the intensity of the field while inserting an polarizer before the detector at angles $\eta = 0^\circ$ and $\eta = 90^\circ$ respectively. In order to find the last piece of information $\delta(x, y)$, we record the intensity profile while dialing the polarizer angle at $\eta \neq 0^\circ, 90^\circ$, say $\eta = 45^\circ$. Using these three measurement, one can calculate the absolute value of the phase $|\delta(x, y)|$, and therefore the complete spatial polarization of the field (there will, however, be a sign ambiguity on the phase).

In next section we will use a similar method to retrieve the spatial phase of a fundamental electric field at the focus of an objective, by collecting the far-field THG signal from a polystyrene microsphere.

4.3.1 Spatial Polarization Phase Retrieval

To probe the spatial polarization state profile of the focused fundamental field, we prepare a sample of a polystyrene beads whose diameters are small compared to the diameter of the focal spot, and place it in the laser-scanning THG microscope shown in Fig. 4.9. The diameter of the microsphere is sufficiently small to sample only a small spatially-localized region of the focused fundamental beam. In this limit, the third harmonic polarization density is evaluated at the center of the nanosphere located at x_f, y_f , and is given by $\mathbf{P}^{(3)}(x_f, y_f) = \frac{1}{4}\epsilon_0\chi^{(3)}E^2(x_f, y_f)\mathbf{E}(x_f, y_f)$. Here the x, y, z vector components of the focal field are $\mathbf{E} = (E_x, E_y, E_z)$ so that the factor $E^2 = \mathbf{E} \cdot \mathbf{E} = E_x^2 + E_y^2 + E_z^2$. The vector focal field is related to the incident field through the the Richards–Wolf integral [117].

The far-field THG intensity signal generated by the microsphere is filtered by

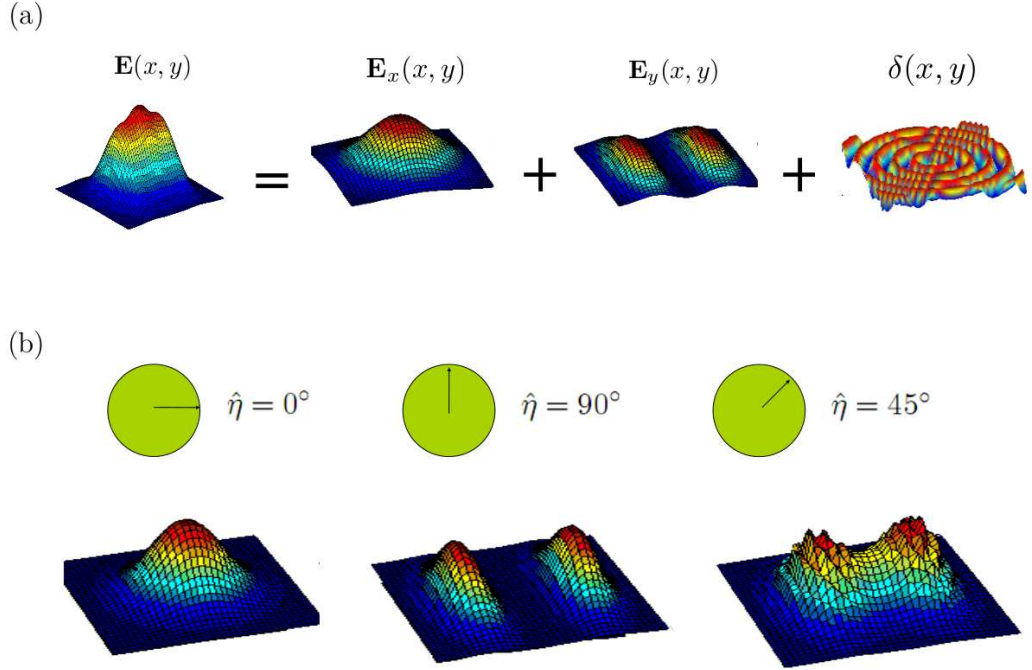


Figure 4.11: Spatial electric field retrieval. a) An electric field can be decomposed in terms of its x and y -polarization, while the phase difference between the two are needed to completely characterized the field. b) There intensity measurement with a polarizer at angles $\eta = 0^\circ$ and $\eta = 90^\circ$ and $\eta \neq 0^\circ, 90^\circ$, say $\eta = 45^\circ$ are needed to fully recover the spatial features of an electric field.

a bandpass chromatic filter, and collected by a photo-multiplier tube (PMT). Figure 4.12 show the third order power dependence of the signal, with slope of ≈ 2.8 . The integrated signal S at the detector is given by,

$$S = \int_{\Theta_{min}}^{\Theta_{max}} \int_0^{2\pi} |\mathbf{E}_{THG}(x_f, y_f)\delta(x_f, y_f)|^2 d\Omega \quad (4.2)$$

proportional to a sum over the third-harmonic polarization density vector components. Here, Θ is the acceptance angle of the focusing objective, Ω is the solid angle.

The far field THG signal generated by an object $\mathcal{O}(\mathbf{r})$ can be represented by Dyadic Green's function integral [78, 81] given by,

$$\mathbf{E}_{THG} = -\mu_0\omega_3^2 \frac{\exp[ik_3R]}{R} \int_V \mathcal{O}(\mathbf{r}) \exp\left(\frac{-ik_3\mathbf{R} \cdot \mathbf{r}}{R}\right) \mathbf{M} \cdot \mathbf{P}^{(3)} d\mathbf{r}^3 \quad (4.3)$$

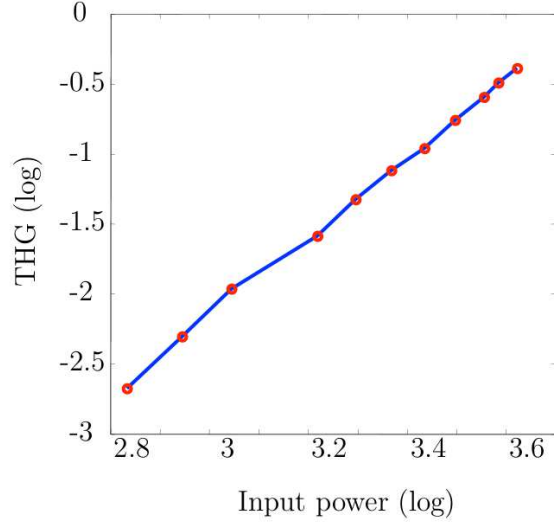


Figure 4.12: Third order power dependence of the signal. the slope is measured to be 2.8

where in spherical coordinate (unit vectors ordered $[\hat{R}, \hat{\Theta}, \hat{\Phi}]$), M is given by,

$$M = \begin{pmatrix} 0 & 0 & 0 \\ \cos \Theta \cos \Phi & \cos \Theta \sin \Phi & -\sin \Theta \\ -\sin \Phi & \cos \Phi & 0 \end{pmatrix} \quad (4.4)$$

For a small nanobead, however, the object can be considered as a delta function $\mathcal{O}(\mathbf{r}) = \delta(\mathbf{r})$. Substituting this into Eq. 4.3, we find,

$$\mathbf{E}_{THG} \approx -\mu_0 \omega_3^2 \frac{\exp[ik_3 R]}{R} \begin{pmatrix} 0 \\ \cos \Theta \cos \Phi P_x^{(3)} - \sin \Theta P_z^{(3)} + \cos \Theta \sin \Phi P_y^{(3)} \\ \cos \Phi P_y^{(3)} - \sin \Phi P_x^{(3)} \end{pmatrix} \quad (4.5)$$

To find the the integrated signal at the detector, we evaluate Eq. (4.2), for $\Theta_{min} = 0$ and $\Theta_{max} = \pi/2$, and we find,

$$S = \pi^2 [3|P_x^{(3)}|^2 + 3|P_y^{(3)}|^2 + 3|P_z^{(3)}|^2] / 4 \quad (4.6)$$

$$\propto |E^2|^2 [3|E_x|^2 + 3|E_y|^2 + 2|E_z|^2] / 4 \quad (4.7)$$

where $E^2 = \mathbf{E} \cdot \mathbf{E} = E_x^2 + E_y^2 + E_z^2$. In Eq. (4.8), $P_x^{(3)}, P_y^{(3)}, P_z^{(3)}$ is the induced polarization at the focus, by E_x, E_y, E_z respectively. In general, linearly polarized light, say E_x^{inc} incident on the focusing optics, induces a third order polarization density in the focal volume in all polarization directions ($P_x^{(3)}, P_y^{(3)}, P_z^{(3)}$), due to scrambling of the incident polarization state. However, for low numerical aperture (moderate focusing conditions) this scrambling is negligible. Figures 4.13 and 4.14 illustrate this point. In Fig.4.13 maximum values of three components of the field going in the vicinity of the focus, for a low and high numerical apertures and a x -polarized incident field, are shown. As illustrated, for both high and low numerical apertures (figure. 4.13(a) and (b)), an x -polarized incident field will have all three x, y , and z -polarization component present at the focus. However, for a low numerical aperture the magnitudes of the y and z -polarized field are considerably lower. Figure 4.14 shows the ratio of the maximum values of the focal field amplitudes $\frac{|E_{zmax}|}{|E_{xmax}|}$, and $\frac{|E_{ymax}|}{|E_{xmax}|}$ for a low, moderate, and high numerical aperture. It can be seen that for a moderate $NA = 0.6$ value, the z -polarized component of the field is almost an order of magnitude less than the x -polarized component and the y -polarized component of the field is 2 orders of magnitude smaller than the x -polarized component. This concludes that in Eq. (4.8), the integrated THG signal for an incident x -polarized field can be approximated as,

$$S = \pi^2 [3|P_x^{(3)}|^2] / 4$$

$$\propto |E_x|^6 \quad (4.8)$$

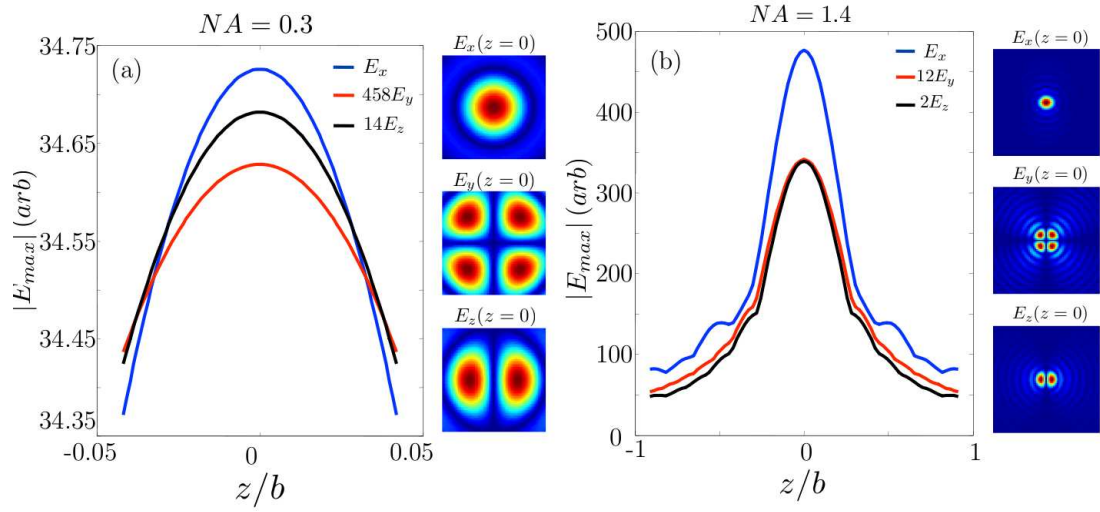


Figure 4.13: Maximum values of three components of the field going in the vicinity of the focus, for a) low and b) high numerical apertures.

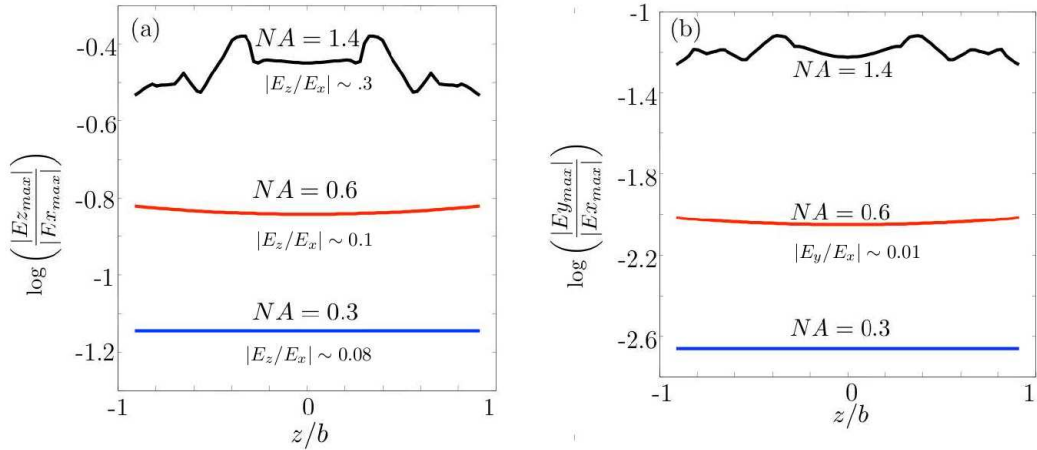


Figure 4.14: Ratio of the maximum values of the focal field amplitudes a) $\frac{|E_{z_{max}}|}{|E_{x_{max}}|}$, and b) $\frac{|E_{y_{max}}|}{|E_{x_{max}}|}$ for a low, moderate, and high numerical aperture.

4.3.2 Theory

Let us assume that the spatially varying complex amplitude $\mathbf{A}^{inc}(x_{inc}, y_{inc})$ of the electric field $\mathbf{E}^{inc}(x_{inc}, y_{inc}, z, t) = \frac{1}{2} \Re \{ \mathbf{A}^{inc}(x_{inc}, y_{inc}) e^{i(kz - \omega t)} + c.c \}$ incident at the objective can be written as,

$$\mathbf{A}^{inc}(x_{inc}, y_{inc}) = \{ \hat{\mathbf{x}} A_x^{inc}(x_{inc}, y_{inc}) e^{i\delta_x(x_{inc}, y_{inc})} + \hat{\mathbf{y}} A_y^{inc}(x_{inc}, y_{inc}) e^{i\delta_y(x_{inc}, y_{inc})} \} \quad (4.9)$$

where $\delta_x(x_{inc}, y_{inc})$ and $\delta_y(x_{inc}, y_{inc})$ are the spatially varying phase of $\hat{\mathbf{x}}$ and $\hat{\mathbf{y}}$ -polarization components, and $A_x^{inc}(x_{inc}, y_{inc})$ and $A_y^{inc}(x_{inc}, y_{inc})$ are the spatially varying amplitudes of the $\hat{\mathbf{x}}$ and $\hat{\mathbf{y}}$ -polarization components. Defining $\delta(x_{inc}, y_{inc}) = \delta_y(x_{inc}, y_{inc}) - \delta_x(x_{inc}, y_{inc})$ the relative phase, and $r(x_{inc}, y_{inc}) = \frac{A_y^{inc}(x_{inc}, y_{inc})}{A_x^{inc}(x_{inc}, y_{inc})}$ simplifies Eq. (4.9) to,

$$\mathbf{A}^{inc}(x_{inc}, y_{inc}) = \{ \hat{\mathbf{x}} + \hat{\mathbf{y}} r(x_{inc}, y_{inc}) e^{i\delta(x_{inc}, y_{inc})} \} A_x^{inc}(x_{inc}, y_{inc}) e^{i\delta_x(x_{inc}, y_{inc})} \quad (4.10)$$

After the field enters the polarizer located right before the objective, the projection of the field along $\hat{\boldsymbol{\eta}}$ with respect to $\hat{\mathbf{x}}$ is denoted by $\mathbf{A}_{\hat{\boldsymbol{\eta}}}^{inc} = \hat{\boldsymbol{\eta}} \{ \hat{\boldsymbol{\eta}} \cdot \mathbf{A}_{inc} \} = \hat{\boldsymbol{\eta}} A_{\hat{\boldsymbol{\eta}}}^{inc}$. Then,

$$\mathbf{A}_{\hat{\boldsymbol{\eta}}}^{inc}(x, y) = \hat{\boldsymbol{\eta}} \left\{ A_x^{inc}(x_{inc}, y_{inc}) \cos(\eta) + r(x_{inc}, y_{inc}) A_x^{inc}(x_{inc}, y_{inc}) \sin(\eta) e^{i\delta(x_{inc}, y_{inc})} \right\} e^{i\delta_x(x_{inc}, y_{inc})} \quad (4.11)$$

In general the vector focal field is related to the incident field through the the Richards–Wolf integral [117]. However, as show in section. 4.3.1, for a low to moderate NA ($\text{NA} \leq 0.7$), the polarization of the fundamental focal field is approximately identical to the paraxial input polarization. With this assumption, we can make the transformation of $A_x^{inc}(x_{inc}, y_{inc}) \xrightarrow{Obj} A_x^f(x_f, y_f)$ and $A_y^{inc}(x_{inc}, y_{inc}) \xrightarrow{Obj} A_y^f(x_f, y_f)$. Then, the field at the focus of the objective can be written as $\mathbf{A}_{\hat{\boldsymbol{\eta}}}^f = \boldsymbol{\eta} A_{\hat{\boldsymbol{\eta}}}^f$, with

$$A_{\hat{\boldsymbol{\eta}}}^f(x_f, y_f) = \{ A_x^f(x_f, y_f) \cos(\eta) + r_f(x_f, y_f) A_x^f(x_f, y_f) \sin(\eta) e^{i\delta(x_f, y_f)} \} e^{i\delta_x(x_f, y_f)} \quad (4.12)$$

where $A_x^f(x_f, y_f)$ and $A_y^f(x_f, y_f)$ are the spatially varying amplitude functions of the $\hat{\mathbf{x}}$ and $\hat{\mathbf{y}}$ -polarization components, $\delta(x_f, y_f) = \delta_y(x_f, y_f) - \delta_x(x_f, y_f)$ is the relative phase, and $r_f(x_f, y_f) = \frac{A_y^f(x_f, y_f)}{A_x^f(x_f, y_f)}$ is the relative amplitude at the focus of the objective.

As the focus field is being scanned across a small nano-bead whose diameter d is much less than the wavelength, $d \ll \lambda$, the local third harmonic polarization density $\mathbf{P}^{(3)}(\eta, x_f, y_f)$ generated at each x_f, y_f point can be written as $\mathbf{P}^{(3)}(\eta, x_f, y_f) = \frac{1}{4}\epsilon_0\chi_{1111}^{(3)} [\mathbf{A}_\eta^f(x_f, y_f) \cdot \mathbf{A}_\eta^f(x_f, y_f)] \mathbf{A}_\eta^f(x_f, y_f)$. The integrated far field third harmonic field can be found through Eq. 4.2 to be proportional to,

$$S(\eta; x_f, y_f) \propto |A_\eta^f(x_f, y_f)|^6 \quad (4.13)$$

Equation 4.13 tells us, the recorded THG signal by the PMT, emitted from each local x_f, y_f point at the focal spot, for each polarization angle η , is the sixth power of the absolute value of the complex amplitude $A_\eta^f(x_f, y_f)$.

Bearing in mind that the goal here, is to retrieve the fundamental field at the focus,

$$\mathbf{A}_f(x_f, y_f) = \{ \hat{\mathbf{x}}A_x^f(x_f, y_f) + \hat{\mathbf{y}}r_f(x_f, y_f)A_x^f(x_f, y_f)e^{i\delta(x_f, y_f)} \} e^{i\delta_x(x_f, y_f)} \quad (4.14)$$

there are three independent unknown functions to be found, namely, $A_x^f(x_f, y_f)$, $r_f(x_f, y_f)$, and $\delta(x_f, y_f)$. However, through Eq. (4.13) and Eq. (4.12), and three independent polarization measurements $\eta = 0^\circ, 90^\circ$ and an arbitrary third angle $\eta \neq 0, 90^\circ$ we can noniteratively find these quantities.

When the polarization angel $\eta = 0^\circ$, the collected third harmonic signal with the PMT will be, $S(0, x_f, y_f) = \{A_x^f(x_f, y_f)\}^6$. Taking the sixth root of the collected THG

signal $S(0, x_f, y_f)$, then, will give us $A_x^f(x_f, y_f)$, which is the $\hat{\mathbf{x}}$ -polarized component of the focal field. In the same manner, the collection of the THG signal for $\eta = 90^\circ$, $S(90, x_f, y_f)$ will reveal the $\hat{\mathbf{y}}$ -polarized component of the focal field, and the relative amplitude $r_f(x_f, y_f)$ can be found to be,

$$r(x_f, y_f) \equiv |A_x^f(x_f, y_f)|/|A_y^f(x_f, y_f)| = \sqrt[6]{S_Y(x_f, y_f)/S_X(x_f, y_f)} \quad (4.15)$$

In order to find the relative phase $\delta(x_f, y_f)$, we have to compute the recorded THG signal Eq. (4.13). After some algebra, and using Mathematica we find,

$$\begin{aligned} S(\eta) = |A_x^f(x_f, y_f)|^6 & \left\{ \frac{1}{2} [(\cos(\eta) \sin(\eta)r)^3] \cos(3\delta) \right. \\ & + \frac{3}{2} [\cos(\eta)^2 \sin(\eta)^4 r^4 + \cos(\eta)^4 \sin(\eta)^2 r^2] \cos(2\delta) \\ & + \frac{1}{2} [(3 \cos(\eta) \sin(\eta)r)^3 + 3 \cos(\eta)^5 \sin(\eta)r + 3 \sin(\eta)^5 \cos(\eta)r^5] \cos(\delta) \\ & \left. + \cos(\eta)^6 + r^6 \sin(\eta) + 9 [\cos(\eta)^4 \sin(\eta)^2 r^4 + \cos(\eta)^2 \sin(\eta)^4 r^4] \right\} \end{aligned} \quad (4.16)$$

Solving for $\delta(x_f, y_f)$, we find three solutions,

$$\cos(\delta) = \begin{cases} \frac{(-1+2a^2-r^2+(-1+r^2)\cos(2\eta))\csc(2\eta)}{2r} \\ \frac{(-1+r^2)\cot(2\eta)-(1+(1+i\sqrt{3})a^2+r^2)\csc(2\eta)}{2r} \\ \frac{(-1+i(i+\sqrt{3})a^2-r^2+(-1+r^2)\cos(2\eta))\csc(2\eta)}{2r} \end{cases} \quad (4.17)$$

where $a(x_f, y_f) \equiv \sqrt[6]{S_\eta(x_f, y_f)/S_X(x_f, y_f)}$. Out of the three solutions found in Eq. 4.17, only one is found to be real, that is,

$$\cos(\delta) = \frac{-1 + 2a^2 - r^2 + (-1 + r^2) \cos 2\eta}{2r} \csc 2\eta \quad (4.18)$$

Thus, the polarization state is determined non-iteratively via three scanned THG

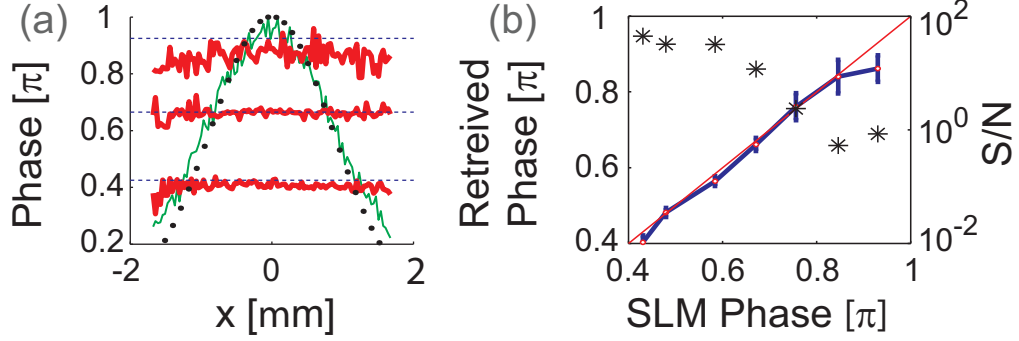


Figure 4.15: (a) Spatially uniform phase across the p -polarized field component of the laser beam. Dashed black lines correspond to the phase written on the SLM while the red lines are the retrieved phase. The green line represent the measured line-out of the third harmonic image of the bead and the black dotted line represents the line-out of the beam on the SLM, demagnified by the demagnification factor. (b) Retrieved vs. applied phase and corresponding signal to noise ratio (S/N), *.

images, measured with different orientations of the analyzing polarizer in the pupil plane. We validated numerically, that Eq. (4.18) gives a correct answer.

4.3.3 Analysis of experimental results

Figure 4.15 shows phases retrieved for uniform phase shifts of the p -polarization, i.e., uniform polarization states $\mathbf{E}(x_f, y_f)$ across the beam. Three representative phase retrievals, with $\delta_{\text{SLM}} = 0.42\pi, 0.68\pi, 0.92\pi$, are shown in Fig. 4.15(a), where we have also plotted $S(x_f, y_f)$, the retrieved bead image cross-section (thin line), compared to the demagnified beam profile measured on the SLM (black dots). The retrieved phases are shown in Fig. 4.15(b) over $\delta_{\text{SLM}} = 0.4\pi - 0.9\pi$. We estimate the error in the retrieved phase to be $\pm\pi/30$ for the relative phases of less than 0.8π . The error increases as the phase approaches more linear polarized beam. We attribute the loss of fidelity to the lower signal levels, and thus decreased signal to noise (S/N) ratio, in the source image, also shown in Fig. 4.15(b). For the data in Fig. 4.15, the polarization projection angle η was taken orthogonal to the linear polarization at δ_{SLM} , resulting in lower intensity THG images. We emphasize that linear polarizations yield

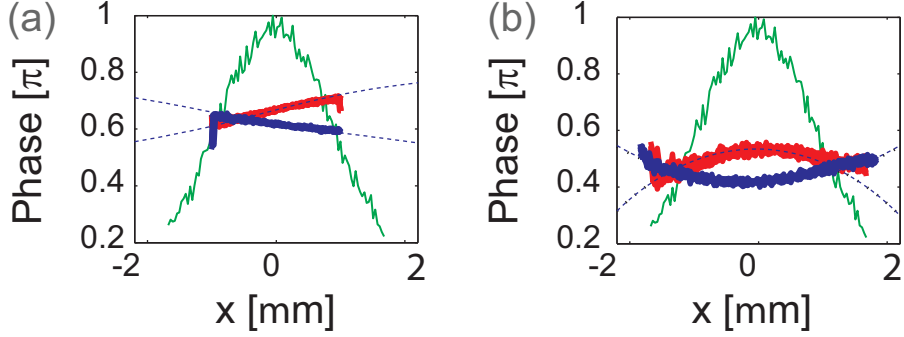


Figure 4.16: (a) Ramp and quadratic phase: Applied (dashed) and retrieved (thick) phase, along with a line-out of the third harmonic image of the bead (thin). The line-outs are taken parallel to the imaged SLM axis.

phase retrievals with the same fidelity as that for circular polarization by measuring projections at suitable angles η , more parallel to the major axis of the polarization ellipse. For polarization states up to $\delta_{\text{SLM}} \leq 0.8\pi$, the retrieved phase is in excellent agreement with the phase imposed by the SLM, and a linear regression fit yields a correlation parameter of $R^2 = 0.96$, confirming a good agreement between the applied and retrieved phase.

Spatially-varying polarization states are shown in Fig. 4.16. Since the linear SLM shapes only along one axis, we show a line-out parallel to the SLM axis transformed to the focus. To compare the retrieved and programmed relative phases, we numerically propagate the pixelated phase and beam profile on the SLM through the optical system. Diffraction from the pixelated SLM phase and spatial frequency filtering from the finite NA of the optics in the system is accounted for by the numerical propagation. The reference phase obtained with this approach is shown as this solid thin lines in Fig. 4.16. In Fig. 4.16(a), we show two polarization states that vary linearly with the x coordinate. The slopes are $d\delta/dx = \{+60, -40\}$ mrad/ μm . Over the spatial extent of the beam, our algorithm accurately retrieves both the absolute value of δ , as well as its slope. Figure 4.16(b) shows results for two polarization states with a quadratic spatial dependence, where $d^2\delta/dx^2 = \{+25, -46\}$ mrad/ μm^2 . In Fig. 4.16(b), we find that the curvature of the quadratic phase applied to the p -

polarization is accurately retrieved.

The applied and retrieved phase profiles for enhanced resolution experiment are shown in Fig. 4.18(a,b), respectively. At edges of the beam, the phase difference is measured to be $\delta = \pi/2$, while at the center of the beam the relative phase is 0.9π . Measurements of the spatial mode of the p and s components independently at the focal plane of the microscope yield images indistinguishable from that shown in Fig. 4.17(a). Thus, the relative field strength across the focal plane is maintained at unity, i.e., $R(x, y) \approx 1$, and the $\delta = \pi/2$ phase difference measured at the focal spot edges corresponds to circularly polarized light whereas the relative phase of 0.9π at the beam center reveals the beam is nearly linear, but still retains a slight ellipticity.

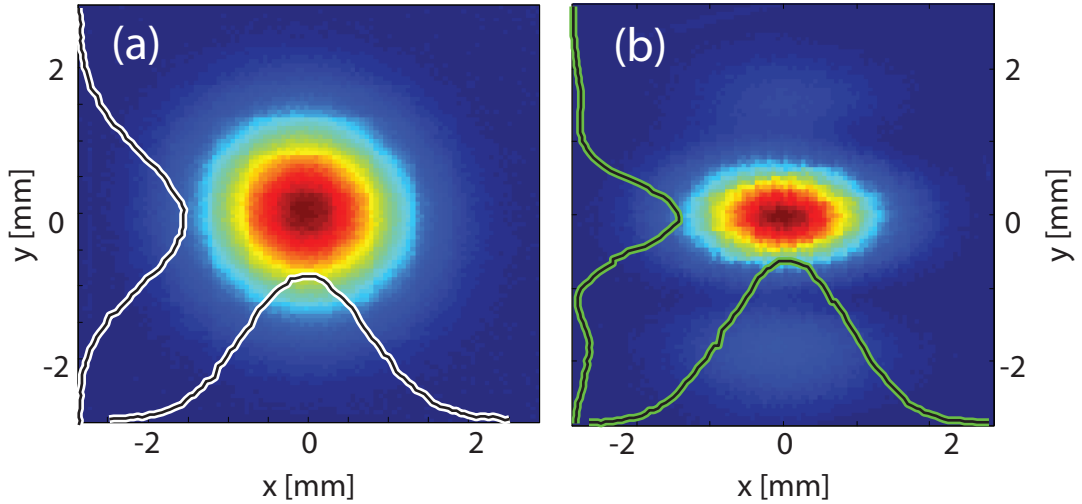


Figure 4.17: Scanning THG microscopy images of 100 nm diameter polystyrene beads, with (a) a uniform linear polarization state and (b) a $\pi/2$ phase jump on the p polarization component.

To validate that the enhanced spatial resolution beam shown in Fig. 4.18(b) originates from the spatially inhomogeneous polarization state distribution, we reconstructed the enhanced spatial resolution focal plane THG scattering by combining the measured focal spot with a spatially uniform linear polarization and the phase

difference obtained from the THG tomography algorithm. The calculated THG scattering signal spatial distribution using $|\mathbf{P}^{(3)}(x, y)|^2$ is shown in Fig. 4.18(c), and shows excellent agreement with the resolution enhancement image shown in Fig. 4.17(b). This result validates the principle of operation of THG scattering suppression in the wings of the spatial mode of a microscope focal spot through a spatially-varying distribution of polarization states.

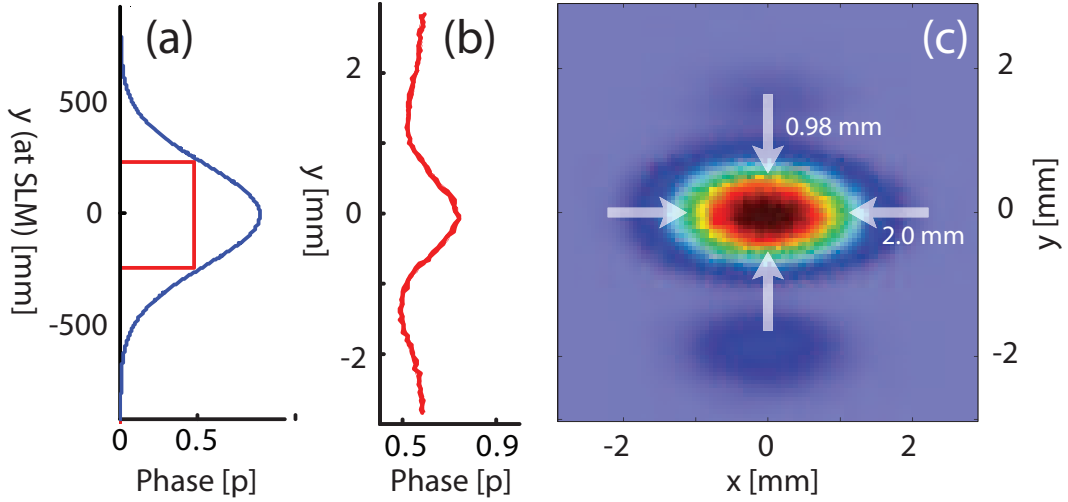


Figure 4.18: (a) Phase applied to the SLM p polarization, relative to the beam intensity distribution. (b) Retrieved phase using tomographic phase retrieval. (c) Reconstructed THG image distribution (see text).

In Fig. 4.17(b), a spatial resolution enhancement of a factor of 2 is attained. We show in Fig. 4.19(a) scan of the transverse THG resolution enhancement as width of the “top-hat” phase profile applied at the SLM is varied over the size of the beam. The reduction in the transverse resolution is plotted as a function of the fractional radius of the polarization switch radius, r_s/w , where w describes the spatial FWHM of the beam incident on the reflective SLM.

Since the resolution enhancement is achieved by suppressing the THG scattering via circular polarization, one expects that the total collected THG energy will decrease as the switch radius r_s decreases. The spatially integrated PMT signal is plotted in Fig. 4.19(b) to show the change in collected energy. As expected, as $r_s \rightarrow 0$,

the collected THG energy also vanishes.

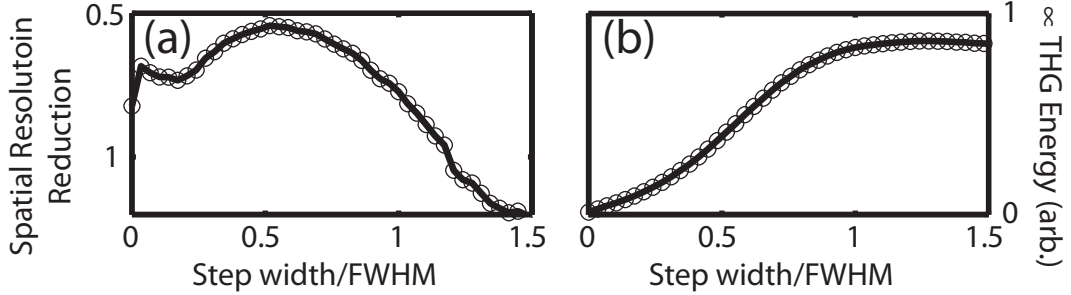


Figure 4.19: Enhanced resolution is shown as a function of polarization switched radius r_s/w . Also, corresponding decrease in the collected THG energy signal is shown.

Although the THG from circular polarized light is not completely suppressed in anisotropic material, the ratio between the circular to linear polarized light could be quite small for some material. For instance, for a cubic symmetry Si crystal with (100) orientation, the ratio $\frac{THG_{lin}}{THG_{circ}} = \frac{1}{4}|\sigma|^2$, where for $\lambda \approx 1 \mu\text{m}$ sigma has a value of 0.2 has been demonstrated [118]. This gives a ratio of $\frac{THG_{lin}}{THG_{circ}} = 100$.

4.4 Summary

In summary, we have demonstrated a method for improved transverse spatial resolution in THG microscopy. This new approach capitalizes on the polarization dependence of THG scattering. In particular, THG scattering is identically suppressed in isotropic media for an incident circularly-polarized field. The technique is demonstrated by imaging an spatially-inhomogeneous polarization state distribution produced by a reflective SLM into the focal plane of a scanning THG microscope. A transverse spatial resolution of up to 2 times enhancement is demonstrated. We are investigating the theoretical limitations of polarization switched THG resolution enhancement. Improved spatial resolution of this technique may prove valuable in microscopy of nano-scale objects. Many anisotropic structures provide sufficient contrast

between THG scattering with linear and circularly polarized to apply this technique. Moreover, deterministic control of the focal field polarization state distribution may provide a route to probing the anisotropic nonlinear response of nano-scale objects. Use of a 2D SLM will enable resolution enhancement over the full extent of the beam.

Moreover, we introduced a new technique based on coherent third harmonic generation microscopy, to characterize the spatially-varying polarization state distribution at the focal field in a nonlinear scanning laser microscope. We developed and demonstrated a non-iterative, *in-situ* phase retrieval algorithm, and measured polarization projection of THG images of a polystyrene bead. Spatially inhomogeneous polarization states were constructed by imaging an SLM to the focal plane of the microscope objective. We determined the spatially-varying polarization states by locally probing the field through THG generated by an isotropic microsphere with a diameter much smaller than the focal field. The tomography technique can be used to probe the focal field polarization state for a wide range of microscopy setups, and is applicable for obtaining polarization states and anisotropic responses from many types of linear and nonlinear optical microscopy.

Chapter 5

Holography

5.1 Introduction

In this chapter, I will discuss an alternative to time consuming laser-scanning microscopy method for 3-D nonlinear imaging, called nonlinear holography [119]. As described in chapter 3, to date, imaging in nonlinear microscopy, like SHG and THG microscopy, has largely been restricted to laser-scanning microscopy due to the relatively high peak intensity required for signal generation. While nonlinear scanning microscopy is a valuable and powerful tool, it is inherently limited by low image acquisition rates. The standard implementation of this technique requires a tightly focused fundamental pulse to be mechanically scanned through each volume element in a 3-D volume (voxel), where images are assembled by serially collecting a nonlinear signal from each voxel. The refresh rate of image acquisition for nonlinear microscopy often fails to capture dynamics of a process under study and presents a significant barrier for application of nonlinear microscopy to many areas [42, 43, 37, 41, 40, 38].

By contrast, a hologram is capable of storing 3-D optical field information in a 2-D image. Holography was first suggested by Gabor [1] though his work on electron microscopy. He suggested a two step process of recording of the interference pattern

of the scattered wave from an object, called the object wave, and a known reference wave on a photographic film, followed by reconstruction of the object field (phase and amplitude) by re-illuminating the recording interference pattern by an optical replica of the reference wave. The recorded interference pattern, the hologram, he showed would contain information about the 2-D object field.

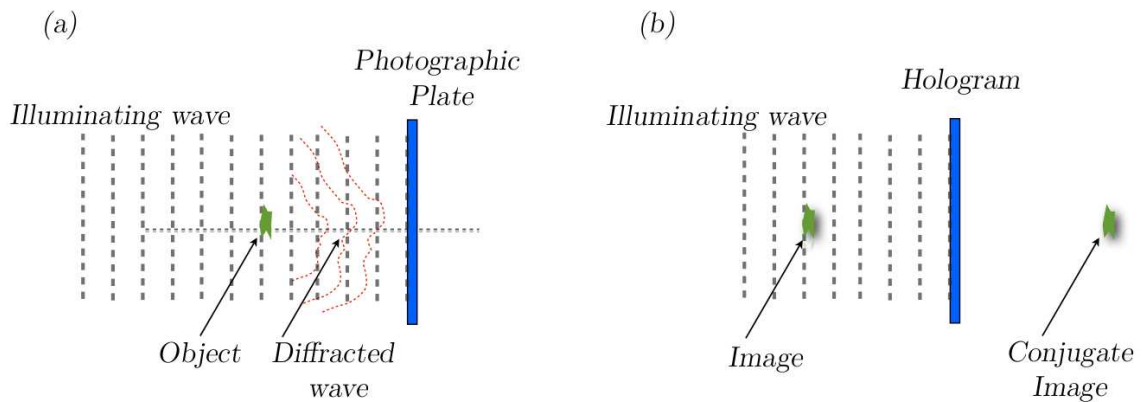


Figure 5.1: Gabor's in-line configuration for holographic recording a) The interference pattern between the incident reference plane wave is recorded by a recording medium. Image reconstruction b), is accomplished by illuminating the hologram by the reconstruction beam, identical to the incident reference beam used for creating the hologram. The image of the object will appear where the object was located during the recording process. A conjugate image (twin-image) will also appear on the other side (the conjugate plane) of the recorded hologram, in line with the real image object.

In the experimental setup suggested by Gabor, shown in Fig. 5.1, both the object wave and the reference wave would be propagated along the optical axis and recorded on a recording medium normal to the optical axis. This so called in-line, or on-axis setup, suffered from unwanted component, namely twin image, which obscured both phase and the amplitude of the reconstructed images. It wasn't until 1960's when E. N. Leith and J. Upatnieks [3, 2] made an improvement to Gabor's technique by introducing an off-axis holography that overcame the twin image problem. In the developed off-axis reference technique, the source of illumination for both object and

reference is highly coherent cw laser. Moreover, reference wave was incident at an angle with respect to the object wave. As a result, when the hologram was illuminated with the original reference beam, the reconstructed images (twin images) were separated from each other. The angle between the reference and the object wave determined the degree of this separation, and the coherence of the beams ensured good interference pattern. Figure 5.3 illustrates this technique.

This early work predated digital cameras and required acquisition by photographic film. Recording the holographic interferograms with a CCD camera has opened a vast field of digital holography, leading to significant improvements in speed of hologram processing. Using digital holograms, 3D microscopy images can be computed numerically from a single image capture [4, 5, 6, 7]. In these techniques, a digital hologram is recorded by interference with a known reference wave, which allows the complex electric field to be determined at the CCD camera. The complex field can be numerically back-propagated to the sample region to obtain 3D image information [89].

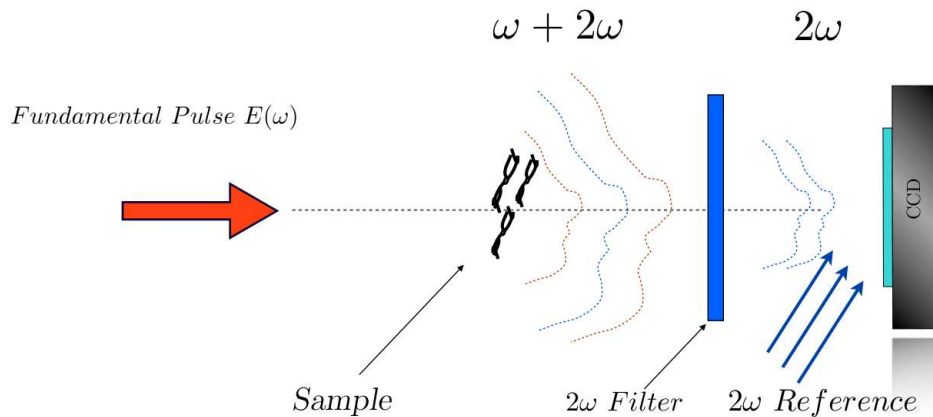


Figure 5.2: In off-axis nonlinear holography the sample is illuminated by a fundamental short pulse. The residual fundamental beam will be filtered by a bandpass chromatic filter, while the second harmonic emerging from the sample will interfere with a second harmonic reference beam. The interference pattern will be recorded by a EMCCD camera.

The principle of nonlinear holography introduced in this thesis is similar to its developed linear counterpart [4, 5, 6, 7]. In nonlinear holography, however, the interference pattern is formed by the nonlinear signal from the sample and a SHG reference wave, derived from the same laser source, illustrated in Fig. 5.2. In this chapter I will discuss the fundamental principles of linear holography which will later on be applied to label-free nonlinear holography of biological specimens.

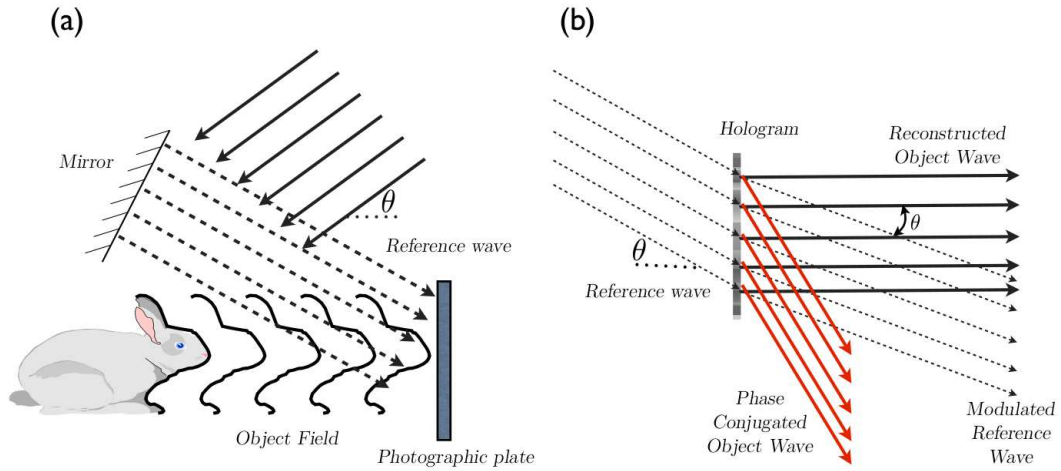


Figure 5.3: Off-axis holography setup: recording a) the interference pattern of the object beam and a reference beam incident on the photographic plate with an angle θ with respect to the object beam. In reconstruction b) of the object beam, the hologram is illuminated with the same reference beam. In off-axis holography, however, the phase conjugated object image is separated from the real image with an angle θ .

5.2 Digital Recording in Off-Axis Holography

In off axis holography a monochromatic reference wave $\mathbf{E}_{\text{ref}}(x, y)$ and the wave from the object $\mathbf{E}_{\text{obj}}(x, y)$ forms an interference pattern recorded by a CCD. The resulting hologram is electronically recorded and stored. The object is in general a three dimensional body, located at an average distance z_{obj} from the CCD. The recorded interference intensity $I_H(x, y)$ can be described as,

$$\begin{aligned}
I_H(x, y) &= \frac{1}{2}nc\epsilon_0 |\mathbf{E}_{\text{ref}}(x, y) + \mathbf{E}_{\text{obj}}(x, y)|^2 \\
&= \frac{1}{2}nc\epsilon_0 [\mathbf{E}_{\text{ref}}(x, y) \cdot \mathbf{E}_{\text{ref}}^*(x, y) + \mathbf{E}_{\text{obj}}(x, y) \cdot \mathbf{E}_{\text{obj}}^*(x, y) \\
&\quad + \mathbf{E}_{\text{ref}}^*(x, y) \cdot \mathbf{E}_{\text{obj}}(x, y) + \mathbf{E}_{\text{ref}}(x, y) \cdot \mathbf{E}_{\text{obj}}^*(x, y)]. \quad (5.1)
\end{aligned}$$

The first two terms are the intensities of the reference and the object waves, and the last two terms are the real and the virtual images, respectively [89]. Here, (x, y) are the transverse coordinates in the plane where the hologram is recorded. The linear polarization of the reference beam selects co-polarized object beam components to form interference. Off-axis holography enables complete extraction of the complex field of the object beam, provided that the spatial carrier frequency of the interference fringes is sufficiently high. In digital holography, a two-dimensional Fourier transform of the hologram I_H is used to separate the real and virtual images from the static terms in the transformed space (k_x, k_y) . The angle of interference between the object and reference waves is chosen to provide a sufficiently high carrier spatial frequency to prevent aliasing of these three terms.

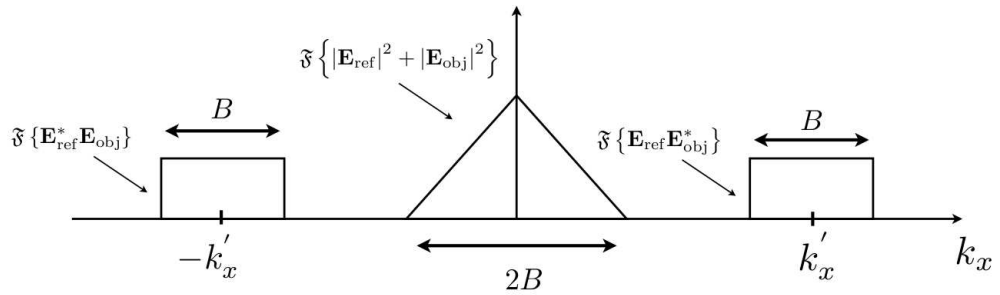


Figure 5.4: In frequency domain, the real and virtual images will be separated from the DC term (intensity of the reference and the object waves in the frequency domain), provided that the spatial carrier frequency of the interference pattern (which depends on the angle between the incident reference beam with respect to the object wave) is sufficiently high with respect to the bandwidth (B) of the object wave

5.2.1 Obtaining 3-D Images from 2-D Data

The simplest form of a hologram is a hologram of a single point-source, which produces a series of concentric rings, identical to Fresnel zone plate lens (FZP) [120]. For instance, if we assume our reference field is a plane wave with amplitude a , the the recorded hologram of a point source at a distance z_0 from the recording medium can be calculated to be [89],

$$\begin{aligned} I &\propto \left| a + \frac{ik_0}{2\pi z_0} \exp \left[\frac{ik_0}{2\pi z_0} (x^2 + y^2) \right] \right|^2 \\ &= a^2 + \left(\frac{k_0}{2\pi z_0} \right)^2 + \frac{k_0}{\pi z_0} \sin \left(\frac{k_0}{2z_0} (x^2 + y^2) \right) \end{aligned} \quad (5.2)$$

As any object can be considered to be composed of many point sources, it follows that the hologram of an object can be understood as the superposition of many FZP. Moreover, quality of the images form by a hologram depends on the property of the hologram constructed. For instance, the resolution of Gabor's hologram, depends on the wavelength and the coherence of the illuminating light, along with the $NA = \frac{D}{f}$ of the recording hologram, where $D = 2r_N$ is the diameter, and $f \approx \frac{D\delta_{r_N}}{\lambda}$ is the focal length of the FZP. Here, r_N is the radius of the outermost zone of the FZP with width δ_{r_N} . (The resolution of the recording media also effect the resolution, and will be discussed in section 5.2.3).

Three-dimensional imaging capability of a hologram can be considered by investigating the phase of the recorded Fresnel zone in Eq. (5.2). The spatial rate of change of the phase of Eq. (5.2), in x -direction, is the local fringe frequency $f_{local} = \frac{x}{\lambda z_0}$. The further away the point source lies from the recording medium, for a given λ and a fixed point on the hologram, the higher the local frequency will be. Therefore, the depth information is encoded within the phase, or the local fringe frequency of the FZP. Furthermore, if we consider two points sources along the optical axis, the

recorded hologram will be the superposition of two FZP's with different focal length, and local fringe frequency, and once again the depth information is encoded in phase of the recorded FZP. Figure 5.5 shows the hologram and the reconstruction of two point sources, located at z_1 and z_2 from the recording medium. Figure 5.5(a) show the recorded hologram, and Fig. 5.5(b) the reconstruction of the point sources using the numerical reconstruction algorithm explained in next section.

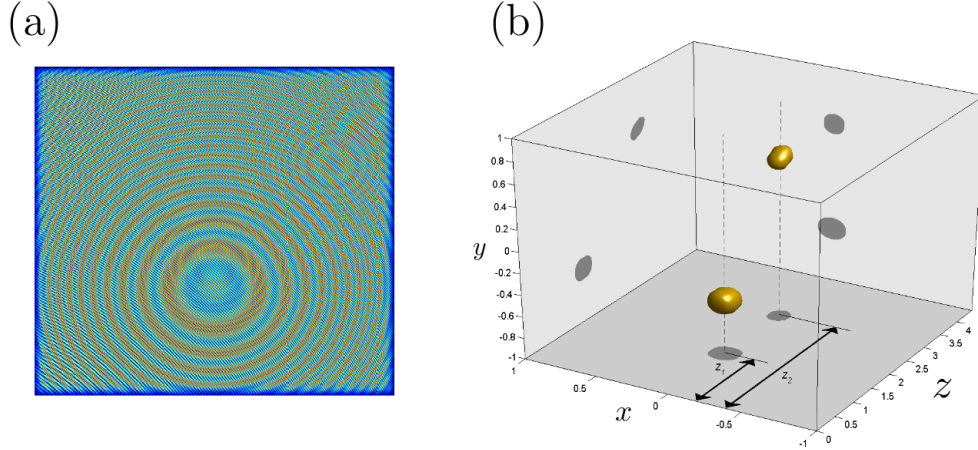


Figure 5.5: Off-axis hologram a) of two point sources separated in the direction of the optical axis and laterally. The hologram of the two point sources are the superposition of two Fresnel zones with focal lengths f_1 and f_2 . In the reconstruction, b) the two points sources will appear at an average distance $z_1 = f_1$ and $z_2 = f_2$.

5.2.2 Numerical Reconstruction of the Object Field

In digital holography, numerical reconstruction of the field requires isolation of the complex object field, followed by back propagation through the object space to recover the three dimensional object distribution. The object field recorded at the CCD is obtained by filtering the real image sideband of the numerically 2D Fourier transformed digital hologram. An inverse 2D transform of this sideband yields the quantity $\mathbf{E}_{\text{ref}}^*(x, y) \cdot \mathbf{E}_{\text{obj}}(x, y)$. The object field is obtained by multiplying by the conjugate of plane wave reference field, whose intensity is independently measured for each acquired hologram. Once the object field $\mathbf{E}_{\text{obj}}(x, y)$ has been retrieved, it will

be propagated a distance z_{obj} to retrieve the phase and the intensity of the object.

The numerical propagation of the object field from CCD plane through the object plane can be performed based on Rayleigh-Sommerfeld diffraction formula, which is computationally very expensive. There are, however, many efficient numerical methods available[121, 122, 4]. We use an angular spectrum method to yield the field at a propagation distance z [89].

In angular spectrum method one assumes that the field can be written in terms of superposition of many monochromatic plane waves with spatial frequencies k_x and k_y . Then each plane wave will be propagated through transfer function of propagation through free space $\exp [ik_z z]$, where $k_z^2 = 1 - k_x^2 - k_y^2 = \left(\frac{2\pi}{\lambda}\right)^2$. After the propagation is done, the field will be recovered by superposition of all plane waves.

Numerical propagation using angular spectrum method, starts by decomposing the object field by its angular spectrum,

$$\mathbf{A}(k_x, k_y, z = 0) = \int_{-\infty}^{\infty} \int_{-\infty}^{\infty} \mathbf{E}_{obj}(x, y, z = 0) \exp [-i(k_x x + k_y y)] dx dy \quad (5.3)$$

where $\mathbf{A}(k_x, k_y, z = 0)$ is the angular spectrum of the object field at the recording medium where the hologram has been recorded (hologram plane), and $k_x = 2\pi f_x$ and $k_y = 2\pi f_y$ are the spatial frequencies. Each plane wave, thereafter, will be propagated through space using the free space propagation transfer function,

$$H(k_x, k_y) = \exp [ik_z z] \quad (5.4)$$

$$\begin{aligned} &= \exp \left[i \sqrt{k^2 - k_x^2 - k_y^2} z \right] \\ &= \exp \left[i \sqrt{\left(\frac{2\pi}{\lambda}\right)^2 - k_x^2 - k_y^2} z \right] \end{aligned} \quad (5.5)$$

The reconstructed image at distance z can be found by,

$$\mathbf{E}(x, y, z) = \int_{-\infty}^{\infty} \int_{-\infty}^{\infty} \mathbf{A}_{\text{obj}}(k_x, k_y, z = 0) \exp \left[i \sqrt{\left(\frac{2\pi}{\lambda}\right)^2 - k_x^2 - k_y^2} z \right] \exp [i(k_x x + k_y y)] dk_x dk_y \quad (5.6)$$

5.2.3 Resolution in Digital Holographic Microscopy

In off-axis digital holography the resolution of the reconstructed image depends on the how well the interference pattern between the reference wave and the object field is spatially resolved. The maximum spatial frequencies k_x (considering one dimension only) to be resolved is determined by the wavelength, and the maximum angle θ_{max} between the reference and object field and is given by [89],

$$k_x = \frac{2 \sin\left(\frac{\theta_{max}}{2}\right)}{\lambda}. \quad (5.7)$$

Moreover, Shannon's sampling criterion requires each interference fringe to be sampled by at least two CCD pixel to resolve the fringe spatial frequency, that is $k_x = \frac{1}{2\Delta x}$, where Δx is the pixel pitch. Therefore, the maximum spatial frequency recorded by the CCD is limited by the pixel pitch Δx , and therefore limiting the radial resolution $r_x = 0.61 \frac{\lambda}{\sin(\theta)} \approx \frac{1}{k_x} \approx 2\Delta x$. For instance for a CCD camera with $\Delta x = 16 \mu\text{m}$, the smallest object that can be resolved is about $32 \mu\text{m}$, well above the Rayleigh resolution.

One way to get around this problem is to magnify the holographic image by using a high NA microscope objective. This is the main goal of digital holographic microscopy. By inserting an objective microscope between the object and the hologram one achieves a reduction of the spatial frequency component k_x, k_y by the magnification factor. This idea is illustrated in Fig. 5.6. In holographic microscopy, the object wave is collected by a high NA objective and imaged at a distance z_{obj} from the

CCD. After the recording of the hologram with CCD and isolating the object wave described in section 5.2, it will be propagated a distance z_{obj} to the image plane, to retrieve the magnified object intensity and phase. The original size of the object sample can be achieved by normalizing the image coordinates by the magnification factor. The magnification of the imaging system in the holographic setup can be modified to match the sampling capacity of the CCD camera, to reach the diffraction limited resolution.

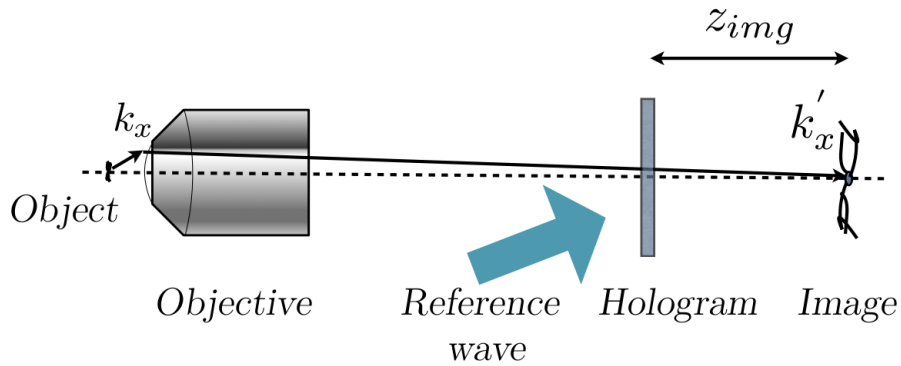


Figure 5.6: By inserting an objective microscope between the object and the hologram one achieves a reduction of the spatial frequency component k_x, k_y by the magnification factor. (Only k_x is shown here)

5.3 Summary

In summary, we saw 3-D images of an object can be achieved by recording a two-dimensional interference pattern between a reference wave and object wave. In biological nonlinear imaging where the traditional method has largely been restricted to low image acquisition rates by using laser-scanning microscopy, nonlinear holographic microscopy could potentially be used to brake the barrier for faster imaging acquisition to map out the fast dynamics of the living tissues.

Chapter 6

Label-Free Second Harmonic

Generation Holographic

Microscopy of Biological Specimens

6.1 Introduction

The formation of images of biological specimens with coherent nonlinear scattering opens unique image formation contrast due to the nature of nonlinear interactions. This has motivated extensive investigation of both second harmonic generation (SHG) and third harmonic generation (THG) optical microscopy [123, 86, 96]. Work on SHG and THG microscopy has been largely restricted to laser-scanning microscopy due to the relatively high peak intensity required for signal generation. However laser scanning of three dimensional (3D) images takes considerable time to form a 3D image because each voxel must be acquired serially. To address this issue, harmonic holography using small nanoparticles for labeling and to provide a strong SHG signal was recently introduced to form high-speed images [119]. We here demonstrate label free 3D SHG holographic microscopy of biological specimens using a femtosecond

oscillator.

SHG microscopy was first introduced less than a decade after the first demonstration of the laser [124, 64]. Three dimensional images were formed shortly after by scanning the focal spot of a a continuous-wave laser to form 3D images [98]. This early work had extremely slow image acquisition speeds. With the advent of femtosecond laser pulses, acquisition time of laser-scanning SHG images has reduced sufficiently to enable wide-spread use in biological imaging. This technique has proved to be a powerful tool for imaging intrinsic subcellular signals from endogenous proteins such as microtubule, myosin and collagen in living tissues [125, 24, 28]. Since SHG microscopy forms images for structures comprising ordered non-centrosymmetric molecules or tissues, it provides a novel optical image contrast mechanism [126, 127, 128] that have found use in *in-vivo* biological studies.

In SHG microscopy, the measured signal is proportional to the square of the illumination intensity. As a consequence, the signal is localized to a small volume near the focus. This confers a significant advantage, automatically providing nonlinear optical sectioning and the ability to form high quality images in scattering media [22, 23]. Other nonlinear microscopies inherit these advantages while also offering rich possibilities for additional contrast mechanisms in biological imaging. THG microscopy [15, 16, 32] forms images at interfaces, and chemically-specific coherent nonlinear microscopy is obtained through use of coherent anti-Stokes Raman scattering [18, 84].

The advantages of the intensity-dependent response in nonlinear microscopy require high intensities to obtain images with a suitable signal-to-noise ratio. Specimen damage limits the usable intensity [86]. The damage mechanisms can be broadly divided into thermal loading, where the accumulation of the laser's average power causes detrimental heating, and damage caused by high peak intensities. The incident average power can be reduced while maintaining high peak intensities by reducing the laser pulse duration, or by reducing the laser pulse repetition frequency. However,

peak-intensity damage places an upper limit on the attainable harmonic signal. This is of particular importance in *in vivo* or *ex vivo* biological samples.

While nonlinear scanning microscopy is a valuable and powerful tool, it is inherently limited by low image acquisition rates. The standard implementation of this technique requires a tightly focused fundamental pulse to be mechanically scanned through each volume element in a 3D volume, where images are assembled by serially collecting a nonlinear signal from each voxel. The refresh rate of image acquisition for nonlinear microscopy often fails to capture dynamics of a process under study and presents a significant barrier for application of nonlinear microscopy to many areas [37, 38, 39, 40, 41, 42, 43].

By contrast, a hologram is capable of storing 3D optical field information in a 2D image, and we here combine this technique with the nonlinear SHG contrast mechanism. We make use of off-axis holography introduced by Leith and Upatniek [3, 2], which led to the first 3D imaging image recording. These techniques was reviewed in chapter 5.

Second harmonic generation holography was recently introduced to acquire 3D SHG microscopy images without use of time-consuming laser scanning [50]. This experiment used a 1 mJ, 10 Hz repetition rate femtosecond laser amplifier to image the distribution of 100 nm diameter nanoparticle clusters made of the non-centrosymmetric BaTiO₃ crystal [50]. A subsequent experiment employed a Ti:sapphire oscillator and recorded SHG holograms from mammalian (HeLa) labeled with BaTiO₃ nanoparticles [119].

In this chapter, second-order nonlinear holographic microscopy for three-dimensional imaging, using harmonic generation of endogenous tissue features without nanocrystal labeling, is demonstrated. In these experiments, we report on 3D SHG holography imaging in muscle tissues without extrinsic labels using a Yb:KGW oscillator. The average power and peak intensity are sufficiently low to avoid damage to the biological

specimens. In addition, the 1027-nm center wavelength of the Yb:KGW laser pulses operates in a biological window where the combination of scattering and absorption are exceptionally low [85].

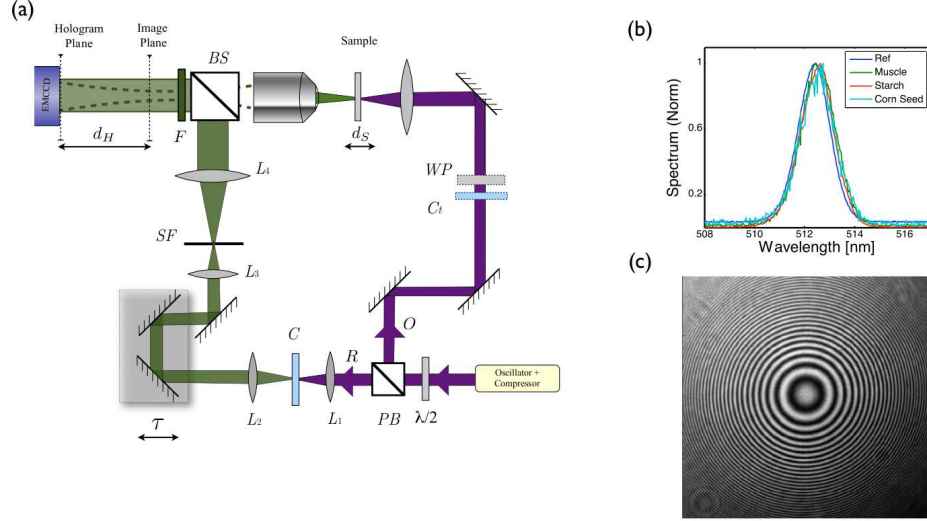


Figure 6.1: (a) Experimental arrangement; see text for details. (b) Second-harmonic spectra measured for the reference beam (blue line) and samples human muscle (green), starch granules (red), and corn seed (cyan). (c) Interference Fresnel rings observed without a sample at the image plane, at time overlap between reference and independently frequency-doubled object pulses.

6.2 Theory

In chapter 5, we described the formation of linear holograms and reconstruction of the object field. Here, I will repeat some of these results.

In our experiments, off-axis digital holograms are formed by recording, using a digital CCD camera, the interference between SHG radiation generated by ordered structure in a specimen and an off-axis reference wave. To describe the recorded hologram, we will consider the electric field of the incident beam illuminating the sample, which takes the form $\mathcal{E}_0(\mathbf{r}_0, t) = \mathbf{E}_0(\mathbf{r}_0)e^{i(\omega_0 t - k_0 z_0)}$, where $\mathbf{E}_0(\mathbf{r}_0)$ describes the spatial distribution of the field strength and ω_0 is the incident field optical radial frequency. The

fundamental field drives a polarization density oscillating at the second harmonic of the incident field given by

$$\mathbf{P}^{(2)}(\mathbf{r}_0) = \frac{1}{2}\epsilon_0\chi^{(2)}(\mathbf{r}_0) : \mathbf{E}_0(\mathbf{r}_0)\mathbf{E}_0(\mathbf{r}_0). \quad (6.1)$$

The nonlinear optical susceptibility $\chi^{(2)}(\mathbf{r}_0)$ is a tensor, whose elements are dictated by the material of the object. Here, $\mathbf{r}_0 = x_0\hat{i} + y_0\hat{j} + z_0\hat{k}$ is the spatial coordinate in the object space.

The second harmonic radiation emerging from the object, $\mathcal{E}_{\text{SHG}}(x, y, t; z) = \mathbf{E}_{\text{obj}}(x, y; z)e^{i(\omega_2 t - k_2 z)}$, contains information encoding the 3D spatial structure of the specimen, and can be described by a Green's function formalism [78].

$$\mathbf{E}_{\text{obj}}(x', y'; z) = -\mu_0\omega_2^2 \int \int \int_V \mathbf{G}_0(\mathbf{r}, \mathbf{r}_0) \cdot \mathbf{P}^{(2)}(\mathbf{r}_0) dx_0 dy_0 dz_0 \quad (6.2)$$

where we assume $z \gg z_0$, $\omega_2 = 2\omega_0$, $k_2 = \omega_2 n/c$. The dyadic Green's function is given by

$$\mathbf{G}_0(\mathbf{r}, \mathbf{r}_0) = \frac{e^{ik_2 r'}}{4\pi r'} e^{-ik_2(x'x_0/r' + y'y_0/r' + z'z_0/r')} \begin{bmatrix} (1 - x'^2/r'^2) & -x'y'/r'^2 & -x'z'/r'^2 \\ -x'y'/r'^2 & (1 - y'^2/r'^2) & -y'z'/r'^2 \\ -x'z'/r'^2 & -x'y'/r'^2 & (1 - z'^2/r'^2) \end{bmatrix}, \quad (6.3)$$

where $r' = \sqrt{x'^2 + y'^2 + z'^2}$.

The radiated SHG field is collected by a microscope objective and a hologram is formed by interference with an independently frequency-doubled reference, $\mathbf{E}_{\text{ref}}(x, y)e^{i2\omega_0 t}$. The hologram is recorded with a lateral magnification M_l , and its intensity pattern

is given by

$$\begin{aligned}
I_H(x, y) &= \frac{1}{2}nc\epsilon_0 |\mathbf{E}_{\text{ref}}(x, y) + \mathbf{E}_{\text{obj}}(x, y)|^2 \\
&= \frac{1}{2}nc\epsilon_0 [\mathbf{E}_{\text{ref}}(x, y) \cdot \mathbf{E}_{\text{ref}}^*(x, y) + \mathbf{E}_{\text{obj}}(x, y) \cdot \mathbf{E}_{\text{obj}}^*(x, y) \\
&\quad + \mathbf{E}_{\text{ref}}^*(x, y) \cdot \mathbf{E}_{\text{obj}}(x, y) + \mathbf{E}_{\text{ref}}(x, y) \cdot \mathbf{E}_{\text{obj}}^*(x, y)]. \quad (6.4)
\end{aligned}$$

The first two terms are the intensities of the reference and the object waves, and the last two terms are the real and the virtual images, respectively [89]. Here, (x, y) are the transverse coordinates in the plane where the magnified hologram is recorded. The linear polarization of the reference beam selects co-polarized object beam components to form interference.

Off-axis holography enables complete extraction of the complex field of the object beam, provided that the spatial carrier frequency of the interference fringes is sufficiently high. In digital holography, a two-dimensional Fourier transform of the hologram I_H is used to separate the real and virtual images from the static terms in the transformed space (k_x, k_y) . The angle of interference between the object and reference waves is chosen to provide a sufficiently high carrier spatial frequency to prevent aliasing of these three terms.

Numerical reconstruction of the field requires isolation of the complex object field, followed by back propagation through the object space to recover the three dimensional object distribution. The object field recorded at the CCD is obtained by filtering the real image sideband of the numerically 2D Fourier transformed digital hologram. An inverse 2D transform of this sideband yields the quantity $\mathbf{E}_{\text{ref}}^*(x, y) \cdot \mathbf{E}_{\text{obj}}(x, y)$. The object field is obtained by multiplying by the conjugate of plane wave reference field, whose intensity is independently measured for each acquired hologram. Once the object field $\mathbf{E}_{\text{obj}}(x, y)$ has been retrieved, we use angular spectrum method to yield the field at a propagation distance to yield the field at a propagation distance

z [89].

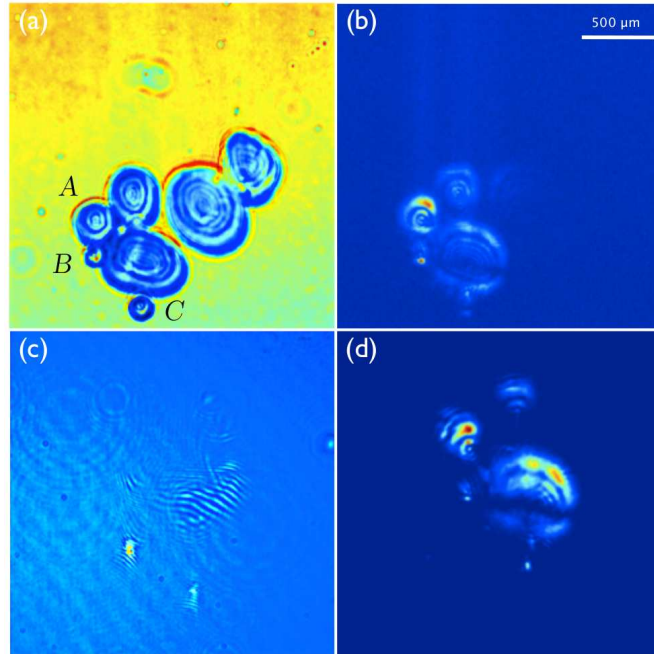


Figure 6.2: A cluster of starch granules (scale is the same for all figures): (a) White light; (b) second-harmonic from the sample; (c) measured hologram; (d) reconstruction at image plane.

6.3 Experimental Setup

The ultrashort laser pulses are derived from a home-built Yb:KGW laser oscillator. Briefly, a 20 W diode array at 975 nm (Apollo) is free-space imaged and focused into a 2 mm long, 5%-at doped Yb:KGW crystal (NovaPhase). The standing-wave cavity has one $105 \mu\text{m}$ ($1/e^2$) waist overlapping the pump focus inside the crystal, and a second $100 \mu\text{m}$ on a 4% modulation depth SESAM (BATOP). The SESAM and an intracavity compressor lead to stable modelocked pulses with 4.5 nm optical bandwidth centered at 1027 nm. We obtain a 70-MHz train of pulses capable of delivering 14 nJ of pulse energy.

The holographic microscopy setup is based on a modified Mach–Zehnder interferometer as shown in Fig. 6.1(a). A half wave plate (Tower Optical) followed by

polarizing beamsplitter cube (PB), controls the balance between the beam energies in the reference and the object arms. In the reference arm, the fundamental beam is focused into a 0.1 mm thick KDP crystal (C , EKSPLA) with a $f_1 = 50$ mm lens to generate the SHG reference beam. This reference is collected and collimated with a $f_2 = 125$ mm lens, to fill the back aperture of the focusing objective (f_3) of the spatial filter (SF , Newport model 910A). The reference beam is spatially filtered with $15 \mu\text{m}$ pinhole and recollimated with a $f_4 = 100$ mm lens. This results in a ~ 20 mm diameter reference beam with high spatial phase purity. In the object arm, the beam is focused into the sample with a Meiji S-Plan 4×0.1 NA objective. The $1/e^2$ focal spot radius is measured to be $35 \mu\text{m}$, in good agreement with calculated value of $32 \mu\text{m}$. The SHG signal from the sample is collected with a Zeiss Epiplan 50×0.5 NA objective. Both focusing and collection objectives are mounted in tip-tilt mounts (Thorlabs) on x, y, z translation stages (OptoSigma) to allow for precise alignment. The specimens are held in a custom microscope slide holder on an x', y', z' stage. The sample and reference SHG beams are combined with a non-polarizing beam splitter (BS , Thorlabs). The combined signal is first filtered by a 10 nm bandpass filter centered at 510 nm (Thorlabs, FB510-10) and a colored glass bandpass filter (FGS900). To record the holograms, we use an Andor Newton electron-multiplying charge-coupled device (EMCCD) camera, thermo-electrically cooled to -65°C , that has 1600×400 pixels with a $16\mu\text{m}$ pixel pitch. The high sensitivity of the electron-multiplying gain, along with its low noise cooled CCD, allows us to record low intensity SHG holograms with high signal-to-noise and short integration times. When processing the holograms presented below, we crop a relevant 400×400 pixel area.

The normalized spectrum of the second harmonic reference beam and SHG signals from samples under study are shown in Fig. 6.1(b). The spectra are centered around 513 nm, with an optical bandwidth of ≈ 2.3 nm. Without a sample in the microscope, we confirmed that the microscope glass slide interfaces did not yield any measurable

second-harmonic signal.

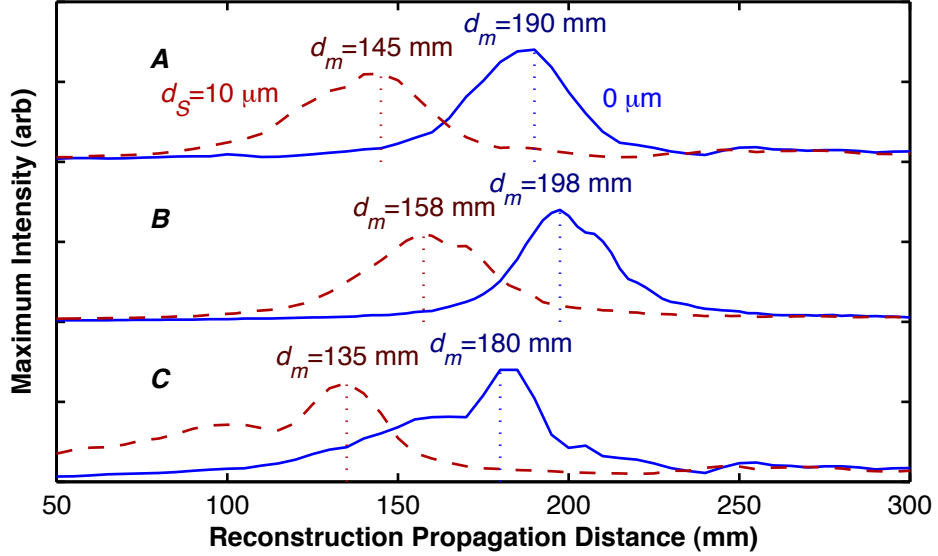


Figure 6.3: Peak intensities, in local regions around starch grains marked *A*, *B* and *C* in Fig. 6.2, with varying reconstruction distance d_H . The peaks correspond to the axial plane where each grain is focused. Comparison between two object planes d_S allows us to estimate the microscope axial magnification.

Due to the short coherence length of the pulses used to form the hologram ($\ell_c \approx 250 \mu\text{m}$), the object and reference beams must be temporally overlapped. This is accomplished with a delay arm in the reference arm. In order to co-locate the pulses in time, the object fundamental beam is independently frequency-doubled before the microscope in a 4 mm KDP crystal (C_t), and combined with the reference without a sample. The interference fringes between the object and reference beams are observed as the length of the reference arm is changed by the translation stage. Time overlap is optimized by maximizing the depth of modulation of the interference pattern. Figure 6.1(c) shows the Fresnel interference pattern for an on-axis hologram setup. The holographic data shown for the rest of this paper are taken in an off-axis configuration.

We measured the lateral magnification of our microscope by illuminating a $12.5\text{-}\mu\text{m}$ pitch wire calibration mesh at the object plane with the SHG generated before

microscope. We estimate a lateral magnification of $|M_l| \approx 67$. The resolution of our microscope is determined by two factors: the lateral magnification along with the pixel size of the CCD camera, and the collection objective’s numerical aperture. We measured the resolution to be $0.85\mu\text{m}$, by collecting the SHG images from a 80 nm gold nano-bead.

6.4 Results

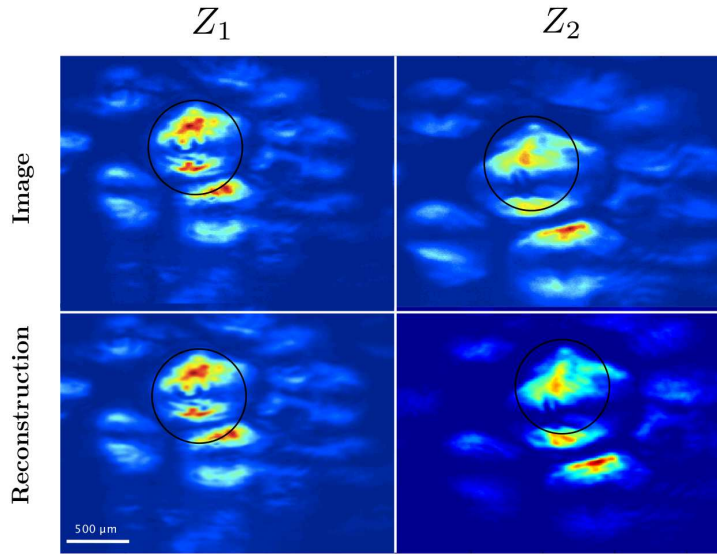


Figure 6.4: Image and reconstruction of corn seed at two different image and reconstruction planes.

In Fig. 6.2, we show holographic reconstructions of a cluster of potato starch. Figure 6.2(a) shows a linear microscopy image of the starch illuminated with white light, while Fig. 6.2(b) shows the SHG generated purely in the sample collected near the image plane. The SHG signal is concentrated near three starch granules, labeled A , B and C for comparison with Fig. 6.3, where the intensity of the incident fundamental beam is greatest. The hologram, recorded at distance $d_H = 25$ cm from the image plane, is shown in Fig. 6.2(c). The hologram was reconstructed using the analysis

described in the theory section and is shown in Fig. 6.2(d).

Translating the starch cluster shown in Fig. 6.2 allows us to characterize the axial magnification of the microscope. In Fig. 6.3, we show the maximum reconstructed intensity, in a restricted region around the granules labeled A , B and C , for different reconstruction distances d_H . The local peak intensities reconstructed from the hologram in Fig. 6.2(c) are shown with a solid blue line. From the data, we see that the granules come into focus at distances $d_H = 190, 198, 180$ mm for A, B, C . Next, we translate the sample by $d_S = 10 \mu\text{m}$ and record a new hologram. The reconstruction peak intensities are shown by the red dashed line, and the reconstruction distances for the granule foci are observed to shift by $\Delta d_H \approx 47$ mm. We attribute the decrease in the peak intensity for the $d_S = 10 \mu\text{m}$ data to a reduced light collection angle of the collection objective when the sample is translated. The change in the width may be due to different lateral magnification when the sample is reconstructed at a different image plane. The large width and characteristic structure of peak C as compared to A and B arises because the interference rings from granules A and B enter into the region around C . The axial magnification is calculated by $M_a = \Delta d_H / d_S \approx 4700$, in good agreement with the theoretical value of $M_a = M_l^2 \approx 4500$.

The validity of our reconstruction algorithm was investigated by comparing second harmonic images to holographic images back propagated to the same SHG image acquisition plane, using a prepared corn seed slide (The Microscope Store, LLC). Figure 6.4 shows second harmonic images taken at two different camera positions $Z_1 = 14$ cm and $Z_2 = 6$ cm from the image plane, corresponding to $17 \mu\text{m}$ displacement in sample space. A hologram was also recorded, numerically reconstructed, and propagated to the plane at which the two reference SHG images were acquired. It can be seen that different features come into focus for different camera positions, corresponding to different slices within the sample. We have marked them for readability. The small discrepancies between the images and reconstructions may be due

to potential phase variations across the reference beam, which we assume to be a plane wave. These variations can be compensated for with many existing algorithms [129, 130, 131].

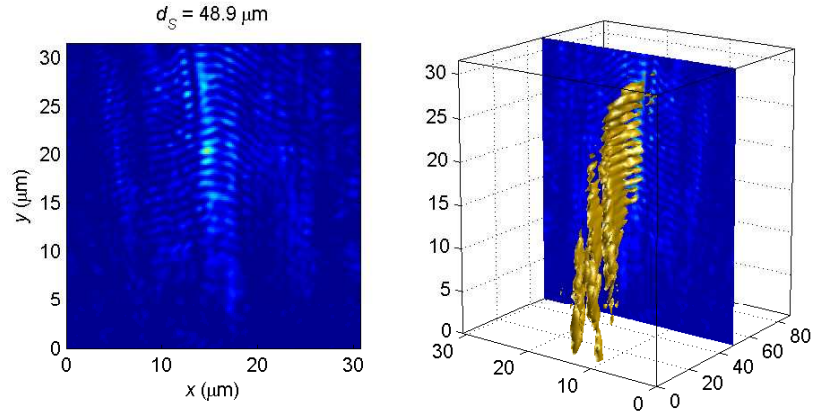


Figure 6.5: Reconstruction of hologram showing several separate human muscle fibrils. The animation shows the assembly of reconstruction planes into the three-dimensional depiction of the sample.

Biological tissues such as collagen, myosin, and muscle fibrils exhibit a strong second harmonic signal due to their highly organized molecular structures [24, 28, 27, 14, 13, 132, 26]. This allows us to record second harmonic holographic microscope images without the need for additional labels. The incident pulse energy was adjusted to 4 nJ, corresponding to a peak intensity of around 300 MW/cm². With a 500 ms integration time, a strong second harmonic signal was observed on the EMCCD camera. The signal was clearly visible at substantially shorter exposure times (50 ms), but the images suffered from lower signal-to-noise and slow readout artifacts from the camera. The deterioration of the signal-to-noise could be partly mitigated by further lowering the temperature of the camera (down to -100° with water cooling). A 3D reconstruction of the muscle sample is shown in Fig. 6.5. The animation shows the series of reconstruction planes, showing the intensity source data from which the iso-surface is calculated. In particular, we see two closely-spaced fibrils at reconstruction distances $d_s = 25, 35 \mu\text{m}$. These results demonstrate the utility of this laser source

and microscopy setup to biologically relevant samples.

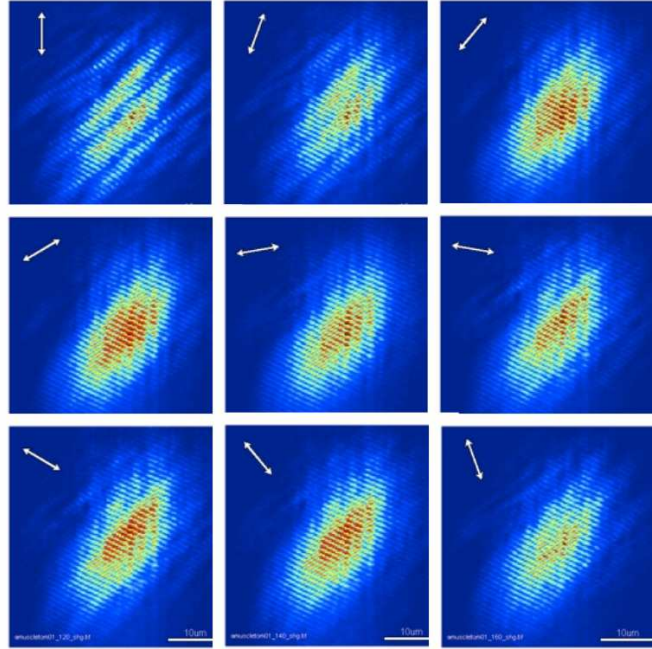


Figure 6.6: Polarization dependence of the muscle tissue.

To ensure the origin of the signal is indeed from the muscle tissue, we insert a half wave plate in the object arm, before the condenser. At the image plane, we record the second harmonic signal, while rotating the polarization of the field incident on the sample by increments of 10° . The result is shown in Fig. 6.6. As can be seen in, the intensity of the fibrils changes versus the polarization angle [14, 13, 103]. Moreover, depending on the orientation of the fibrils with respect to the polarization angle, different part of the sample, corresponding to different tissues, will be pronounced.

6.5 Summary

In conclusion, second harmonic holographic microscopy has been performed with biological samples for the first time with an ultrashort Yb:KGW laser oscillator. The holograms were recorded with a CCD camera and numerically reconstructed with a

numerical Fresnel propagation kernel. Importantly, these images required pulse energies below 5 nJ, and using SHG obviates the need for external contrast markers. We observed no tissue damage or loss of image contrast, even after continued exposures. We used the microscope to image various samples including corn seeds, potato starch, and human muscle fibrils, including characterizations of the lateral and axial magnifications and resolutions. The resolution could be increased by the use of a more powerful collection objective, a higher-resolution camera, or by employing a more sophisticated reconstruction algorithm that includes aberration compensation. Higher speed 3D SHG image acquisition is possible by making use a a stronger reference wave to reduce CCD integration times.

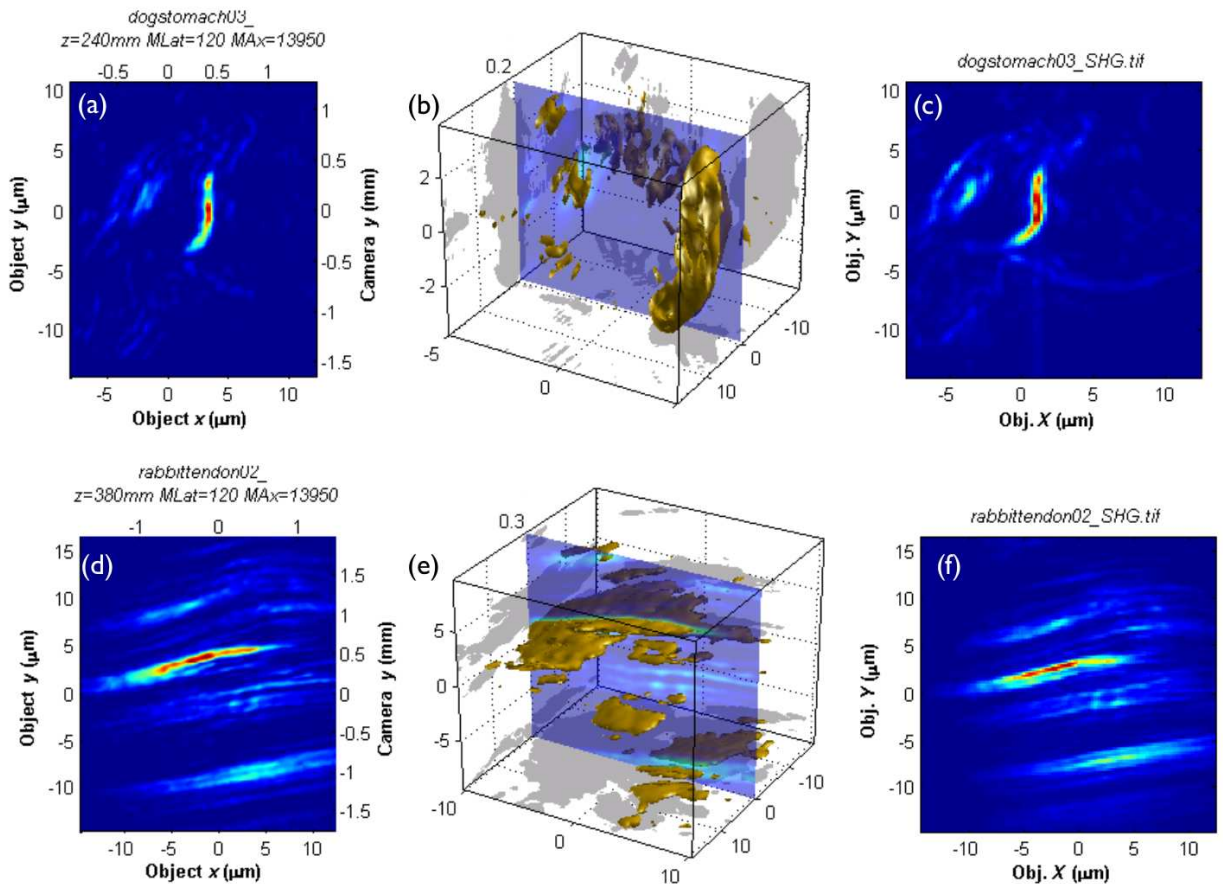


Figure 6.7: Dog stomache: Holographic a) reconstruction at the image plane, and b) around the focus. Also, the c) SHG image taken at focus is show. Rabbit tendon (c,d,e)

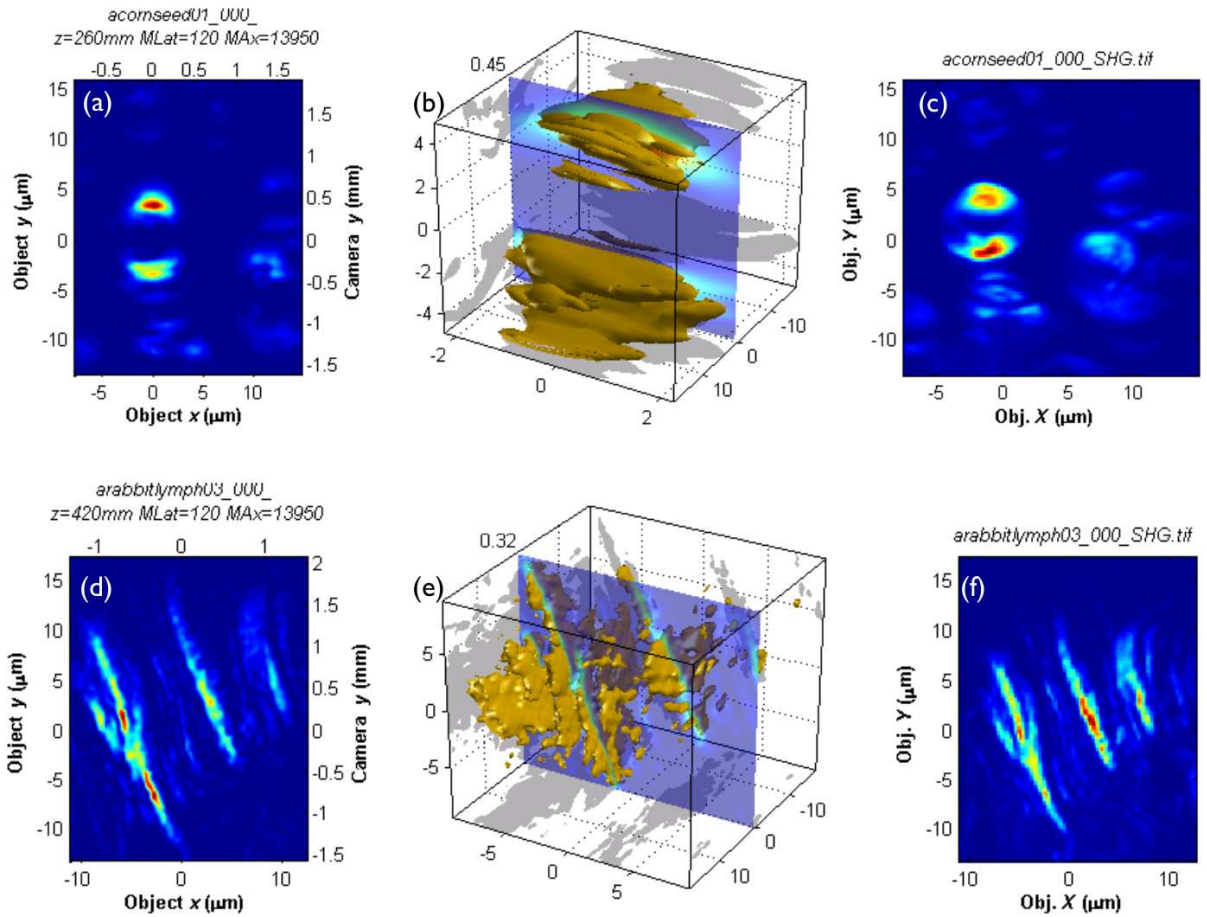


Figure 6.8: Corn seed: Holographic a) reconstruction at the image plane, and b) around the focus. Also, the c) SHG image taken at focus is show. Rabbit lymph (c,d,e).

Chapter 7

Conclusion

In conclusion, we have demonstrated a method for improved transverse spatial resolution in THG microscopy. This approach capitalizes on the polarization dependence of THG emission. In particular, THG emission is identically quenched in isotropic media for an incident circularly-polarized field. For non-isotropic media, THG emission is generally weak and strong THG suppression is maintained. This result was achieved by imaging a SLM into the plane of the sample, and applying a spatially-tailored $\frac{\pi}{2}$ phase difference between the two orthogonal polarization components. A transverse spatial resolution of up to 2 times is demonstrated. Future work in this technique would be investigating the theoretical limitations of polarization switched THG resolution enhancement, since deterministic control of the focal field polarization state distribution may provide a route to probing the anisotropic nonlinear response of nano-scale objects. Moreover, we would apply this technique to imaging of biological tissues. Moreover, we would further expand this technique to imaging of biological tissues.

We have also introduced a new technique based on coherent third harmonic generation microscopy, to characterize the spatially-varying polarization state distribution at the focal field in a nonlinear scanning laser microscope. We demonstrated a non-

iterative, in-situ phase retrieval algorithm, and measured polarization projection of THG images of a polystyrene bead. We determined the spatially-varying polarization states by locally probing the field through THG generated by an isotropic microsphere with a diameter much smaller than the focal field diameter. The tomography technique can be used to probe the focal field polarization state for a wide range of microscopy setups, and is applicable for obtaining polarization states and anisotropic responses from many types of linear and nonlinear optical microscopy.

Moreover, we showed 3-dimensional imaging through nonlinear SHG holographic microscopy. We obtained 3-dimensional images of an object by recording a 2-dimensional interference pattern between a second harmonic reference wave and second harmonic object wave of variety of biological specimen. In biological nonlinear imaging where the traditional method has largely been restricted to low image acquisition rates by using laser-scanning microscopy, nonlinear holographic microscopy could potentially be used to brake the barrier for faster imaging acquisition to map out the fast dynamics of the living tissues. In future, we would expand this method to THG holographic microscopy. Furthermore, by exploring the polarization dependence of the second harmonic signal from biological tissues, we would expand this method to revealing inner structures of biological samples. Moreover, we would pursue this method to enhance the speed in which the holograms are recorded by eliminating the readout artifacts observed, for example by introducing a fast mechanical shutter in front of the camera, and reconstructed, through using fast, inexpensive graphics cards. Furthermore, nonlinear holographic microscopy could be applied to capture the dynamics of living tissues.

Appendix A

Derivation of q^{th} Harmonics Generation under Focusing Conditions

In this appendix, I will drive the q^{th} harmonic generation, for a monochromatic wave under focusing conditions. First, we will transfer the wave equation from the spatial domain to the spatial frequency domain, reducing the problem to an inhomogenous linear ODE for each spatial frequency. Moreover, we will assume an un-depleted pump approximation.

A.1 The setup

We will start our derivation with the wave equation driven by a nonlinear polarization density. For the q^{th} harmonic, we end up with a differential equation describing the slowly-varying amplitude of given by

$$2ik_{z,q} \frac{\partial \mathbf{A}_q(x, y, z)}{\partial z} + \nabla_T^2 \mathbf{A}_q(x, y, z) = - \left(\frac{q\omega_1}{c} \right)^2 \chi^{(q)} \mathbf{A}_1^q(x, y, z) e^{i\Delta kz} \quad (\text{A.1})$$

where a solution of the form of $\mathbf{E}(x, y, z, t) = \mathbf{A}_q(x, y, z)e^{i(k_z z - \omega t)}$ has been substituted into the wave equation and the amplitude is assumed to be slowly varying with respect to λ along the z direction. Here, subscript 1 indicates the fundamental complex amplitude, while the superscript indicates the raised to the q^{th} power.

Note that in the paraxial approximation, $k_z \approx k$, which we will adopt in the remainder of this document. Also note that $\mathbf{A}_q(x, y, z)$ is a complex spatial envelope and that we are considering a monochromatic frequency.

Let us define a convention for Fourier transforms.

$$\mathbf{A}_q(x, y, z) = \iint_{-\infty-\infty}^{\infty, \infty} \hat{\mathbf{A}}_q(k_x, k_y, z) e^{i(k_x x + k_y y)} dk_x dk_y \quad (\text{A.2})$$

$$\hat{\mathbf{A}}_q(k_x, k_y, z) = \frac{1}{4\pi^2} \iint_{-\infty-\infty}^{\infty, \infty} \mathbf{A}_q(x, y, z) e^{-i(k_x x + k_y y)} dx dy \quad (\text{A.3})$$

Now, let's transform Eq. (A.1) into the spatial frequency domain. Taking the 2D Fourier transform yields:

$$\begin{aligned} & \left(2ik_q \frac{\partial}{\partial z} + \nabla_T^2 \right) \iint_{-\infty-\infty}^{\infty, \infty} \hat{\mathbf{A}}_q(k_x, k_y, z) e^{i(k_x x + k_y y)} dk_x dk_y = \\ & - \left(\frac{q\omega_1}{c} \right)^2 \chi^{(q)} \iint_{-\infty-\infty}^{\infty, \infty} \hat{\mathbf{A}}_1^q(k_x, k_y, z) e^{i(k_x x + k_y y)} e^{i\Delta k z} dk_x dk_y \end{aligned} \quad (\text{A.4})$$

Here, $\hat{\mathbf{A}}_1^q(k_x, k_y, z)$ represents the spatial frequency distribution of the fundamental spatial field raised to the q^{th} power

Now, we can write

$$\nabla_T^2 e^{i(k_x x + k_y y)} = (k_x^2 + k_y^2) e^{i(k_x x + k_y y)} \quad (\text{A.5})$$

so that Eq. (A.4) simplifies to a linear ODE for each spatial frequency given by

$$\left[2ik_q \frac{\partial}{\partial z} + (k_x^2 + k_y^2) \right] \hat{\mathbf{A}}_q(k_x, k_y; z) = - \left(\frac{q\omega_1}{c} \right)^2 \chi^{(q)} \hat{\mathbf{A}}_1^q(k_x, k_y, z) e^{i\Delta k z} \quad (\text{A.6})$$

In the undepleted pump approximation, the spatial frequency distribution for the driving term on the RHS of the equation above may be directly calculated.

A.1.1 The homogenous solution to Eq. (A.6)

The linear propagation of a field will be given by the homogeneous solution to Eq. (A.6). Let's calculate the situation for a Gaussian distribution. The homogeneous equation is written as

$$\frac{\partial \hat{\mathbf{A}}_q(k_x, k_y; z)}{\partial z} = -i \frac{(k_x^2 + k_y^2)}{2k_q} \hat{\mathbf{A}}_q(k_x, k_y; z) \quad (\text{A.7})$$

The solution to this equation may be written as

$$\hat{\mathbf{A}}_q(k_x, k_y; z) = \hat{\mathbf{A}}_q(k_x, k_y; 0) e^{-i \frac{(k_x^2 + k_y^2)}{2k_q} z} \quad (\text{A.8})$$

For a Gaussian beam with a waist w_{q0} and amplitude A_{q0} at $z = 0$, we have a spatial frequency distribution of

$$\hat{\mathbf{A}}_q(k_x, k_y; 0) = \frac{1}{4\pi^2} \iint_{-\infty-\infty}^{\infty\infty} A_{q0} e^{-\frac{x^2+y^2}{w_{q0}^2}} e^{-i(k_x x + k_y y)} dx dy \quad (\text{A.9})$$

Making use of the identity

$$\int e^{-Ax^2 - 2Bx} dx = \sqrt{\frac{\pi}{A}} e^{B^2/A}, \quad (\text{A.10})$$

the spatial frequency distribution of the Gaussian at the waist is given by

$$\begin{aligned}
\hat{\mathbf{A}}_q(k_x, k_y; 0) &= \frac{1}{4\pi^2} A_{q0} \left(\sqrt{\pi w_{q0}^2} e^{(ik_x)^2 w_{q0}^2/4} \right) \left(\sqrt{\pi w_{q0}^2} e^{(ik_y)^2 w_{q0}^2/4} \right) \\
&= A_{q0} \frac{w_{q0}^2}{4\pi} e^{-(k_x^2 + k_y^2) \frac{w_{q0}^2}{4}}
\end{aligned} \tag{A.11}$$

Now, the Gaussian may be written as

$$\hat{\mathbf{A}}_q(k_x, k_y; z) = A_{q0} \frac{w_{q0}^2}{4\pi} e^{-(k_x^2 + k_y^2) \left[\frac{w_{q0}^2}{4} + \frac{iz}{2k_q} \right]} \tag{A.12}$$

Transforming this back to the spatial domain gives

$$\mathbf{A}_q(x, y; z) = \iint_{-\infty-\infty}^{\infty\infty} A_{q0} \frac{w_{q0}^2}{4\pi} e^{-(k_x^2 + k_y^2) \frac{w_{q0}^2}{4} \left[1 + \frac{iz}{w_{q0}^2 k_q} \right]} e^{i(k_x x + k_y y)} dk_x dk_y \tag{A.13}$$

This gives a solution of

$$\begin{aligned}
\mathbf{A}_q(x, y; z) &= \frac{A_{q0}}{\left[1 + \frac{iz}{w_{q0}^2 k_q} \right]} \exp \left\{ -\frac{(x^2 + y^2)}{w_{q0}^2 \left[1 + \frac{iz}{w_{q0}^2 k_q} \right]} \right\} \\
&= \frac{A_{q0}}{(1 + i\zeta)} \exp \left\{ -\frac{(x^2 + y^2)}{w_{q0}^2 (1 + i\zeta)} \right\}
\end{aligned} \tag{A.14}$$

For simplicity, we will use the following substitution

$$B_q = 1 + \frac{2iz}{w_{q0}^2 k_q} \tag{A.15}$$

Leading to

$$\mathbf{A}_q(x, y; z) = \frac{A_{q0}}{B_q} \exp \left\{ -\frac{(x^2 + y^2)}{w_{q0}^2 B_q} \right\} \tag{A.16}$$

Before we move on with the rest of the derivation, some explanation of the above expression is in due. As expected, the homogenous solution to the propagation equation, for a Gaussian distribution is also Gaussian. Here, $\zeta = 2z/b$ is a dimensionless longitudinal coordinate defined in terms of the confocal parameter, $b = 2\pi w_{q0}^2/\lambda_q = k_q w_{q0}^2$, which is the measure of the longitudinal extent of the focal region of the gaussian beam. Figure. A.1, illustrate this quantity. The subscript q illustrate the order of harmonic of the initial gaussian beam. For example, if the homogenous wave equation was to be solved for the fundamental beam, $q = 1$, and Eq. A.14 can be written as,

$$\mathbf{A}_1(x, y; z) = \frac{A_{10}}{\left[1 + \frac{i2z}{w_{10}^2 k_1}\right]} \exp \left\{ -\frac{(x^2 + y^2)}{w_{10}^2 \left[1 + \frac{i2z}{w_{10}^2 k_1}\right]} \right\} \quad (\text{A.17})$$

$$= \frac{A_{10}}{B_1} \exp \left\{ -\frac{(x^2 + y^2)}{w_{10}^2 B_1} \right\} \quad (\text{A.18})$$

A.1.2 The driving term in the spatial frequency space.

Given the solution of a Gaussian for the paraxial wave equation presented in the previous section, we can readily compute the source term for an undepleted pump for q^{th} harmonic generation. In the spatial domain, the driving term is given by

$$-\left(\frac{q\omega_1}{c}\right)^2 \chi^{(q)} \mathbf{A}_1^q(x, y, z) = -\left(\frac{q\omega_1}{c}\right)^2 \chi^{(q)} \frac{A_{10}^q}{B_1^q} \exp \left\{ -q \frac{(x^2 + y^2)}{w_{10}^2 B_1} \right\} \quad (\text{A.19})$$

Transforming this to spatial frequency space gives

$$\frac{1}{4\pi^2} \left(-\left(\frac{q\omega_1}{c}\right)^2 \chi^{(q)} \frac{A_{10}^q}{B_1^q} \right) \iint_{-\infty-\infty}^{\infty\infty} \exp \left\{ -q \frac{(x^2 + y^2)}{w_{10}^2 B_1} \right\} e^{i(k_x x + k_y y)} dx dy \quad (\text{A.20})$$

This simplifies to

$$\frac{-q^2\omega_1^2\chi^{(q)}A_{10}^q}{4\pi^2 \cdot c^2B_1^q} \left(\frac{\pi}{q}w_{10}^2B_1 \right) \exp \left\{ -(k_x^2 + k_y^2) \frac{w_{10}^2B_1}{4q} \right\} \quad (\text{A.21})$$

and is written compactly as

$$\frac{-q\omega_1^2\chi^{(q)}A_{10}^qw_{10}^2}{4\pi c^2B_1^{q-1}} e^{-(k_x^2+k_y^2)\frac{w_{10}^2B_1}{4q}} \quad (\text{A.22})$$

A.1.3 Inhomogeneous spatial frequency domain equation

Taking the Fourier space expression for the un-depleted term of a focused Gaussian and inserting it into Eq. (A.6), we obtain

$$\left[2ik_q \frac{\partial}{\partial z} - (k_x^2 + k_y^2) \right] \hat{\mathbf{A}}_q(k_x, k_y; z) = \frac{-q\omega_1^2\chi^{(q)}A_{10}^qw_{10}^2}{4\pi c^2B_1^{q-1}} e^{-(k_x^2+k_y^2)\frac{w_{10}^2B_1}{4q}} e^{i\Delta kz} \quad (\text{A.23})$$

Finally, we have the equation that we wish to solve

$$\frac{\partial \hat{\mathbf{A}}_q}{\partial z} = -i \frac{(k_x^2 + k_y^2)}{2k_q} \hat{\mathbf{A}}_q + i \frac{\omega_1\chi^{(q)}A_{10}^qw_{10}^2}{8\pi n_q c B_1^{q-1}} e^{-(k_x^2+k_y^2)\frac{w_{10}^2B_1}{4q}} e^{i\Delta kz} \quad (\text{A.24})$$

Where we have made use of

$$\frac{1}{k_q} = \frac{c}{n_q w_q} = \frac{c}{n_q q w_1}$$

A.2 Solutions in the spatial frequency domain

Let us assume that we have no injected control q^{th} harmonic field and that the solution of the field takes the form of a Gaussian given in Eq. (A.12).

$$\hat{\mathbf{A}}_q(k_x, k_y; z) = \mathbf{A}_{q0}(z) \frac{w_{q0}^2}{4\pi} e^{-(k_x^2+k_y^2)\frac{w_{q0}^2A_q}{4}} \quad (\text{A.25})$$

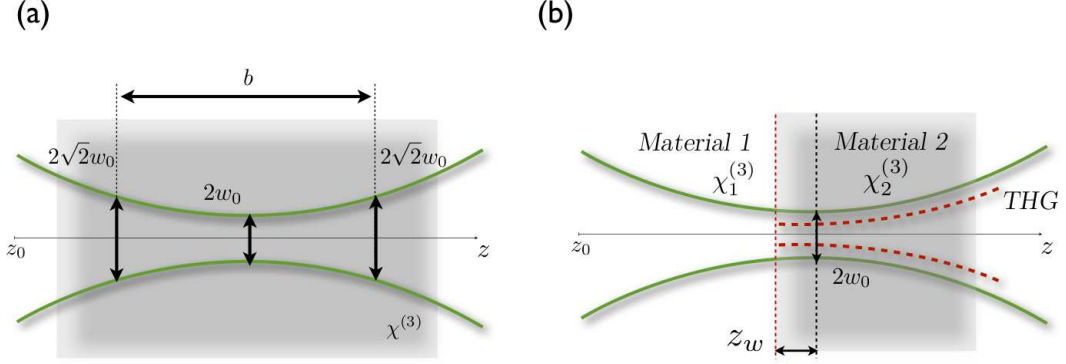


Figure A.1: Geometry of a Gaussian beam focused (a) inside a bulk material and (b) on an interface of two material with different third order susceptibilities.

Taking the partial with respect to z gives

$$\frac{\partial \hat{\mathbf{A}}_q(k_x, k_y; z)}{\partial z} = \frac{-i(k_x^2 + k_y^2)}{2k_q} \hat{\mathbf{A}}_q(k_x, k_y; z) + \frac{w_{q0}^2}{4\pi} e^{-(k_x^2 + k_y^2) \frac{w_{q0}^2 B_q}{4}} \frac{\partial \mathbf{A}_{q0}(z)}{\partial z} \quad (\text{A.26})$$

Inserting this into Eq. (A.24) gives,

$$\frac{w_{q0}^2}{4\pi} e^{-(k_x^2 + k_y^2) \frac{w_{q0}^2 B_q}{4}} \frac{\partial \mathbf{A}_{q0}(z)}{\partial z} = i \frac{\omega_1 \chi^{(q)} A_{10}^q w_{10}^2}{8\pi n_q c B_1^{q-1}} e^{-(k_x^2 + k_y^2) \frac{w_{10}^2 B_1}{4q}} e^{i\Delta k z} \quad (\text{A.27})$$

Rearranging

$$\frac{\partial \mathbf{A}_{q0}(z)}{\partial z} = i \left(\frac{w_{10}}{w_{q0}} \right)^2 \frac{\omega_1 \chi^{(q)} A_{10}^q}{2n_q c B_1^{q-1}} e^{-(k_x^2 + k_y^2)} \left\{ \left[\frac{w_{10}^2}{4q} + \frac{iz}{2qk_1} \right] - \left[\frac{w_{q0}^2}{4} + \frac{iz}{2k_q} \right] \right\} e^{i\Delta k z} \quad (\text{A.28})$$

From which we have a solution

$$\mathbf{A}_{q0}(z) = i \left(\frac{w_{10}}{w_{q0}} \right)^2 \frac{\omega_1 \chi^{(q)} A_{10}^q}{2n_q c} \int_{z_0}^z \frac{e^{-(k_x^2 + k_y^2) \left\{ \left[\frac{w_{10}^2}{4q} + \frac{iz'}{2qk_1} \right] - \left[\frac{w_{q0}^2}{4} + \frac{iz'}{2k_q} \right] \right\}} e^{i\Delta k z'}}{B_1^{q-1}} dz' \quad (\text{A.29})$$

For small Δk , we can make the assumptions,

$$\left[\frac{w_{10}^2}{4q} + \frac{iz'}{2qk_1} \right] = \left[\frac{w_{q0}^2}{4} + \frac{iz'}{2k_q} \right] \quad (\text{A.30})$$

Or, equivalently

$$w_{10}^2 = qw_{q0}^2 \quad (\text{A.31})$$

$$qk_1 = k_q \quad (\text{A.32})$$

Which gives us,

$$\mathbf{A}_{q0}(z) = iq \frac{\omega_1 \chi^{(q)} A_{10}^q}{2n_q c} \int_{z_0}^z \frac{e^{i\Delta k z'}}{\left[1 + \frac{i2z}{w_{10}^2 k_1} \right]^{q-1}} dz' \quad (\text{A.33})$$

or equivalently,

$$\mathbf{A}_{q0}(z) = iq \frac{\omega_1 \chi^{(q)} A_{10}^q}{2n_q c} J_q(\Delta k; z_0; z) \quad (\text{A.34})$$

where,

$$J_q(\Delta k; z_0; z) = b \int_{z_0/b}^{z/b} \frac{e^{i\Delta k b z'}}{(1 + i2z')^{q-1}} dz' \quad (\text{A.35})$$

is the q^{th} harmonic interaction length and z_0 is the position of the entrance of the medium, and $z = 0$ represents the waist of the beam.

A.2.1 Limiting case of infinite uniform nonlinear media

When we consider the q^{th} harmonic power in the case of an infinite, uniform nonlinear medium, the integral can be solved analytically through contour integration.

$$J = b \int_{-\infty}^{\infty} \frac{e^{i\Delta k b z'}}{(1 + 2iz')^{q-1}} dz' \quad (\text{A.36})$$

To evaluate the integral, we first find the poles of the integrand to be $z'_0 = \frac{i}{2}$. Moreover, with a negative mismatch ($\Delta k < 0$), the contour encloses the lower-half plane (LHP). Since the pole will always be located on the positive imaginary axis, namely upper half plane (UHP), for any q^{th} order power, the value of this integral will be 0.

With a positive mismatch, the contour will enclose the UHP and the pole of order $m = q - 1$. The circular portion of the integration goes to zero by virtue of the exponential taking on an infinite negative argument, thus the integration over the real line portion will just be $2\pi i$ times the residue.

The residue of an m^{th} order pole is given by

$$\begin{aligned}
Res &= \frac{1}{(m-1)!} \frac{\partial^{m-1}}{\partial z^{m-1}} \left[(z - z'_0)^m f(z) \right] \Big|_{z=\frac{-i}{2}} \\
&= \frac{1}{(m-1)!} \frac{\partial^{m-1}}{\partial z^{m-1}} \left[\left(z - \frac{i}{2} \right)^m \frac{e^{i\Delta kbz'}}{(1 + 2iz')^m} \right] \Big|_{z=\frac{-i}{2}} \\
&= \frac{1}{(m-1)!} \left(-\frac{i}{2} \right)^m \frac{\partial^{m-1}}{\partial z^{m-1}} e^{i\Delta kbz'} \Big|_{z=\frac{-i}{2}} \\
&= \frac{1}{(q-2)!} \left(-\frac{i}{2} \right)^{q-1} \frac{\partial^{q-2}}{\partial z^{q-2}} e^{i\Delta kbz'} \Big|_{z=\frac{-i}{2}} \\
&= \frac{1}{(q-2)!} \left(-\frac{i}{2} \right)^{q-1} (\Delta kb)^{q-2} e^{-\Delta kb/2}
\end{aligned} \tag{A.37}$$

Then,

$$\begin{aligned}
J &= b \int_{-\infty}^{\infty} \frac{e^{i\Delta kbz'}}{(1 + 2iz')^{q-1}} dz' \\
&= 2\pi i \frac{b}{(q-2)!} \left(-\frac{i}{2} \right)^{q-1} (\Delta kb)^{q-2} e^{-\Delta kb/2} \\
&= 2\pi \frac{1}{(q-2)!} \frac{b}{2} \left(\frac{\Delta kb}{2} \right)^{q-2} e^{-\Delta kb/2}
\end{aligned} \tag{A.38}$$

Thus, for $\Delta k > 0$,

$$J = \frac{\pi b}{(q-2)!} \left(\frac{\Delta kb}{2} \right)^{q-2} e^{-\Delta kb/2} \tag{A.39}$$

Compactly written,

$$J_q(\Delta k; z_0; z) = \begin{cases} 0 & \text{for } \Delta k < 0 \\ \frac{\pi b}{(q-2)!} \left(\frac{\Delta kb}{2}\right)^{q-2} e^{-\Delta kb/2} & \text{for } \Delta k > 0 \end{cases} \quad (\text{A.40})$$

A.2.2 Limiting case of non-uniform nonlinear media

If we consider the susceptibility to not be uniform across the sample, we can no longer remove it from the integral as was done in the previous section. For example, consider the case of two semi-infinite homogeneous samples brought in contact with identical refractive indices but differing uniform susceptibilities $\chi_1^{(3)}$ and $\chi_2^{(3)}$ at an interface located z_w (which maps onto $z_r = \frac{z_w}{b}$ in our normalized coordinates) beyond the beam waist (*cf* A.1).

$$J = \int_{-\infty}^{z_r} \frac{\chi_1 e^{i\Delta kbz'}}{(1+2iz')^2} dz' + \int_{z_r}^{\infty} \frac{\chi_2 e^{i\Delta kbz'}}{(1+2iz')^2} dz' \quad (\text{A.41})$$

If we bring in a variable $\delta\chi = \chi_1 - \chi_2$ and use the the assumption that $\Delta kb \ll 1$, we can write

$$J = \int_{-\infty}^{\infty} \frac{\chi_1}{(1+2iz')^2} dz' - \int_{z_r}^{\infty} \frac{\delta\chi}{(1+2iz')^2} dz' \quad (\text{A.42})$$

The first integral can be done using a quick substitution, and is equal to 0. On a special note, this would be the same result as if we had chosen Δk to be 0. The second integral will also be done using a substitution and is shown below.

$$\begin{aligned}
J &\approx - \int_{z_r}^{\infty} \frac{\delta\chi}{(1+2iz')^2} dz' \\
&\approx - \int_{y_1}^{y_2} \frac{-i\delta\chi}{2y^2} dy \\
&\approx \lim_{g \rightarrow \infty} \frac{-i\delta\chi}{2(1+2iz)} \Big|_{z_r}^g \\
&\approx \lim_{g \rightarrow \infty} \frac{-i\delta\chi}{2} \left(\frac{1}{1+2ig} - \frac{1}{1+2iz_r} \right) \\
&\approx \lim_{g \rightarrow \infty} \delta\chi \left(\frac{\frac{z_r}{g} - 1}{\frac{1}{g} - 4z_r + 2i(1 + \frac{z_r}{g})} \right) \\
&\approx -\delta\chi \left(\frac{1}{-4z_r + 2i} \right)
\end{aligned} \tag{A.43}$$

Thus, the collected third harmonic intensity $I_3 = \frac{1}{2}\epsilon_0 cn_3 E_3 E_3^* \propto |J|^2$, and the collected power with a CCD for example will be,

$$P_3 \propto \frac{\delta\chi^2}{(1 + \frac{4z_r^2}{b^2})} \tag{A.44}$$

Which states that the THG is proportional to the square of the difference between the between the third order susceptibilities.

Bibliography

- [1] D. Gabor, “A new microscopic principle,” *Nature* **161**(4098), 777–778 (1948).
- [2] E. N. Leith and J. Upatniek, “Microscopy by wavefront reconstruction,” *J Opt Soc Am* **55**(8), 981–986 (1965).
- [3] E. Leith and J. Upatniek, “Reconstructed wavefront and communication theory,” *J Opt Soc Am* **52**(10), 1123–1130 (1962).
- [4] U. Schnars and W. Juptner, “Digital recording and numerical reconstruction of holograms,” *Meas. Sci. Technol.* **13**(9), 85–101 (2002).
- [5] F. Palacios, J. Ricardo, D. Palacios, E. Goncalves, J. L. Valin, and R. D. Souza, “3D image reconstruction of transparent microscopic objects using digital holography,” *Opt Comm* **248**(13), 41–50 (2005).
- [6] U. Jüptner, “Direct recording of holograms by a CCD target and numerical reconstruction,” *Appl. Opt* **33**(2), 179–181 (1994).
- [7] E. Cucho, P. Marquet, and C. Depeursinge, “Simultaneous amplitude-contrast and quantitative phase-contrast microscopy by numerical reconstruction of Fresnel off-axis holograms,” *Appl Opt* **38**(34), 6994–7001 (1999).
- [8] T. Wilson, *Confocal microscopy* (Academic Press, London, 1990).
- [9] T. Wilson and J. R. Sheppard, *Theory and practice of scanning optical microscopy* (Academic Press, London, 1984).
- [10] F. Helmchen and W. Denk, “Deep tissue two-photon microscopy,” *Nat meth* **2**(12), 932–940 (2005).
- [11] W. Denk, J. H. Strickler, and W. W. Webb, “2-photon laser scanning fluorescence microscopy,” *Science* **248**(4951), 73–76 (1990).
- [12] L. V. Wang, *Biomed Opt* (Wiley, 2007).
- [13] I. Freund, M. Deutsch, and A. Sprecher, “Connective-tissue polarity-optical 2nd harmonic microscopy, crossed-beam summation, and small-angle scattering in rat-tail tendon,” *Biophys J* **50**(4), 693–712 (1986).

- [14] S. Roth and I. Freund, “Coherent optical harmonic-generation in rat-tail tendon,” *Opt Commun* **33**(3), 292–296 (1980).
- [15] Y. Barad, H. Eisenberg, M. Horowitz, and Y. Silberberg, “Nonlinear scanning laser microscopy by third harmonic generation,” *Appl. Phys. Lett.* **70**(8), 922–924 (1997).
- [16] J. A. Squier, M. Müller, G. J. Brakenhoff, and ken R Wilson, “Third harmonic generation microscopy,” *Opt Exp* **3**(9), 315–324 (1998).
- [17] M. D. Duncan, “Molecular discrimination and contrast enhancement using a scanning coherent anti-Stokes Raman microscope,” *Opt comm* **50**(5), 307–312 (1984).
- [18] M. D. Duncan, J. Reintjes, and T. Manuccia, “Scanning coherent anti-stokes Raman microscope,” *Opt Lett* **7**(8), 350–352 (1982).
- [19] S. V. Plotnikov, A. C. Millard, P. J. Campagnola, and W. A. Mohler, “Characterization of the myosin-based source for second-harmonic generation from muscle sarcomeres,” *Biophys J* **90**(2), 693–703 (2006).
- [20] S. W. Chu, S. Y. Chen, G. W. Chern, T. H. Tsai, Y. C. Chen, B. L. Lin, and C. K. Sun, “Studies of $\chi^{(2)}/\chi^{(3)}$ tensors in submicron-scaled bio-tissues by polarization harmonics optical microscopy,” *Biophys J* **86**(6), 3914–3922 (2004).
- [21] R. Williams, W. Zipfel, and W. Webb, “Interpreting second-harmonic generation images of collagen I fibrils,” *Biophys J* **88**, 1377–1386 (2005).
- [22] P. J. Campagnola, M. D. Wei, A. Lewis, and L. M. Loew, “High-resolution nonlinear optical imaging of live cells by second harmonic generation,” *Biophysical Journal* **77**(6), 3341–3349 (1999).
- [23] L. Moreaux, O. Sandre, and S. Charpak, “Coherent scattering in multi-harmonic light microscopy,” *Biophys J* **80**, 1568–1574 (2001).
- [24] P. J. Campagnola and L. M. Loew, “Second-harmonic imaging microscopy for visualizing biomolecular arrays in cells, tissues and organisms,” *Nat Biotechnol* **21**(11), 1356–1360 (2003).
- [25] J. Y. Huang, A. Lewis, and L. Loew, “Nonlinear optical-properties of potential sensitive styryl dyes,” *Biophys J* **53**(5), 665–670 (1988).
- [26] A. T. Yeh, N. Nassif, A. Zoumi, and B. J. Tromberg, “Selective corneal imaging using combined second-harmonic generation and two-photon excited fluorescence,” *Opt Lett* **27**(23), 2082–2084 (2002).
- [27] G. Cox, E. Kable, A. Jones, I. Fraser, and F. Manconi, “3-dimensional imaging of collagen using second harmonic generation,” *J Struct Bio* **141**, 53–62 (2003).

- [28] W. Mohler, A. C. Millard, and P. J. Campagnola, “Second harmonic generation imaging of endogenous structural proteins,” *Methods* **29**(1), 97–109 (2003).
- [29] C. K. Sun, S. W. Chu, S. Y. Chen, T. H. Tsai, T. M. Liu, C. Y. Lin, and H. J. Tsai, “Higher harmonic generation microscopy for developmental biology,” *J Struct Biol* **147**(1), 19–30 (2004).
- [30] J. F. Ward and G. H. C. New, “Optical third harmonic generation in gases by a focused laser beam,” *Phys Rev* **185**(1), 57 (1969).
- [31] R. W. Boyd, *Nonlinear optics*, 3rd ed. (Academic Press, 2008).
- [32] M. Müller, J. Squier, K. R. Wilson, and G. J. Brakenhoff, “3D microscopy of transparent objects using third-harmonic generation,” *J Microsc-Oxford* **191**, 266–274 (1998).
- [33] A. Lago, G. Hilber, and R. Wallenstein, “Optical-frequency conversion in gaseous media,” *Phys Rev A* **36**(8), 3827–3836 (1987).
- [34] R. Dorn, S. Quabis, and G. Leuchs, “Sharper focus for a radially polarized light beam,” *Phys Rev Lett* **91**(23), 233,901 (2003).
- [35] O. Masihzadeh, P. Schlup, and R. A. Bartels, “Enhanced spatial resolution in third-harmonic microscopy through polarization switching,” *Optics Letters* **34**(8), 1240–1242 (2009).
- [36] B. J. Davis and P. S. Carney, “Robust determination of the anisotropic polarizability of nanoparticles using coherent confocal microscopy,” *J Opt Soc Am A* **25**(8), 2102–2113 (2008).
- [37] M. Antkowiak, N. Callens, C. Yourassowsky, and F. Dubois, “Extended focused imaging of a microparticle field with digital holographic microscopy,” *Opt Lett* **33**(14), 1626–1628 (2008).
- [38] Y. Otsu, V. Bormuth, J. Wong, B. Mathieu, G. P. Dugué, A. Feltz, and S. Dieudonné, “Optical monitoring of neuronal activity at high frame rate with a digital random-access multiphoton (RAMP) microscope,” *J Neurosci Meth* **173**(2), 259–270 (2008).
- [39] M. S. Amin, Y. K. Park, N. Lue, R. R. Dasari, K. Badizadegan, M. S. Feld, and G. Popescu, “Microrheology of red blood cell membranes using dynamic scattering microscopy,” *Opt Express* **15**(25), 17,001–17,009 (2007).
- [40] W. Choi, C. Fang-Yen, K. Badizadegan, and S. Oh, “Tomographic phase microscopy,” *Nat meth* **4**(9), 717–719 (2007).
- [41] N. Lue, W. Choi, G. Popescu, and T. Ikeda, “Quantitative phase imaging of live cells using fast Fourier phase microscopy,” *App Opt* **46**(10), 1836–1842 (2007).

- [42] V. Crepel, D. Aronov, I. Jorquera, A. Represa, Y. Ben-Ari, and R. Cossart, “A parturition-associated nonsynaptic coherent activity pattern in the developing hippocampus,” *Neuron* **54**(1), 105–120 (2007).
- [43] O. Garaschuk, R. Milos, C. Grienberger, N. Marandi, H. Adelsberger, and A. Konnerth, “Optical monitoring of brain function in vivo: from neurons to networks,” *Pflug Arch Eur J Phy* **453**(3), 385–396 (2006).
- [44] S.-P. Tai, Y. Wu, D.-B. Shieh, L.-J. Chen, K.-J. Lin, C.-H. Yu, S.-W. Chu, C.-H. Chang, X.-Y. Shi, Y.-C. Wen, K.-H. Lin, T.-M. Liu, and C.-K. Sun, “Molecular imaging of cancer cells using plasmon-resonant-enhanced third-harmonic-generation in silver nanoparticles,” *Adv Mater* **19**(24), 4520 (2007).
- [45] P. Schoen, M. Behrndt, D. Ait-Belkacem, H. Rigneault, and S. Brasselet, “Polarization and phase pulse shaping applied to structural contrast in nonlinear microscopy imaging,” *Phys Rev A* **81**(1), 013,809 (2010).
- [46] C. P. Pfeffer, B. R. Olsen, F. Ganikhanov, and F. Legare, “Multimodal nonlinear optical imaging of collagen arrays,” *J Struct Biol* **164**(1), 140–145 (2008).
- [47] H. Chen, H. Wang, M. N. Slipchenko, Y. Jung, Y. Shi, J. Zhu, K. K. Buhman, and J.-X. Cheng, “A multimodal platform for nonlinear optical microscopy and microspectroscopy,” *Optics Express* **17**(3), 1282–1290 (2009).
- [48] P. Xu, X. Li, V. Chigrinov, and S. Studentsov, “Fast and high-contrast liquid-crystal shutters with low power consumption based on an optical-mode-interference cell,” *Appl Optics* **45**(17), 4020–4025 (2006).
- [49] N. Spagnolo, C. Vitelli, S. Giacomini, F. Sciarrino, and F. D. Martini, “Polarization preserving ultra fast optical shutter for quantum information processing,” *optics express* **16**(22), 17,609–17,615 (2008).
- [50] Y. Pu, M. Centurion, and D. Psaltis, “Harmonic holography: a new holographic principle,” *Appl Optics* **47**(4), A103–A110 (2008).
- [51] P. Klopp, V. Petrov, U. Griebner, and G. Erbert, “Passively mode-locked Yb : KYW laser pumped by a tapered diode laser,” *optics express* **10**(2), 108–113 (2002).
- [52] S. A. Meyer, J. A. Squier, and S. A. Diddams, “Diode-pumped Yb : KYW femtosecond laser frequency comb with stabilized carrier-envelope offset frequency,” *Eur Phys J D* **48**(1), 19–26 (2008).
- [53] F. Hoos, T. P. Meyrath, S. Li, B. Braun, and H. Giessen, “Femtosecond 5-W Yb:KGW slab laser oscillator pumped by a single broad-area diode and its application as supercontinuum source,” *Appl Phys B-Lasers O* **96**, 5–10 (2009).
- [54] D. Yelin and Y. Silberberg, “Laser scanning third-harmonic-generation microscopy in biology,” *optics express* **5**(8), 169–175 (1999).

- [55] S. Hell and J. Wichmann, “Breaking the diffraction resolution limit by stimulated emission: stimulated-emission-depletion fluorescence microscopy,” *Opt Lett* **19**(11), 780–782 (1994).
- [56] E. Betzig, G. H. Patterson, R. Sougrat, O. W. Lindwasser, S. Olenych, J. S. Bonifacino, M. W. Davidson, J. Lippincott-Schwartz, and H. F. Hess, “Imaging intracellular fluorescent proteins at nanometer resolution,” *Science* **313**(5793), 1642–1645 (2006).
- [57] M. Gustafsson, “Nonlinear structured-illumination microscopy: Wide-field fluorescence imaging with theoretically unlimited resolution,” *P Natl Acad Sci Usa* **102**(37), 13,081–13,086 (2005).
- [58] M. Hofmann, C. Eggeling, S. Jakobs, and S. Hell, “Breaking the diffraction barrier in fluorescence microscopy at low light intensities by using reversibly photoswitchable proteins,” *P Natl Acad Sci Usa* **102**(49), 17,565–17,569 (2005).
- [59] Q. T. Nguyen, N. Callamaras, C. Hsieh, and I. Parker, “Construction of a two-photon microscope for video-rate Ca²⁺ imaging,” *Cell Calcium* **30**(6), 383–393 (2001).
- [60] G. Y. Fan, H. Fujisaki, A. Miyawaki, R. K. Tsay, R. Y. Tsien, and M. H. Ellisman, “Video-rate scanning two-photon excitation fluorescence microscopy and ratio imaging with cameleons,” *Biophys J* **76**(5), 2412–2420 (1999).
- [61] T. H. Maiman, “Stimulated optical radiation in ruby,” *Nature* **187**(4736), 493–494 (1960).
- [62] A. E. Franken, C. Hill, W. Peters, and G. Weinreich, “Generation of optical harmonics,” *Phys Rev Lett* **7**(4), 118–120 (1961).
- [63] Y. R. Shen, *The principle of nonlinear optics* (Wiley, 1984).
- [64] R. W. Hellwarth, J. cherlow, and T. T. Yang, “Origin and frequency dependence of nonlinear optical susceptibilities of glasses,” *Phys Rev B* **11**, 964–967 (1975).
- [65] J. N. Gannaway and C. J. R. Sheppard, “Second-harmonic imaging in the scanning optical microscope,” *Opt Quant Elect* **10**, 435–439 (1978).
- [66] G. T. Boyd, Y. R. Shen, and T. W. Hansch, “Continuous-wave 2nd-harmonic generation as a surface microprobe,” *Opt Lett* **11**(2), 97–99 (1986).
- [67] I. H. Chen, S. W. Chu, F. Bresson, M. C. Tien, J. W. Shi, and C. K. Sun, “Three-dimensional electric field visualization utilizing electric-field-induced second-harmonic generation in nematic liquid crystals,” *Opt Lett* **28**(15), 1338–1340 (2003).

- [68] C. K. Sun, S. W. Chu, S. P. Tai, S. Keller, A. Abare, U. K. Mishra, and S. P. DenBaars, “Mapping piezoelectric-field distribution in gallium nitride with scanning second-harmonic generation microscopy,” *Scanning* **23**(2), 182192 (2001).
- [69] L. Moreaux, O. Sandre, and J. Mertz, “Membrane imaging by second-harmonic generation microscopy,” *J Opt Soc Am B* **17**(10), 1685–1694 (2000).
- [70] M. Han, G. Giese, and J. F. Bille, “Second harmonic generation imaging of collagen fibrils in cornea and sclera,” *Opt Exp* **13**(15), 5791–5797 (2005).
- [71] P. Stoller, K. M. Reiser, P. M. Celliers, and A. M. Rubenchik, “Polarization-modulated second harmonic generation in collagen,” *Biophys J* **82**(6), 3330–3342 (2002).
- [72] S. J. Lin, S. H. Jee, C. J. Kuo, R. J. Wu, W. C. Lin, J. S. Chen, Y. H. Liao, C. J. Hsu, T. F. Tsai, Y. F. Chen, and C. Y. Dong, “Discrimination of basal cell carcinoma from normal dermal stroma by quantitative multiphoton imaging,” *Opt Lett* **31**(18), 2756–2758 (2006).
- [73] P. P. Bey, J. F. Giuliani, and H. Rabin, “Linear and circular polarized laser radiation in optical third harmonic generation,” *Phys. Lett. A* **26**(3), 128 (1968).
- [74] J. M. Schins, T. Schrama, J. A. Squier, G. J. Brakenhoff, and M. Müller, “Determination of material properties by use of third-harmonic generation microscopy,” *J Opt Soc Am B* **19**(7), 1627–1634 (2002).
- [75] T. Y. F. Tsang, “Optical 3rd-harmonic generation at interfaces,” *Phys Rev A* **52**(5), 4116–4125 (1995).
- [76] M. Kolesik and J. V. Moloney, “Nonlinear optical pulse propagation simulation: From Maxwell’s to unidirectional equations,” *Phys Rev E* **70**(3), 036,604 (2004).
- [77] D. Jackson, *Classical electrodynamics*, 3rd ed. (Wiley, 2002).
- [78] L. Novotny and B. Hecht, *Principles of nano-optics*, 1st ed. (Cambridge University Press, 2007).
- [79] A. A. Asatryan, C. J. R. Sheppard, and C. M. de Sterke, “Vector treatment of second-harmonic generation produced by tightly focused vignetted Gaussian beams,” *J Opt Soc Am B* **21**(12), 2206–2212 (2004).
- [80] J. X. Cheng, A. Volkmer, and X. S. Xie, “Theoretical and experimental characterization of coherent anti-Stokes Raman scattering microscopy,” *J Opt Soc Am B* **19**(6), 1363–1375 (2002).
- [81] J. X. Cheng and X. S. Xie, “Green’s function formulation for third-harmonic generation microscopy,” *J Opt Soc Am B* **19**(7), 1604–1610 (2002).

- [82] F. Helmchen and W. Denk, “New developments in multiphoton microscopy,” *Current opinion in neurobiology* (2002).
- [83] R. Gauderon, P. B. Lukins, and C. J. R. Sheppard, “Three-dimensional second-harmonic generation imaging with femtosecond laser pulses,” *Opt Lett* **23**(15), 1209–1211 (1998).
- [84] A. Zumbusch, G. Holtom, and X. Xie, “Three-dimensional vibrational imaging by coherent anti-Stokes Raman scattering,” *Phys Rev Lett.* **82**(20), 4142–4145 (1999).
- [85] V. Tuchin, *Tissue optics* (SPIE Press, 2000).
- [86] J. A. Squier and M. Müller, “High resolution nonlinear microscopy: A review of sources and methods for achieving optimal imaging,” *Rev Sci Inst* **72**(7), 2855–2867 (2001).
- [87] D. R. Sandison and W. W. Webb, “Background rejection and signal-to-noise optimization in confocal and alternative fluorescence microscopes,” *Appl Opt* **33**(4), 603–615 (1994).
- [88] M. Born and E. Wolf, *Principles of Optics* (McGraw-Hill, 1968).
- [89] J. W. Goodman, *Introduction to Fourier optics* (McGraw -Hill, 1996).
- [90] R. D. Frostig, *In vivo optical imaging of brain function* (CRC Press, 2002).
- [91] J. A. Squier, M. Müller, and V. Barzda, *Ultrafast optics* (www.physics.gatech.edu/gcuo/ultratext.html, 2008).
- [92] K. Bahlmann, P. T. C. So, M. Kirber, R. Reich, B. Kosicki, W. McGonagle, and K. Bellve, “Multifocal multiphoton microscopy (MMM) at a frame rate beyond 600 Hz,” *Opt Exp* **15**(17), 10,998–11,005 (2002).
- [93] V. Andresen, A. Egner, and S. W. Hell, “Time-multiplexed multifocal multiphoton microscope,” *Opt Lett* **26**(2), 75–77 (2001).
- [94] Y. P. Tan, I. Llano, A. Hopt, F. Wurriehausen, and E. Neher, “Fast scanning and efficient photodetection in a simple two-photon microscope,” *J Neurosci Meth* **92**(1-2), 123–135 (1999).
- [95] A. Hopt and E. Neher, “Highly nonlinear photodamage in two-photon fluorescence microscopy,” *Biophys J* **80**(4), 2029–2036 (2001).
- [96] K. E. Sheetz and J. A. Squier, “Ultrafast optics: Imaging and manipulating biological systems,” *J Appl Phys* **105**(5), 051,101 (2009).
- [97] C. Sheppard, J. Gannaway, R. Kompfner, and D. Walsh, “Scanning harmonic optical microscope,” *Ieee J Quant Elect* **13**(9), D100–D100 (1977).

- [98] J. Gannaway and C. Sheppard, “Second-harmonic imaging in the scanning optical microscope,” *Opt Quant Elect* (1978).
- [99] E. Y. S. Yew and C. J. R. Sheppard, “Effects of axial field components on second harmonic generation microscopy,” *Opt Exp* **14**(3), 1167–1174 (2006).
- [100] J. Mertz and L. Moreaux, “Second-harmonic generation by focused excitation of inhomogeneously distributed scatterers,” *Opt Comm* **196**(1-6), 325–330 (2001).
- [101] F. Legare, C. Pfeffer, and B. R. Olsen, “The role of backscattering in SHG tissue imaging,” *Biophys J* **93**(4), 1312–1320 (2007).
- [102] C. P. Pfeffer, B. R. Olsen, and F. Legare, “Second harmonic generation imaging of fascia within thick tissue block,” *Opt Exp* **15**(12), 7296–7302 (2007).
- [103] F. Tiaho, G. Recher, and D. Rouede, “Estimation of helical angles of myosin and collagen by second harmonic generation imaging microscopy,” *Opt Exp* **15**(19), 12,286–12,295 (2007).
- [104] A. F. Abouraddy and K. C. Toussaint, “Three-dimensional polarization control in microscopy,” *Phys Rev Lett* **96**(15), 153,901 (2006).
- [105] M. R. Beversluis, L. Novotny, and S. J. Stranick, “Programmable vector point-spread function engineering,” *Opt Exp* **14**(7), 2650–2656 (2006).
- [106] I. Iglesias and B. Vohnsen, “Polarization structuring for focal volume shaping in high-resolution microscopy,” *Opt Commun* **271**(1), 40–47 (2007).
- [107] H. P. Urbach and S. F. Pereira, “Field in focus with a maximum longitudinal electric component,” *Phys Rev Lett* **100**(12), 123,904 (2008).
- [108] K. Yoshiki, M. Hashimoto, and T. Araki, “Second-harmonic-generation microscopy using excitation beam with controlled polarization pattern to determine three-dimensional molecular orientation,” *Jpn J Appl Phys* **44**(33-36), L1066–L1068 (2005).
- [109] S. Carrasco, B. E. A. Saleh, M. C. Teich, and J. T. Fourkas, “Second- and third-harmonic generation with vector Gaussian beams,” *J Opt Soc Am B* **23**(10), 2134–2141 (2006).
- [110] N. Olivier and E. Beaulieu, “Third-harmonic generation microscopy with focus-engineered beams: a numerical study,” *Opt Exp* **16**(19), 14,703–14,715 (2008).
- [111] D. P. Biss and T. G. Brown, “Polarization-vortex-driven second-harmonic generation,” *Opt Lett* **28**(11), 923–925 (2003).

- [112] K. Yoshiki, K. Ryosuke, M. Hashimoto, T. Araki, and N. Hashimoto, “Second-harmonic-generation microscope using eight-segment polarization-mode converter to observe three-dimensional molecular orientation,” *Opt Lett* **32**(12), 1680–1682 (2007).
- [113] V. V. Krishnamachari and E. O. Potma, “Detecting lateral interfaces with focus-engineered coherent anti-Stokes Raman scattering microscopy,” *J Ram Spectrosc* **39**(5), 593–598 (2008).
- [114] P. Schlup, J. Wilson, K. Hartinger, and R. A. Bartels, “Dispersion balancing of variable-delay monolithic pulse splitters,” *Appl Optics* **46**(23), 5967–5973 (2007).
- [115] M. Takeda, H. Ina, and S. Kobayashi, “Fourier-transform method of fringe-pattern analysis for computer-based topography and interferometry,” *J Opt Soc Am* **72**(1), 156–160 (1982).
- [116] O. Masihzadeh, P. Schlup, and R. A. Bartels, “Control and measurement of spatially inhomogeneous polarization distributions in third-harmonic generation microscopy,” *Opt Lett* **34**(7), 1090–1092 (2009).
- [117] B. Richards and E. Wolf, “Electromagnetic diffraction in optical systems. 2. Structure of the image field in an aplanatic system,” *Proc R Soc Lon Ser-A* **253**(1274), 358–379 (1959).
- [118] D. J. Moss, H. M. Vandriel, and J. E. Sipe, “Dispersion in the anisotropy of optical 3rd-harmonic generation in silicon,” *Opt Lett* **14**(1), 57–59 (1989).
- [119] C. L. Hsieh, R. Grange, Y. P, and D. Psaltis, “Three-dimensional harmonic holographic microscopy using nanoparticles as probes for cell imaging,” *Opt Exp* **17**(4), 2880–2891 (2009).
- [120] G. L. Rogers, “Gabor diffraction microscope: the hologram as a generalized zone plate,” *Nature* **166**, 237 (1950).
- [121] D. Wang, J. Zhao, F. Zhang, G. Pedrini, and W. Osten, “High-fidelity numerical realization of multiple-step Fresnel propagation for the reconstruction of digital holograms,” *Appl Opt* **47**(19), D12–D20 (2008).
- [122] T. M. Kreis, “Frequency analysis of digital holography with reconstruction by convolution,” *Opt Eng* **41**(8), 1829–1839 (2002).
- [123] C. K. Sun, “Higher harmonic generation microscopy,” *Adv Biochem Eng Biot* **95**, 17–56 (2005).
- [124] R. Hellwarth and P. Christen.P, “Nonlinear optical microscopic examination of structure in polycrystalline ZnSe,” *Optics Communications* **12**(3), 318–322 (1974).

- [125] P. J. Campagnola, A. C. Millard, M. Terasaki, P. E. Hoppe, C. J. Malone, and W. A. Mohler, “Three-dimensional high-resolution second-harmonic generation imaging of endogenous structural proteins in biological tissues,” *Biophysical Journal* **82**(1), 493–508 (2002).
- [126] Y. Guo, P. Ho, A. Tirkšliunas, F. Liu, and R. Alfano, “Optical harmonic generation from animal tissues by the use of picosecond and femtosecond laser pulses,” *Appl Opt* **35**(34), 6810–6813 (1996).
- [127] S. W. Chu, I. H. Chen, T. M. Liu, P. C. Chen, C. K. Sun, and B. L. Lin, “Multimodal nonlinear spectral microscopy based on a femtosecond Cr : forsterite laser,” *Opt Lett* **26**(23), 1909–1911 (2001).
- [128] G. Peleg, A. Lewis, M. Linial, and L. Loew, “Nonlinear optical measurement of membrane potential around single molecules at selected cellular sites,” *P Natl Acad Sci Usa* **96**(12), 6700–6704 (1999).
- [129] T. Colomb, J. K. Kuhn, F. Charriere, C. Depeursinge, P. Marquet, and N. Aspert, “Total aberrations compensation in digital holographic microscopy with a reference conjugated hologram,” *Opt Express* **14**(10), 4300–4306 (2006).
- [130] S. Nicola, P. Ferraro, A. Finizio, and G. Pierattini, “Wave front reconstruction of Fresnel off-axis holograms with compensation of aberrations by means of phase-shifting digital holography,” *Optics and Lasers in Engineering* **37**, 331–340 (2002).
- [131] T. Colomb, E. CuChe, F. Charriere, J. Kuhn, N. Aspert, F. Montfort, P. Marquet, and C. Depeursinge, “Automatic procedure for aberration compensation in digital holographic microscopy and applications to specimen shape compensation,” *Appl Optics* **45**(5), 851–863 (2006).
- [132] P. J. Campagnola, H. A. Clark, W. A. Mohler, A. Lewis, and L. M. Loew, “Second-harmonic imaging microscopy of living cells,” *J Biomed Opt* **6**(3), 277–286 (2001).